Numerical estimation of upward pressure differences over a placed block revetment under wave loading on a dike

M.F. van Heest

Delft University of Technology

TU Delft

Numerical estimation of upward pressure differences over a placed block revetment under wave loading on a dike

by

M.F. van Heest

Student number: 4357108
Project duration: May, 2022 – January, 2023
Thesis committee:

Prof. dr. ir. M.R.A. van Gent,	TU Delft (Chair of committee)
Dr. ir. R.J. Labeur,	TU Delft
Ir. M. Horstman,	Royal HaskoningDHV (Daily supervisor)

TU Delft

Royal HaskoningDHV
Enhancing Society Together

Preface

This thesis concludes my Master's degree in Hydraulic Engineering at the Delft University of Technology. During my studies, I specialized in coastal engineering because of my interest in this field. This research project was conducted in collaboration with the Coastal Engineering department of Royal HaskoningDHV. The project provided me with an opportunity to learn about research methodology and gain insights into the state of art of numerical modelling of wave-structure interaction of coastal structures.

I would like to express my gratitude to Mark Klein Breteler for providing me with the necessary data from the physical experiment and taking the time to explain the research and the results obtained. I also would like to extend my appreciation to my thesis committee members Marcel van Gent and Robert Jan Labeur for providing me with extensive feedback and guidance throughout the research process.

Special thanks to Marc Horstman, my daily supervisor at Royal HaskoningDHV, who guided me through the research process and helped me in setting up the CFD model. Marc Horstman was always available to contact and took a lot of time to assist me. I also would like to thank Cock van der Lem for his involvement in my research and for providing me with feedback.

Lastly, I would like to thank my family and friends for their personal support during these months. It would not have been a pleasant and educational experience without their encouragement.

M.F. van Heest
Delft, April 2023

Abstract

Placed block revetments on dikes are used for the protection of the structure against wave loading. The dimensions of the revetment are determined with empirical relations and design tools. The stability of the design solution needs to be checked by physical flume tests to ensure the safety of the structure. However, these tests can be costly and time-consuming. Research has to show whether computational fluid dynamics (CFD) can be used to improve the design process of the revetment and reduce the number of required physical flume tests. The most important load on a placed block revetment is an uplifting force that results from a (porous media) flow through the top and filter layer of the structure during wave-structure interaction. This study aimed to determine whether CFD modelling can accurately predict the uplift of the top layer of a placed block revetment and identify the optimal approach for modelling this type of revetment.

In order to reach this goal, an existing CFD model is used and validated with a physical test performed in the Delta Flume. First, the data from the physical test is extensively analysed to check how the results relate to the physical processes described in the literature. Next, a two-dimensional CFD model has been set up with the open-source software package OpenFOAM. To mimic the physical test, the model is created in 1:1 scale with all the structure dimensions similar to the Delta Flume set-up. The top layer in the physical test consisted of C-star blocks that have been schematized in order to model the structure as a two-dimensional model. Two different schematizations are proposed and tested on their performance. In the first schematization, the top layer is modelled as a continuum in which the resistance is determined by the Darcy-Forchheimer equations, just as in the filter layer. In the second schematization, the top layer is modelled by rectangular blocks alternated by small gaps. The CFD model results and the physical test are compared based on trends and statistics.

The model performance has been evaluated for three consecutive processes. First, the wave generation and propagation are analysed by comparing the wave spectra of the incoming waves and monitoring the wave conditions along the numerical flume. The model could reproduce a wave spectrum accurately, and the wave properties remained constant during propagation. The second process that has been evaluated is the wave-breaking that results in wave loads on the slope. It has been shown that the quasi-static wave loads are predicted with a reasonable accuracy (i.e. measured values deviate less than 10%) while the dynamic wave loads deviate up to 35% from the physical test results. It is concluded that there is room for improvement in modelling the wave-breaking. The last evaluated process is the porous media flow that leads to pressure differences over the top layer. The optimal schematization of the top layer was the rectangular blocks alternated with gaps. Just as in the physical test, only the dynamic wave loads lead to upward forces. These predicted forces deviate less than 20%.

To model the flow through the top layer, the local inertia, advective inertia and resistance terms are important in the conservation of momentum equation. For the top layer schematized with a continuum layer, the advective inertia term is underestimated by orders of magnitude leading to inaccurate results. The top layer schematized with rectangular blocks led to load predictions with reasonable accuracy. The resistance term was underestimated because no shear stress in the gaps between the blocks was included. However, the resistance term is small compared to the local inertia and advective inertia.

In future research, additional attention should be given to determining the optimal grid resolution. Results have shown that decreasing the grid sizes leads to increased predicted pressures. It could also be beneficial to further investigate the modelling strategy of the top layer. Schematization 2 has led to the most accurate model results. However, this model requires a fine grid resolution to resolve the flow through the gaps, leading to high computational times. A CFD model in which the top layer is schematized as a continuum would be beneficial in terms of computational times. Increasing the fictional porosity and grain size increase the contribution of the inertia term in the momentum balance, leading to better results. Investigating a method for obtaining these values may be of added value.

Contents

List of Figures

List of Tables

Nomenclature

Abbreviations

Abbreviation	Definition
CFD	Computational Fluid Dynamics
CFL	Courant Friedrichs Lewy number
DBM	Dynamic Boundary Method
ISM	Impulse Source Method
KC	Keulengan-Carpenter number
MSM	Mass Source Method
NB	Numerical Beach
NSE	Navier Stokes equations
NLSWE	Nonlinear Shallow Water equations
OpenFOAM	Open Field Operation And Manipulation
RANS	Reynolds Averaged Navier Stokes equations
RZM	Relaxation Zone Method
SBM	Static Boundary Method
SPH	Smoothed Particle Hydrodynamics
VARANS	Volume Averaged Reynolds Averaged Navier Stokes equations
VOF	Volume of fluid method

List of symbols

Symbol	Definition	Unit
α	Empirical coefficient Darcy-Forchheimer equation	[-]
β	Empirical coefficient Darcy-Forchheimer equation	[-]
γ	Indicator function	[-]
γ_t	Surface tension coefficient	[-]
γ_p	Empirical coefficient	[-]
ε_p	Loss coefficient	[-]
κ	Hydraulic conductivity	[m/s]
κ_y	Surface curvature	[m^{-1}]
Λ	Leakage length	[m]
μ	Dynamic viscosity	[Pa*s]
ξ	Iribarren number	[-]
$\xi_{m-1,0}$	Iribarren number based on the spectral wave period	[-]
ρ	Density	[kg/m^3]

υ	Kinematic viscosity	[m^2/s]
Φ	Hydraulic head	[m]
Φ_t	Hydraulic head on top layer	[m]
Φ_f	Hydraulic head in filter layer	[m]
∇	Stress tensor	[-]
a	Resistance coefficient	[m^2/s]
A	Surface	[m^2]
b	Resistance coefficient	[m^2]
b	Thickness of the filter layer	[m]
C	Courant number	[-]
c	Empirical coefficient	[-]
C_m	Added mass coefficient	[-]
d_{n50}	Grain diameter	[m]
D	Thickness of the top layer	[m]
e_p	Degree of openness	[-]
f	Frequency	[Hz]
F_p	Resistance force from permeable structure	[kN]
g	Gravitational acceleration	[m/s^2]
h	Still water level	[m]
H	Wave height	[m]
H_s	Significant wave height	[m]
$H_{1/3}$	Wave height exceeded by 1/3 of the waves	[m]
$H_{1/10}$	Wave height exceeded by 1/10 of the waves	[m]
$H_{2\%}$	Wave height exceeded by 2% of the waves	[m]
H_{m0}	Significant wave height based on spectrum	[m]
i	Gradient	[-]
i_t	Gradient over top layer	[-]
i_f	Gradient in filter	[-]
k	Linearized permeability of the filter layer	[m^3/s]
k'	Linearized permeability of the top layer	[m^3/s]
KC	Keulegan - Carpenter number	[-]
L_0	Deep water wavelength	[m]
L_R	Length of relaxation zone	[m]
m_0	Variance	[m^2]
N_p	Porosity of permeable structure	[-]
N	Number of waves	[-]
p^*	Excess pressure	[Pa]
p_{max}	Maximum pressure	[Pa]
p	Pressure	[Pa]
p_b^*	Pressure at the boundary	[Pa]
p_{ref}^*	Pressure in imaginary reservoir on backside structural element	[Pa]
Q_t	Inflow through top layer	[m^3/s]
Q_{f1}	Inflow through filter layer	[m^3/s]
Q_{f2}	Outflow through filter layer	[m^3/s]

q	Flow velocity through filter layer	[m/s]
q_t	Flow velocity through top layer	[m/s]
$R_{2\%}$	Run-up exceeded by 2% of the waves	[m]
T	Wave period	[s]
T_m	Mean wave period	[s]
T_p	Peak period	[s]
T_{m01}	Spectral period	[s]
T_{m02}	Spectral period	[s]
$T_{m-1,0}$	Spectral period	[s]
u_f	Velocity in filter	[m/s]
u_r	Relative velocity	[m/s]
u_l	Liquid velocity	[m/s]
u_g	Liquid velocity	[m/s]
$u_p^{\perp}$	Pore velocity	[m/s]
$u^{\perp}$	Filter velocity normal to structure element	[m/s]
z	Elevation	[m]

.

1

Introduction

1.1. Background

A flood defence is a hydraulic structure with as main function the protection of areas of interest against flooding. The threat of flooding could originate from seas, rivers, lakes, or other waterways. An example of a flood defence is a dike. A dike is a water-retaining structure consisting of soil with sufficient elevation and strength to be able to retain the water under extreme circumstances (Jonkman et al., 2021). If a dike fails, the hinterland may be flooded. This could lead to loss of life and economic damage, especially in low-lying countries such as the Netherlands. To prevent flooding, the Dutch government has prescribed a maximum failure probability for each dike within the country by law. Dikes may fail in several ways, each with its own associated probability of failure. To ensure their safety, the total probability of failure across all failure mechanisms cannot exceed the prescribed failure probability for the dike. This safety criterion applies to the annual probability of failure and is the only requirement that dike curators, typically waterboards, must meet. The hydraulic boundary conditions mainly determine the design of the dike. Sea dikes, for example, are subjected to wave loading. Without the protection of the soil mass, the dike will eventually fail by erosion of the outer slope. An effective way to deal with this phenomenon is the placement of hard revetments to protect the subsoil. Hard revetments can consist of natural rock, concrete elements, or asphalt (Schiereck et al., 2019). Figures 1.1 and 1.2 show examples of hard revetments. This thesis will mainly focus on the hydraulic loads on placed block revetments.

Figure 1.1: Pattern placed revetment with shaped natural rock, from (Dorst et al., 2012).

Figure 1.2: Placing of Hydroblocks, from (Dorst et al., 2012).

The design process of a revetment is iterative. In the Netherlands, it is common to use the tool Steentoets (Klein Breteler et al., 2014). In this tool, empirically derived relations describe the wave loading on dikes, which makes it possible to perform safety assessments. Steentoets is created by Deltares and approved by the Dutch government and therefore commonly used. The design process consists of several steps. First, the client composes a program of requirements. Utilizing these boundary conditions, engineers can start to design the dike. To this end, they need to collect all the relevant data consisting

of e.g. hydraulic boundary conditions, location, orientation, geometry and soil properties. The dike has to be divided into subsections such that each cross-section within a subsection has approximately the same orientation, geometry, and soil properties. Then, a selection of possible revetments for each subsection has to be made. After that, for single elements of the revetment (under layer, filter layer, filling layer, and top layer) the required dimensions are determined using empirical relations. Also, the toe construction and transitions must be designed at this point. A first dike design is obtained and can be verified with Steentoets (Klein Breteler et al., 2015). Figure 1.3 gives a schematization of the described design process.

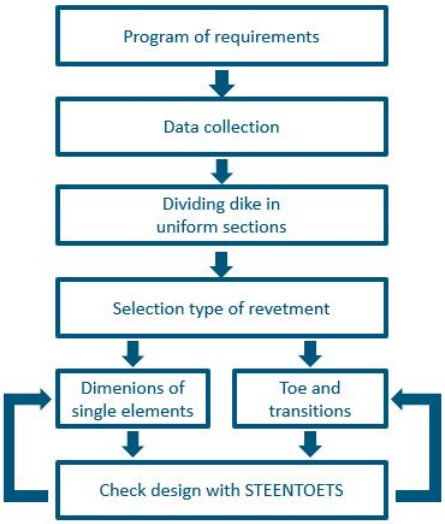

Figure 1.3: Design process of a dike. (Klein Breteler et al., 2015)

Empirical relations can be used to relate the hydraulic loads on a dike to the dimensions of the different elements of the revetment. The tool Steentoets can then test whether the loads on a proposed revetment design are smaller than its strength for those dimensions. If a design solution is approved by Steentoets, in may cases the conceptual design is considered complete. However, the reliability of the design is often questioned, leading to physical flume tests to observe the wave-structure interaction in greater detail and ensure the structural integrity of the final design solution.

1.2. Problem definition

Wave loading on revetments is a very complex process. Empirical relations have been derived to relate wave conditions to the stability of a revetment (e.g. *The Rock Manual* (2007)). These empirical relations are implemented in design tools, that are used as described in Section 1.1. Nevertheless, the use of empirical tools (such as Steentoets) is not sufficient for evaluating the safety of a revetment (Blacka et al., 2011). Empirical relations are only valid when they are applied in situations with the same, or a very similar, configuration as the tests they are derived from. As a consequence, some structure designs rely on the use of empirical relations outside of their range of validity for safety assessment purposes. Therefore design solutions have to be tested in small or large-scale physical models before they can be built. Physical flume tests increase both the duration and the costs of the design phase of a project. Especially large-scale tests of complex configurations can entail significant costs (Neves et al., 2021). Flume tests can also be performed with small-scale models in order to reduce costs. However, this could lead to inaccurate results, because of scaling effects that might occur (Howarth et al., 1996). To reduce the number of required tests in physical models, numerical modelling may be suitable. Numerical computer simulations that describe physical (hydraulic) processes are known as Computational Fluid Dynamics (CFD) models. Various CFD models based on different equations are derived in the past and used to simulate wave-structure interactions (Higuera et al., 2014b). Navier Stokes (NS) models are an example of CFD models. NS models are valided for a wide range of wave-structure interactions (Higuera et al., 2014a). Examples of NS models that are developed are OpenFOAM, COBRAS, IH3VOF, ComFlow and FLOW-3D (Jacobsen et al., 2018). A challenging as-

pect of CFD modelling is the wave-structure interaction for porous structures. In Van Gent (1995) an NS model was developed and successfully used in which the effects of the porous media were included via resistance source terms and a number of other parameters. In this method the porous media is treated as one continuum, so the model does not resolve the flow in the actual pores. The porous media flow in this model was described by the extended Darcy-Forchheimer equation. This approach is successfully applied to several case studies. This research will further explore the possibility of applying a porous media flow through a continuum for the top and filter layer, to simulate wave loading on a dike.

1.3. Objective and research questions

The objective of this thesis is formulated as:

To determine whether CFD modelling can accurately predict hydraulic loads on placed block revetments as a result of wave impacts.

This research objective can be translated into a research question. The research question is stated below, followed by 5 sub-questions that will support this main question:

What is the most effective way to model a placed block revetment using CFD to simulate the hydraulic head over a revetment, which consequently can cause uplift of units in the top layer? Which physical processes should be incorporated into this model?

1. What are the physical mechanisms that lead to different pressure signals on the top layer and in the filter layer of a placed block revetment?
2. How does the pressure distribution on the top layer of a dike predicted by CFD modelling relates to the pressure distribution from a similar setup in a physical test?
3. How do the filter pressures in a dike determined by CFD modelling relate to the filter pressures determined in physical tests?
4. To what extent is it feasible to model a placed block revetment of a dike as a continuum, and what are the required α and β values for producing accurate estimates of hydraulic loads?
5. What would be the added value of CFD modelling in the design process of placed block revetments?

To address these inquiries, it is essential to identify the specific physical processes responsible for generating wave loads on a placed block revetment on a dike. Furthermore, it is crucial to determine how to integrate these processes into a CFD model and identify which discretizations are suitable in order to obtain a computationally efficient model that produces accurate predictions.

1.4. Approach and methods

This thesis aims to validate the hydraulic loads on a placed block revetment obtained from CFD modelling. In order to answer the research questions, a methodology is proposed consisting of a couple of steps. These steps are illustrated in Figure 1.4 and described in this section. First, a literature study is performed to gain insight into wave loading on dikes and the state of art in CFD modelling of wave interaction with hydraulic structures. Also, the most recent developments and knowledge about CFD modelling of hydraulic structures will be addressed. Next, data of a physical experiment in which a placed block revetment is subjected to waves will be investigated. This part should provide inside whether physical processes and principles as explained in the literature are observable in practical applications. This included the mapping of the hydraulic conditions and the measured pressures. Thereafter, a CFD model will be set up. Combining the state of art known from the literature, and the analysis of the physical experiment should lead to a model that mimics the physical tests. This includes the determination of empirical coefficients. In the last stage of the research, numerical simulations with all the final settings will be executed. Based on the results, conclusions and recommendations will be made.

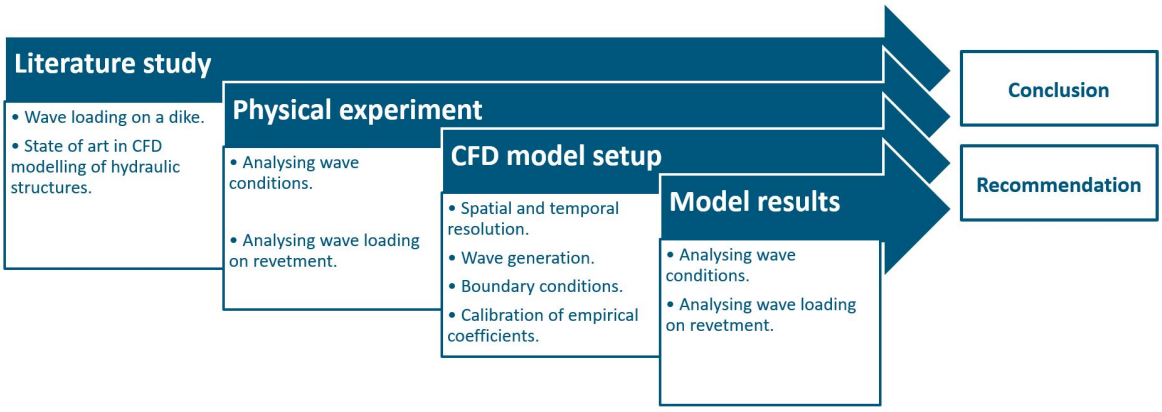

Figure 1.4: Research Methodology.

1.5. Thesis outline

The structure of the remainder of this report is as follows:

- Chapter 2 gives an overview of the relevant literature for this research. First, the physical processes that are relevant for wave loading on dikes are described. This includes the subsections: 'Failure mechanisms of block revetments', 'Wave loading on a dike' and 'Leakage length'. Chapter 2 ends with the state of art of CFD modelling of wave interaction with hydraulic structures.
- Chapter 3 presents an overview of a previously conducted physical model test where a dike was subjected to wave loading. The chapter begins with a description of the research that was employed in the study. Subsequently, the experimental setup for the model is outlined. Finally, the chapter concludes by presenting the results obtained from the physical model test.
- Chapter 4 briefly describes which settings are used in the numerical model. The chapter starts with an approach to explain which simulations are used for the calibration of the empirical coefficients in the model. Next, the flume layout, spatial and temporal resolution, wave generation and boundary conditions are discussed. Thereafter, the design of the top layer and filter layer are described. The chapter concludes with an overview of the final settings.
- Chapter 5 describes multiple numerical simulations in order to reflect on the model performance, for wave loading on dikes. This process is divided into three different steps that are separately considered. First, the wave generation and propagation towards the dike are analysed. Next, the pressures on the slope of the dike have been analysed. The last step in the wave-loading process is the appearance of pressure differences over the top layer. After reflecting on these three steps, also the importance of the leakage length of the structure has been assessed and a scaling analysis of the momentum balance is performed.
- Chapter 6 gives a discussion of the performed research. This chapter is divided into three sections. The first section elaborates on the validity of the results. Next, the interpretation of the results is discussed. Justifications for the model outcomes are provided alongside the connection of the results with the underlying theory. The last section describes the limitations of the performed research.
- Chapter 7 provides the overall conclusion and answer to the main question and the sub-questions. This chapter ends with recommendations for future research.

2

Literature review

In this chapter, an overview of the relevant literature is given. This overview concerns physical processes, dike properties and information about numerical modelling. In Section 2.1 a summary of the different failure mechanisms of block revetments is given. The next subsection describes the different stages of the process of wave loading. In Section 2.3 the most important revetment property (in terms of stability) is discussed. The last subsection gives information about numerical modelling.

2.1. Failure mechanisms of placed block revetments

Nowadays, a lot of different block revetments are used for the protection of dikes. These revetments can be categorized in several ways. It is for example possible to categorize the block revetments by permeability, type of material or the shape of the elements. The most common way is to categorize the placed block revetments by their form, which results in three main types: loose blocks, interlocking blocks and block mattresses (Wolsink, 1984). Loose blocks are placed adjacent to each other which results in surface friction. Interlocking blocks are physically interconnected by their shape. Therefore a single block can't be pushed out of the layer without breaking. Block mattresses are blocks connected through a cable. This thesis will only focus on loose block revetments.

Loose (placed) block revetments can be built of natural stones such as basalt, or concrete. The block revetment is normally placed in a regular pattern on a filter layer consisting of granular material. This layer protects the subsoil against erosion. The smooth surface has as advantage that water flow over the top layer generates barely shear forces. The loads generated by flows are negligible compared to wave loading. There are three different failure mechanisms as a result of wave loading (Klein Breteler et al., 2014):

- Uplifting of the top layer
- Sliding top layer (failing of underlayer)
- Granular transport through top and filter layer

These failure mechanisms will be discussed next.

2.1.1. Uplifting of the top layer

Top layer instability can occur when (single) blocks are exposed to uplifting forces. The resistance against the instability of a block is determined by its own weight and the friction force caused by the surface interaction with the adjacent blocks. The load on the blocks that can cause damage is an upward force resulting from a pressure difference over the top layer. This pressure difference is normally expressed in terms of a hydraulic head difference as this quantity is easier to relate to water flow (Klein Breteler et al., 2014). There are two critical moments during a wave cycle. These moments are the moment of maximum run-down and the moment of wave impact. During these stages of the wave cycle, the largest head differences over the top layer are generated. The uplift force is generated when

the pressure in the filter layer is larger than the pressure on the top layer, for two points located on the same line perpendicular to the slope of the revetment. Figure 2.1 and 2.2 show the hydraulic head at the two critical moments, in both the filter and top layer. The larger the difference in hydraulic head, the larger the uplift force. Besides the wave loading, the difference in the hydraulic head is dependent on the permeability and thickness of both the filter layer and the top layer. This principle will be further evaluated in Section 2.3.

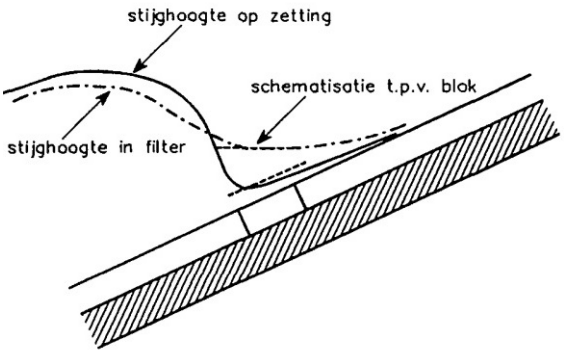

Figure 2.1: Hydraulic head toplayer and filter layer wave front (de Waal et al., 1995).

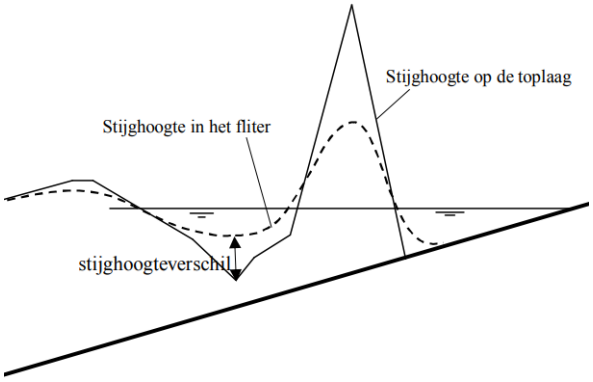

Figure 2.2: Hydraulic head toplayer and filter layer wave impact (Klein Breteler et al., 2012).

2.1.2. Sliding of top layer

Significant groundwater pressure and liquefaction lead to sliding of the top layer. Especially with very open, but interlocking structures one may fear this mechanism (Dorst et al., 2012). In the case of a filter or top layer on clay, this might happen when a high phreatic level is present. If the filter layer and top layer are directly placed on a sand core, the wave run-up and run-down can also cause this mechanism (Klein Breteler et al., 2014).

2.1.3. Granular transport through top and filter layer

If a top layer has a very low permeability, pressure build-up under the layer could be significant. When the layer is very open, water can easily flow out and the difference in the hydraulic head would be a lot less than in case of the low permeability. From that perspective, it is favourable for a dike to have a top layer with high permeability. However, if the permeability is too large, granular material from the filter layer could migrate through the exits of the revetment. Then, erosion of the filter layer will occur and the slope will deform. The same principle could happen between the core material and the filter layer if the filter is not designed correctly (Dorst et al., 2012).

Two of the three failure mechanisms explained above do not originate from wave-structure interaction. Sliding of the top layer occurs only in the presence of significant groundwater pressure of liquefaction. Granular transport between two consecutive layers can only happen if the difference in grain size is too large. To prevent these two failure mechanisms, wave conditions are not the decisive factor in the design. In contrast, uplifting of the top layer depends entirely on the wave-structure interaction. Therefore, this report will focus only on the failure of a placed block revetment caused by uplift since this failure mechanism fully depends on the wave-structure interaction. The design determines the strength of the structure, and the minimum strength required is dependent on the wave loading. The next subsection will focus on the wave loading on dikes and provide more details about the different stages of wave loading.

2.2. Wave loading on a dike

In general, sea dikes are exposed to wind waves and swell. Wind waves are typically short-crested and irregular, while swell waves typically are more regular with long periods and wide crests (Schiereck et al., 2019). When waves reach a dike, they can reflect and/ or break. Whether a wave will break or

not, depends on the wave steepness compared to the slope of the dike. This ratio between the slope of the dike and the steepness is called the dimensionless Iribarren number (ξ):

$$\xi = \frac{\tan \alpha}{\sqrt{\frac{H}{L_0}}} \tag{2.1}$$

With:

$$L_0 = \frac{gT^2}{2\pi} \tag{2.2}$$

In these equations, L_0 is the deep water wavelength, α is the slope of the revetment, H is the wave height, g is the gravitational acceleration and T is the wave period. Laboratory tests have shown that when the Iribarren, number is smaller than $\xi = 2.3$ waves will break while for Iribarren number larger than $\xi = 2.3$ waves will reflect (Battjes, 1974). The breaker types of waves on dike slopes can be further divided based on the way they break. The different breaker types are shown in Figure 2.3. Surging breakers can be found on relatively steep slopes and could be related to standing waves. Collapsing breakers are between breaking and non-breaking. Plunging breakers cause the highest impact. The crest of the wave curls over and locks in the air content under the breaking wave and the water will crash on the slope like a water jet. The last breaker type is the spilling wave. In the situation of a spilling wave, the slope of the dike is relatively mild. The waves break (without generating a water jet) because of the decreasing water depth in a similar way as it does in shallow water in front of flat beaches.

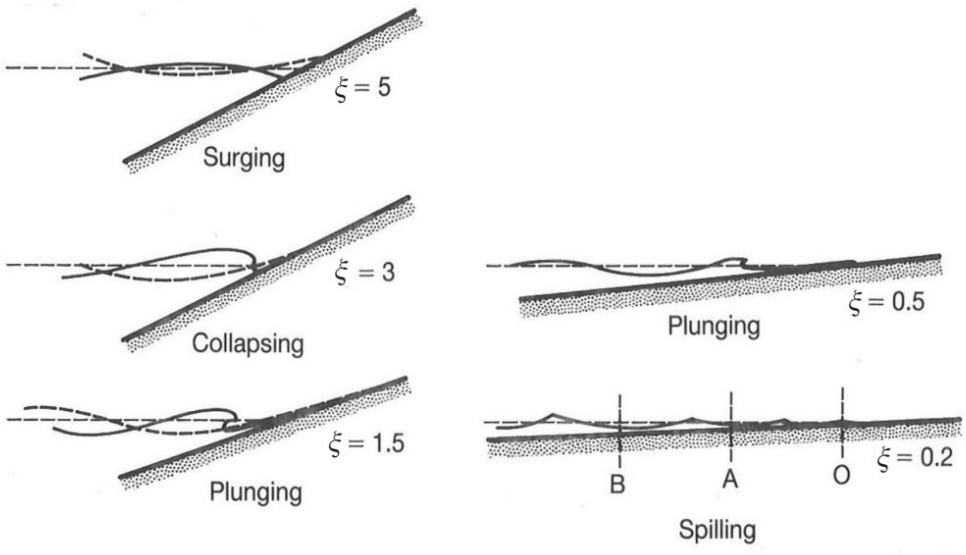

Figure 2.3: Breaker types (*The Rock Manual*, 2007).

Wave attack will result in wave impact, run-up and run-down. Especially plunging breakers can produce high peak pressures on the slope of the dike because a big amount of the wave energy is dissipated over a short distance and within a short time (Yang, 2017). During wave run-up, the resulting forces by the waves will be directed opposite to the gravity forces. Therefore, for smooth slopes, the run-up is less hazardous than the wave run-down (Pilarczyk & Klein Breteler, 1998). As the negative impact of run-up is negligible for the stability of smooth block revetments, only wave run-down and wave impact will be discussed in the next subsections.

2.2.1. Wave run-down

Before wave impact, water flows along the slope in a downward direction. This flow is induced by gravity and is called wave run-down. Wave run-down leads to two load mechanisms on the revetment

of the dike. The first mechanism concerns a drag force on the revetment while at the same time, the phreatic level in the filter will decrease and therefore create a flow gradient in the filter layer. This mechanism may result in geotechnical instabilities such as subsoil erosion and sliding of the revetment. Especially in the case of steep slopes, this phenomenon can be decisive in the design. The second load mechanism caused by wave run-down is reached at maximum wave run-down. During maximum wave run-down there will be an incoming wave that subsequently causes a wave impact. Just before impact, there is a wavefront that creates high pressure on the top layer beneath the point of maximum run down. This pressure leads to a water flow through the filter layer in an upward direction. At this point in time, the pressure in the filter layer around the run-down point is increased, while at the same time, the surface of the revetment above the run-down point is almost dry. Locally, the hydraulic head will decrease so there will be a low pressure on the structure. The interaction of high pressure beneath the revetment and low pressure above the revetment may cause uplift (Pilarczyk & Klein Breteler, 1998). This principle is depicted in Figure (2.4).

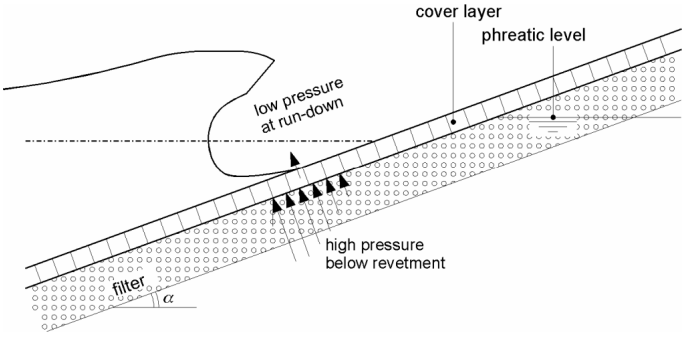

Figure 2.4: Pressure difference over top layer (Pilarczyk & Klein Breteler, 1998).

The placed block revetments will experience the biggest uplifting forces around the run-down point during wave run-down. Determining the location of this critical point in advance is essential as it can help optimize the design of the revetment. However, there are several empirical relations proposed to predict the location of maximum wave run-down that not always leads to the same result. Wave run-down measurements show large scatters and it seems difficult to accurately predict the location of maximum run-down. In fact, the different known formulas to predict the run-down even vary in their dependencies. Run-down relations (2.3) and (2.4) are included in the *The Rock Manual* (2007). These relations are valid for irregular waves on straight smooth slopes. The run-down is only related to the significant wave height (H_s) and the Iribarren number (ξ). No run-down reduction due to roughness is included in this relation. Also, the structure is assumed to be impermeable. $R_{2\%}$ is the run-down distance from still water level that will be exceeded by 2% of the waves.

$$R_{2\%}/H_s = 0.33\xi \quad for \quad 0 < \xi < 4 \tag{2.3}$$

$$R_{2\%}/H_s = 1.5 \quad for \quad \xi \geq 4 \tag{2.4}$$

Equations (2.3) and (2.4) will only give accurate results when applied to situations with similar structures (i.e. impermeable structures with the same surface roughness as the structures used to derive the formulas.) Most of the hydraulic structures will not be in the range of validity of these formulas in practice. A calculation with these equations will only give a rough estimation of the wave run-down. When higher accuracies are desirable, physical tests are still needed.

2.2.2. Wave impact

Sections of the dike slope which are located below the water surface are subjected to quasi-static wave loads. For slopes that are subjected to breaking waves, there is a point of impact. At this impact location the slope experience dynamic wave loads. The dynamic wave load on a slope is relevant for the determination of the stability of the revetment. The impact location is normally distributed and in close relation to the run-down point (Peters, 2017). As mentioned in the previous subsection, plunging breakers generate the highest peak pressures. Using an extreme value analysis, the results may

be described statistically, most sufficiently with a log-normal distribution (Grüne, 1989). In literature, several empirical relations are derived to calculate the peak pressure, based on performed wave tests. These empirical relations have the following form:

$$p_{\max} = c\rho_w g H_s \tag{2.5}$$

In this equation, p_{max} is the maximum pressure that could occur for the given wave conditions, c is an empirical coefficient, ρ_w is the density of water, g is the gravitational acceleration and H_s is the significant wave height. In the research of Peters (2017), results from different wave tests, which contain measurements of peak pressures, are compared. Both regular waves and irregular waves on different slopes and different wave conditions are included. For irregular waves this has led to an extended relation for determining the peak pressure:

$$\frac{p_{\max 2\%}}{\rho_w g H_s} = 8 - 1.6\xi_{m-10} - \frac{2}{\left(\xi_{m-1,0} - 0.2\right)^2} \tag{2.6}$$

In this equation, $p_{max2\%}$ the pressure that will be exceeded by 2% of the waves and $\xi_{m-1,0}$ the Iribarren number based on the spectral wave period. Figure (2.5) shows the normalized peak pressure versus the Iribarren number. The empirical formula is plotted in the same coordinate system as used for field tests of natural storms by Grüne (1989), Delta Flume tests by Klein Breteler and Van der Werf (2016) and experiments by Fuhrboter and Sparboom (1988).

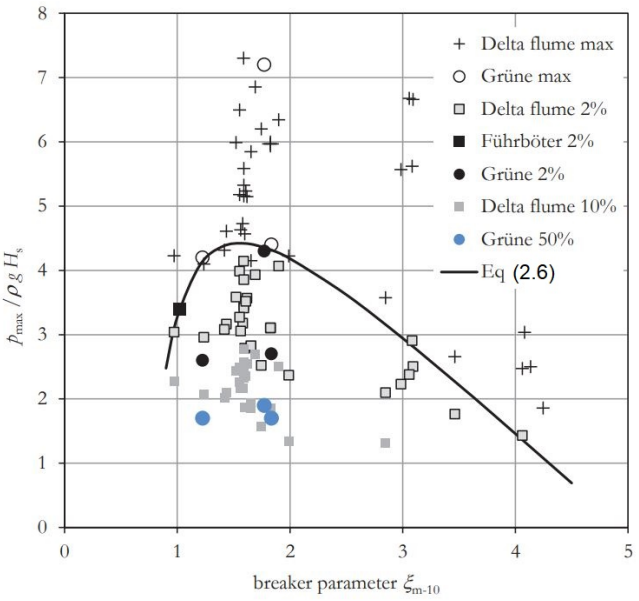

Figure 2.5: Pressure vs. Iribarren number (Peters, 2017).

In Figure 2.5 a lot of scatter from the physical tests can be found. From this figure, it is difficult to conclude that equation (2.6) is the best fit for the performed flume tests. The empirical relation is not sufficient to determine accurate peak pressures that can be used for a design of a structure, without further physical investigation of the real pressures occurring for given wave conditions.

2.3. Leakage length

The uplifting forces that can occur on a placed block revetment are caused by the difference in hydraulic head on the top layer and in the filter layer. The highest uplifting forces are reached at maximum wave run-down and during the wave impact. The hydraulic head in the filter layer in these critical situations is, respectively, determined by the quasi-static wave load and the total force on the revetment caused by the wave impact, in combination with the permeability of the top and filter layer. A large permeability of the filter layer leads to higher flow velocities through the layer and higher forces on the top layer compared to a situation with a small permeability. The water flow through the filter will leave the structure

via the open spaces between the block revetment to the surface and relieve the filter pressure. When the flow experiences no resistance from the top layer e.g. the top layer has a high permeability, the increase in filter pressure will be small because the excess water will unhindered leave the filter and relieve the pressure. If the water flow experiences a high resistance from the top layer e.g. the top layer has a high permeability, it takes more time to drain water from the filter and relieve the pressure. This results in an increase in filter pressure. The ratio in permeability between the top layer and filter layer will determine the difference in hydraulic head over the top layer, given the wave conditions. This ratio in permeability is known as the leakage length (Λ) (Klein Breteler et al., 2014). Formula (2.7) describes this leakage length. The permeability of the top layer increases for both a decrease in thickness (D) and an increase in the linearized permeability (k') of the top layer, while the permeability of the filter layer increases if the thickness of the filter layer (b) increases as well as if the linearized permeability (k) increases. Therefore the product of b, D and k divided by k' gives a ratio of the permeability of the top and filter layer. This ratio is squared in other to obtain the right unit. In a system with a large leakage length, big differences in hydraulic head can occur while for a small leakage length the pressure difference will be smaller for the same wave forcing.

$$\Lambda = \sqrt{\frac{bDk}{k'}} \tag{2.7}$$

In the section below an analytical derivation of a differential equation is given that relates the difference in hydraulic head to the leakage length, as described in (Klein Breteler et al., 2014). A situation in which a revetment is exposed to a wavefront is considered (Figure 2.4). The hydraulic head is defined as:

$$\phi = \frac{p - p_{atm}}{\rho g} + z \tag{2.8}$$

Unlike the quantity pressure, the hydraulic head is not dependent on the water depth. To derive the differential equation that describes wave loading on a dike, a small section of the top layer with a filter layer is considered as shown in Figure 2.6. A flow in the filter layer parallel to the layer itself is considered. The flow in the top layer is perpendicular to the layer. The layer below the filter is considered to be impermeable so no interaction will take place.

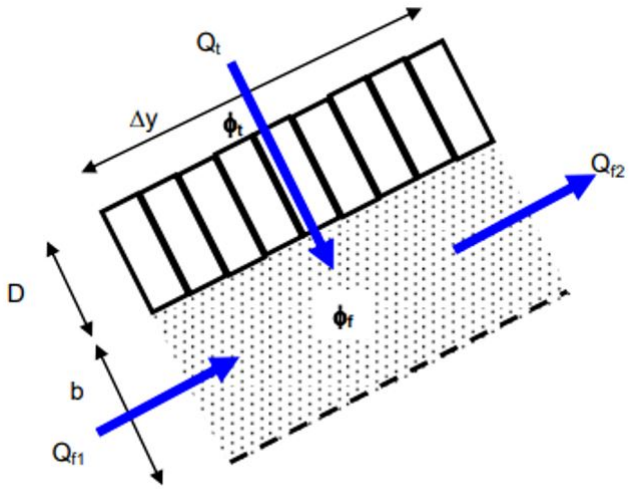

Figure 2.6: Mass balance top and filter layer (Klein Breteler et al., 2014).

For the given situation a mass balance can be considered. The inflow is equal to the outflow. That means that the flow through the top layer equals the difference in flow through the filter:

$$Q_t = Q_{f2} - Q_{f1} \tag{2.9}$$

In this formula, Q_t is the flow through the top layer, Q_{f1} the inflow through the filter and Q_{f2} the outflow through the filter. The top layer can be schematized to be homogeneous with a certain permeability in order to substitute the discharge with the product of the flow velocities (q) and surfaces (A):

$$q_t A_t = q_2 A_f - q_1 A_f \tag{2.10}$$

A_t is the surface of the revetment that is considered, A_f is the surface of inflow and outflow in the filter, q_t is the mean flow velocity through the top layer and q_1 and q_2 are respectively the mean outflow and the mean inflow through surface A_f. If only one meter of the dike is considered, this leads to:

$$\Delta y q_t = b\,(q_2 - q_1) \tag{2.11}$$

$$q_t = b\frac{\Delta q_f}{\Delta y} \tag{2.12}$$

Next, Darcy's law ($q = k * i$) will be used to rewrite the equation. At the same time Δy is made infinitely small and therefore replaced with ∂y:

$$k' i_t = b\frac{\partial\left(k i_f\right)}{\partial y} \tag{2.13}$$

The gradient over the top layer is equal to the difference in hydraulic head over the top layer divided by the thickness of the layer: $i_t = (\phi_t - \phi_f)/D$. For the gradient in the filter applies $i_f = -\partial\phi_f/\partial y$. The new equation equals:

$$k'\left(\phi_t - \phi_f\right)/D = -bk\frac{\partial^2\left(\phi_f\right)}{\partial y^2} \tag{2.14}$$

$$\phi_t = \phi_f - \frac{Dbk}{k'}\frac{\partial^2\left(\phi_f\right)}{\partial y^2} \tag{2.15}$$

And after substituting the leakage length:

$$\phi_t = \phi_f - \Lambda^2\frac{\partial^2\left(\phi_f\right)}{\partial y^2} \tag{2.16}$$

Differential equation (2.16) shows that for a given hydraulic head on the top layer, both the hydraulic head in the filter layer and the difference in hydraulic head over the top layer are only dependent on the leakage length λ. The leakage length is therefore an important characteristic value for a dike, which should be considered when a structure is modelled. Equation (2.16) can only be solved analytically if boundary conditions are highly schematized and if flow in the filter layer is assumed to be laminar (Schiereck et al., 2019). In practice, the loads on a placed block revetment are typically not determined analytically. Instead, empirical relations are derived to determine the dimensions of a placed block revetment for a given wave load, in order to remain stable. However, numerical modelling can be used to predict the acting forces on a structure during wave loading.

2.4. Numerical modelling

To reduce the number of required tests in physical models, numerical modelling may be suitable. Numerical computer simulations that describe physical (hydraulic) processes are referred to as computational fluid dynamics (CFD) models. There are different CFD models that can simulate wave-structure interaction, categorized on the equations that are used. These alternatives are the Nonlinear Shallow water (NLSW) models, Boussinesq-type models and the incompressible flow models, based on the Navier Stokes (NS) equations. The (NLSW) can only be applied if no important accelerations exist in the vertical direction i.e. hydrostatic situations. The Boussinesq-type model has the limitation that wave breaking cannot be modelled in detail. The (NS) equations can be solved either using Smoothed Particle Hydrodynamics (SPH) or a Volume-Of-Fluid (VOF) method. (SPH) models solve from a Lagrangian point of view while the VOF is an Eulerian-type model. Lagrangian models are computationally too expensive to apply on large domains that are normally needed for wave-structure interactions. The

VOF models are not limited by the limitations mentioned above and therefore suitable for a wide range of wave-structure interactions. (VOF) models have already been applied to coastal engineering for a long time and various cases with wave-structure interaction are validated (Van Gent, 1995). The CFD model that is used in this thesis is the Navier Stokes model named OpenFOAM (Weller et al., 1998). OpenFOAM is an open-source software, which means that it is free to use, modify, and distribute. It is accessible to a wide range of users and allows for greater customization of the code. This makes OpenFOAM a suitable model for this thesis. The next subsections will elaborate more on both the mathematical and numerical framework that is used.

2.4.1. Mathematical framework

Volume Averaged Reynolds Averaged Navier-Stokes Equations
The CFD model has to solve the two-phase Navier-Stokes equations. This thesis makes use of the flow model OpenFOAM that solves for the fluids water and air. The Navier-Stokes equations are given in (2.17) and (2.18), and describe the conservation of mass and conservation of momentum respectively. In order to numerically solve the Navier-Stokes equations, a modification is made regarding the governing velocities. An averaging operation is performed by applying Reynolds decomposition. The velocity is decomposed into a time-averaged and fluctuation part: $u = \bar{u} + u'$. Substitution of this expression in the momentum equation leads to the Reynolds Averaged Navier-Stokes equations.

$$\frac{\partial \rho}{\partial t} + \nabla \cdot (\rho \bar{u}) = 0 \tag{2.17}$$

$$\frac{\partial \rho \bar{u}}{\partial t} + \nabla \left[\rho \bar{u} \bar{u}^T\right] = -\nabla p^* + g\chi\nabla\rho + \nabla[\mu\nabla\bar{u} + \rho\overline{u'u'}] + \sigma_T \kappa_\gamma \nabla\gamma \tag{2.18}$$

In the conservation of momentum equation, ($\nabla = \frac{\partial}{\partial x} + \frac{\partial}{\partial y} + \frac{\partial}{\partial z}$), $\bar{u} = (u, v, w)$ is the mean velocity in Cartesian coordinates, ρ is the flood density, $p*$ is the excess pressure, defined as: $p* = p - \rho g \cdot x$, g is the gravitational acceleration, $\chi = [x, y, z]$ is the Cartesian coordinate vector and μ is the dynamic molecular viscosity. The last term in the momentum equation is the effect of the surface tension. γ_T is the surface tension coefficient, κ_γ is the surface curvature and γ is the indicator function of the Volume of Fluid (VOF) field. A more extensive description of γ is given later in this section. In this thesis it is assumed that both water and air are incompressible, which led to the simplification of the conservation of mass equation (2.17) to (2.20).

$$\nabla \cdot \bar{u} = 0 \tag{2.19}$$

Besides the interaction of the waves with the top layer of the dike, also filter pressure has to be simulated in order to define the load on the revetment. The hydrodynamic model has to account for the porosity of the filter layer. Similar to the VOF-model by Van Gent (1995), in Jensen et al. (2014) a hydrodynamic model is used that accounts for permeable coastal structures. Thereafter, this model is used in multiple studies to describe the interaction between waves and permeable coastal structures and flow and morphological changes within an open filter (Jacobsen et al., 2018). In this hydrodynamic model, a volume averaging procedure on the (RANS) equations is applied, which results in the Volume Averaged Reynolds Averaged Navier-Stokes equations (VARANS) (2.21) to account for permeable structures by including the effect of the porosity (Jensen et al., 2014). This hydrodynamic model uses filter velocity in their version of the Navier-Stokes equations:

$$\nabla \cdot \bar{u}_f = 0 \tag{2.20}$$

$$(1 + C_m)\frac{\partial}{\partial t}\frac{\rho \bar{u}_f}{n_p} + \frac{1}{n_p}\nabla\frac{\rho}{n_p}\bar{u}_f\bar{u}_f^T = -\nabla p^* + g\chi\nabla\rho + \frac{1}{n_p}\nabla(n_p\mu\nabla\frac{\bar{u}_f}{n_p}) - F_p \tag{2.21}$$

With:

$$C_m = \gamma_p \frac{1 - n_p}{n_p} \tag{2.22}$$

Here, C_m is the added mass coefficient, n_p is the porosity of the permeable structure, F_p is the resistance from the permeable structure and u_f is the filter velocity. The added mass coefficient can be calculated by (2.22) as defined in Van Gent (1995), where γ_p is an empirical coefficient, which is determined to be 0.34.

Wave generation
To analyse wave-structure interaction within a numerical wave flume, generation and absorption of free surface waves within the wave flume are needed. A variety of numerical wave-maker methodologies have been suggested in the literature. For wave generation, five methods are well known: the Relaxation Zone Method (RZM), Static Boundary Method (SBM), Dynamic Boundary Method (DBM), Mass Source Method (MSM) and Impulse Source Method (ISM). For absorption of waves in the numerical wave flume, six different methods are available: RZM, SBM, DBM, Numerical Beach implementations (NB), geometrically sloped beaches and the cell stretching method (Windt et al., 2019). A brief description of all the different techniques is given in Appendix B.

The relaxation zone method is implemented in the $Waves2Foam$ toolbox and is publicly available. This toolbox is used in Jacobsen et al. (2012), Jensen et al. (2014) and van Gent et al. (2017), among others. The RZM imposes functions for $U(x,t)$ and $\eta(x,t)$ at the boundary of the domain, based on wave theory. These solutions are defined as the target solutions, both represented by $\phi_{target}(x,t)$. The relaxation zone is used to blend the target solution $\phi_{target}(x,t)$, with a computed solution, $\phi_{computed}(x,t)$, over the length of the relaxation zone L_R with the following formulas:

$$\phi(\mathbf{x},t) = \chi_R(x)\phi_{\text{computed}}(\mathbf{x},t) + (1-\chi_R(x))\,\phi_{\text{target}}(\mathbf{x},t) \tag{2.23}$$

$$\chi_R(x) = 1 - \frac{\exp\left(\frac{x}{L_R}\right)^{3.5} - 1}{\exp(1) - 1} \quad with \quad x \in [\ 0 \quad L_R\ ] \tag{2.24}$$

In these formulas, ϕ is the velocity of the indicator function γ, and χ_R is the weighting function. At the boundary of the domain, this function equals 0 and at the end of the relaxation zone, it has increased to 1. The horizontal coordinate x has a value between 0 and L_R. Relaxation zones are also used to avoid reflection of waves from outlet boundaries and further to avoid waves reflected internally in the computational domain to interfere with the wave maker boundaries (Jacobsen et al., 2012).

Flow resistance in filter
The analyzed structure within this thesis is a sea dike. The dike is a permeable structure consisting of a filter layer and a block revetment that allows water to flow from the surface through the top layer to the filter layer and the other way around. Volume Averaging is applied over the Reynolds Averaged Navier-Stokes equation (VARANS) to account for the porosity. By performing this operation, the effects of the porous media flow have to be introduced into (2.21) through the resistance from the permeable structure (F_p) and the added mass coefficient (C_m). In practice, the flow through the porous media experiences frictional forces, which result in energy dissipation. The energy dissipation in the porous media cannot be resolved due to the volume averaging of the RANS equations. To account for the resistance from the permeable structure, the extended Darcy-Forchheimer equation (2.25) is used as a closure model. Moreover, the influence of frictional forces on the inertia is included by introducing the added mass coefficient C_m.

$$F_p = a\rho u_f + b\rho \left\|u_f\right\|_2 u_f \tag{2.25}$$

The ratio between the two terms in (2.25) determines the flow behaviour; if the first term dominates the flow behaves laminar, while domination of the second term implies a turbulent flow. The magnitude of the first term is influenced by resistance coefficient a and the magnitude of the second term is influenced by resistance coefficient b. In literature, there are several approaches to determining coefficients a and b. The first expression for the resistance coefficients is formulated by Engelund (1954). The expression contains a relation between porosity (n_p), viscosity (ν), and grain diameter (d_{n50}) for steady flow. Most

recent expressions in literature for a and b are proposed by Van Gent (1995), in which the known expressions are extended with the effect of oscillatory flows.

$$a = \alpha \frac{(1-n)^2}{n^3} \frac{\nu}{d_{n50}^2} \tag{2.26}$$

$$b = \beta \left(1 + \frac{7.5}{KC}\right) \frac{1-n}{n^3} \frac{1}{d_{n50}} \tag{2.27}$$

In these expressions, α and β are empirical coefficients. KC is the Keulegan-Carpenter number for stones, defined as $KC = u_m T/(nD_{50})$, where u_m is the maximum oscillating velocity and T the period of the oscillation. The KC number accounts for the effects of oscillatory flows. The drag forces are higher under oscillatory flows than in the case of stationary flows. The KC number for the stones is not an easy parameter to estimate, because of the rapid damping of the wave energy through the permeable structure (Jacobsen et al., 2015). Low KC-values imply a large influence of the oscillatory flow on the drag force while for large KC-values this influence becomes negligible. For a more extensive reflection of KC is referred to Jacobsen et al. (2015).

Turbulence closure model

The (VARANS) describes the hydrodynamics for the time-averaged part of the Reynolds decomposition. However, the fluctuating part of the velocity (u') still arises in the Reynolds stress tensor which results in an unknown term in (2.18). This term represents the influence of turbulence in the flow. To approximate the Reynolds stresses, additional equations are needed. This phenomenon is known as the turbulence closure problem (Hanjalic, 2004). Multiple turbulence models are derived to account for this problem and approximate the Reynolds stresses. Despite the development of various turbulence models, in practice, (RANS) models without turbulence closure models are also utilized. Ignoring the turbulence model turns out to be a valid approximation in many engineering applications (Jensen et al., 2014). In the case of wave-structure interaction with permeable structures, the main source of energy dissipation happens within the porous media. The negligible impact of a turbulence model is among others shown in Higuera et al. (2013a) in which a $k-\epsilon$ turbulence closure model is used, Higuera et al. (2013b) that uses a $k-\omega-SST$ turbulence model and Mata (2021) in which a constant eddy viscosity turbulence closure model is used.

Volume of fluid

The (VARANS) equations that are used in the CFD model are solved together with a tracking of the free surface with a Volume of Fluid (VOF) approach. The governing formula is given in (2.28). This equation contains an indicator function γ that represents the fraction of the fluid present in a certain cell. γ is a value within the interval $[0, 1]$, 0 implies that a cell is completely filled with air, while 1 indicates that a cell is completely filled with water. The advection equation employed in the VOF approach is the standard method available in OpenFOAM, and is presented below:

$$\frac{\partial \gamma}{\partial t} + \frac{1}{n_p}\left[\nabla u\gamma + \nabla u_r(1-\gamma)\gamma\right] = 0 \tag{2.28}$$

In this equation, u_r is the relative velocity between the liquid velocity (u_l) and the gas velocity (u_g). It is assumed that the contributions of (u_l) and (u_g) to the evolution of the free surface are proportional to the corresponding phase fraction. The velocity of the effective fluid (u) in a (VOF) model is therefore a weighted average of (u_l) and (u_g) (Berberović et al., 2009):

$$u = \gamma u_l + (1-\gamma)u_g \tag{2.29}$$

2.5. Conclusion

The first part of this chapter describes the physical processes behind the interaction of waves and dikes, and how this could lead to the failure of a placed block revetment. During wave loading, uplifting forces could occur in the filter layer. These uplifting forces result from pressure differences on the top layer and in the filter layer. The pressure differences are the largest during maximum wave run-down and during the wave impact. The most vulnerable location of the revetment is just above the run-down

point. Besides the wave conditions, also some revetment properties determine the maximum uplifting forces that can occur. The ratio between the permeability of the top and filter layer determines the maximum forces for a given wave load. This ratio is called the leakage length. When creating a CFD model that is capable of simulating realistic loads on a revetment, it is important that the described processes and principles are well reflected within the numerical model. Therefore, the described theory will be considered when setting up a CFD model and by reflecting on the performance of this model.

The second part of this chapter focuses on numerical modelling of the interaction between waves and hydraulic structures. Following an introduction to various types of CFD models, the focus has shifted to NS models that employ the VOF method for their solution. Equations that are solved in NS models are described and the state of art is given for topics such as wave generation, porous media flow and turbulence modelling. A challenging part of CFD modelling is to accurately simulate the flow through porous media. For the wave-structure interaction of placed block revetments, the flow through the structure is crucial since it determines the magnitude of the uplifting forces in the filter. To obtain numerical test results that closely match the physical test results, it is crucial to ensure that the model exhibits the same hydraulic behaviour in the layers as in the physical experiment. If there is no flow resistance in these layers, for example, the hydraulic head on the top layer may exactly match the hydraulic head in the filter layer. However, in CFD modelling, some schematizations are necessary, such as modelling the top layer as a two-dimensional layer. These schematizations can significantly affect the flow resistance through the structure and impact the model's performance. Therefore, it is essential to consider porous media flow in the CFD model and its relationship with physical test results.

3

Physical model test

Chapter 3 gives an overview of the Delta Flume tests performed by Deltares. In Section 3.1 the research of Deltares is described, as well as why the Delta Flume tests are used in this study. In Section 3.2 the Delta Flume set-up is explained in more detail. Next, in Section 3.3 is described how the data is pre-processed before it could be used. Subsection 3.4 gives an overview of the results from the physical model tests, that are relevant to compare with the results from the numerical simulations. In the last subsection, conclusions are drawn based on observations from the physical tests.

3.1. Introduction

The goal of this thesis is to investigate whether it is possible to accurately model the hydraulic loads on a placed block revetment by CFD modelling. To validate the results obtained from numerical simulations, the data obtained from the Delta Flume tests performed by Deltares, as described in Klein Breteler and Mourik (2020) are used. The Delta Flume tests are part of a research that is performed to investigate the influence of transitions (on the outer slope of a dike) on the stability of placed block revetments during wave impact. Along the Wadden Sea, a lot of dikes are built with a top layer consisting of block revetments along the lower section, and asphalt along the upper section. An example of such a dike is given in Figure 3.1. The transition is approximately located between NAP +2m and NAP +2.5m, which is within the wave impact zone during storm conditions. Before the research, this location of the transition was supposed to be unfavourable for the stability of the block revetment. However, the research of- Klein Breteler and Mourik (2020) concluded that the difference in hydraulic head over the top layer can be neglected for a wave steepness of 2% and that the influence of the transition is minimal for a wave steepness of 3% to 4%.

Figure 3.1: A dike along the Wadden Sea with both a placed block revetment and asphalt on the top layer.

As the influence of the transition is minor, the Delta Flume tests are particularly appropriate for the present study. The physical tests concern setups in which a placed block revetment is exposed to breaking waves. As a result of wave-structure interaction, uplifting forces are generated during these tests. Pressure transducers are placed both on the top layer and in the filter layer, which means that

the magnitudes of the forces could be determined. The physical tests are performed at different water levels and varying wave conditions, which makes this study suitable for the validation of the CFD model.

3.2. Model set-up Delta Flume

The Delta Flume has the possibility to test wave-structure interactions on a 1:1 scale. The toe of the dike is located 164 meters from the wave paddle. The slope is 1:3,6 and applied without a berm. This slope can be divided into three sections. The lower and upper sections are made of concrete. The middle section, which is located slightly below the still water level, consists of three layers. A C-star block revetment of 17.5 cm is placed on top of a filter layer with a thickness of 15 cm. The used filter material has a diameter of 20-30 mm, which is relatively coarse for a filter layer. Coarse material in the filter layer leads to a relatively high permeability (k) which also leads to a large leakage length λ. As a result, larger hydraulic head differences over the top layer are measured compared to a situation with a small leakage length. This principle is explained in Section 2.7. The deepest layer consists of impermeable sand cement. The core of the dike is completely made out of sand. Nevertheless, no infiltration of water occurs because the core is completely covered by impermeable layers. Figure 3.2 shows the configuration.

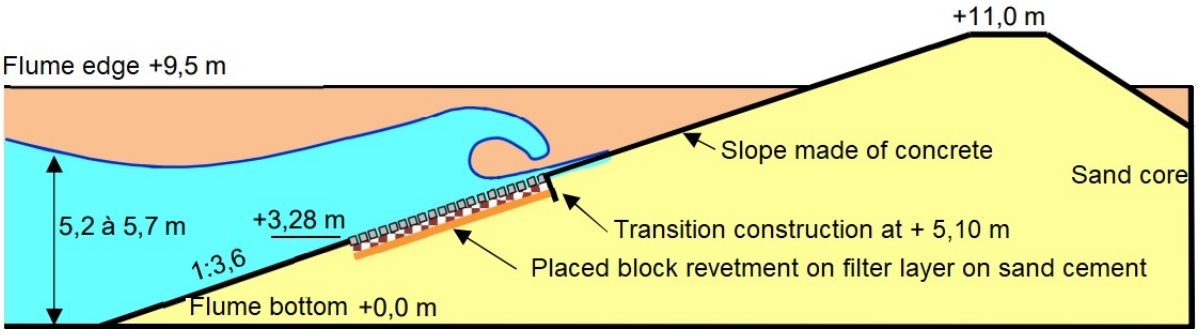

Figure 3.2: Vertical cross-section of model set-up in the Delta flume. (Klein Breteler & Mourik, 2020).

In total, 13 tests were conducted which differ in wave steepness, wave height and water level. Tests 1-6 are performed with a wave steepness of 2%, tests 7-10 with a wave steepness of 3% and tests 11-13 with a wave steepness of 4%. For a wave steepness of 2% the influence of the transition is negligible. Tests 1-6 are therefore most suitable to use as a case study. The applied water level varies per conducted test, with a minimum water level of 5.2 meters and a maximum water level of 5.85 meters. The transition from C-star blocks to concrete is located at a height of Y = 5.1 m. As a result, for tests 2,3 and 4, the wave impact will be on the concrete layer above the placed block revetment. At the placed block revetment, mainly quasi-static wave loads will be registered. Physical tests 1, 5 and 6 are performed with lower water levels. As a result, the wave impact took place on the placed block revetment. Mimicking these setups could be used to reflect on the process of wave breaking and the rise of uplifting forces due to high filter pressures. Specifications of the hydraulic conditions from the physical tests can be found in Table 3.1.

During the physical tests, the wave height is measured by 17 different wave gauges that are present in the Delta Flume. In the dike that has been built for this research, a total of 30 pressure transducers are placed within the structure. 19 pressure transducers are placed on the top layer and 11 in the filter layer. The locations of the measuring devices are listed in Appendix C.

3.3. Data pre-processing

The pressure transducers on the top layer and in the filter layer are used to determine the hydraulic loads on the placed block revetment. Before the data is appropriate to use, pre-processing of the data set is needed. The first adaptation is removing noise from the time signal. Within the time signal, high peaks consisting of only 1 sample are registered on a regular basis. This phenomenon is only observed for devices placed on the top layer. In Klein Breteler and Mourik (2020) this is explained by grains that cause an impact on the cover of the measuring devices. Around the peaks the signal is

relatively constant, therefore removing peaks consisting of 1 sample is preferred.

To determine the difference in hydraulic head over the top layer, the filter pressure and the pressure on the slope must be measured at exactly the same location, i.e. within the same line perpendicular to the slope. In the Delta Flume tests, the pressure sensors in the different layers are not located exactly above each other. To account for this situation, for missing locations the pressure is determined by linear interpolation of data from surrounding measuring devices. These locations are indicated as 'virtual locations'. For the upper part of the top layer, virtual pressure transducers are located exactly in the middle of the neighbouring devices. In the filter layer, the virtual devices are located in line with the virtual devices of the top layer, perpendicular to the slope. Figure 3.3 gives an overview of the situation. In Appendix C the coordinates are listed in tables.

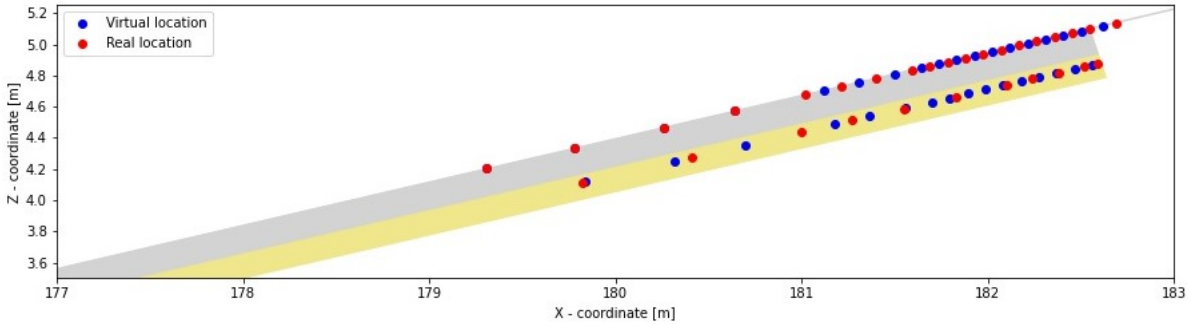

Figure 3.3: Location pressure transducers.

The third step is to convert the unit of the measured pressure. The sampling frequency of the pressure transducers is 1000 Hz and the pressures are measured in $[kN/m^2]$. To compare devices that are placed at different heights, it is more convenient to know the hydraulic head $[m]$ at the different locations of the sensors. Therefore, the pressure $[kN/m^2]$ is converted to a hydraulic head $[m]$ with the use of formula 2.8.

The last step of data pre-processing is the calculation of a time-moving average of the time series. This is done to minimize the remaining noise or any other coincidences in the time signals. The time series are subsequently filtered by performing a time moving average with formula 3.1 as is done in Klein Breteler and Mourik (2020). In this formula, $\phi_{t,vgem}$ is the weighted average of the hydraulic head at time t [m], ϕ_{t+n} the hydraulic head in the original data, n samples after time t [m] and f_{t+n} a weighting factor corresponding to ϕ_{t+n} (-). The different weighting factors are listed below the equation.

$$\phi_{t,vgem} = \frac{\phi_{t-2} \cdot f_{t-2} + \phi_{t-1} \cdot f_{t-1} + \phi_t \cdot f_t + \phi_{t+1} \cdot f_{t+1} + \phi_{t+2} \cdot f_{t+2}}{f_{t-2} + f_{t-1} + f_t + f_{t+1} + f_{t+2}} \tag{3.1}$$

f_{t-2} = 0.30
f_{t-1} = 0.85
f_t = 1.00
f_{t+1} = 0.85
f_{t+2} = 0.30

3.4. Results Delta Flume

Data obtained from the wave gauges provides information about the waves that propagate toward the structure. This data is used to make sure that the structure in the wave flume and the structure in the numerical model both are subjected to the same wave heights and wave periods, although the wave trains are not necessarily the same. Data obtained from the pressure transducers on the slope and within the filter layer provide information about the hydraulic loads themselves. The normative hydraulic

load for a placed block revetment is the difference in the hydraulic head over the top layer. For different locations at the slope of the dike, the pressure is measured on both the top layer and the filter layer. Combining this information could provide insight into the distribution of the difference in hydraulic head over time, for a certain location. In the following subsections, the data from both the wave gauges and pressure transducers are analysed in order to obtain results that can be compared to the results from the numerical simulation.

3.4.1. Wave gauges

In the Delta Flume, 17 wave gauges were present. The measured wave height equals the total wave height which is the summation of the incoming wave height and the reflective wave height. In a perfect representation of the physical test setup in the CFD model, the incoming wave height, reflection coefficient (R) and the total wave height will all be the same. In practice, the reflection coefficient (R) could differ because of the way that structural properties are schematized (e.g. porosity, roughness) and the numerical diffusion in the CFD model. Due to these variations, the total wave heights may differ even for similar incoming waves. Consequently, it is not recommended to compare the total wave heights. Instead, to accurately compare waves, it is necessary to separate the incoming wave height from the wave signal. This is done by a least squares method proposed by Mansard and Funke (1980). This method requires simultaneous measurement of the waves at three locations in the flume which are in reasonable proximity to each other and are on a line parallel to the direction of wave propagation. Wave gauges 1, 2 and 3 are used to perform this separation method. To compare the incoming wave heights, the variance density spectra are calculated. The purpose of describing waves with a spectrum is to describe the water level elevation as a stochastic process and to characterise all possible time records that could have been made under the conditions of the actual observation. (Holthuijsen, 2007). The variance density spectra for tests 1-6 are depicted in Figure 3.4.

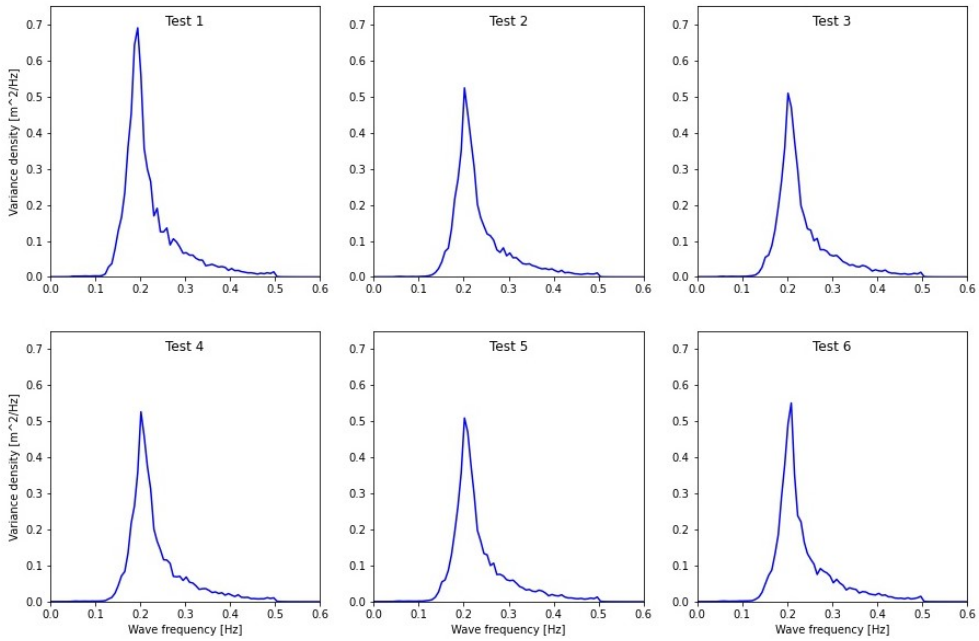

Figure 3.4: Variance density spectra of Delta Flume tests.

Based on the wave spectra, also the zeroth order moment (or variance, m_0), peak period (T_p), significant wave height (H_{m0}) and spectral periods (T_{m01}, T_{m02} and $T_{m-1,0}$) are calculated. In order to calculate the number of waves (N), the mean wave period (T_m) and the wave heights ($H_{1/3}$, $H_{1/10}$ and $H_{2\%}$), a zero down crossing method is applied on the wave gauge data. The output contains a list with both the individual wave heights and the individual wave periods. Minor fluctuations in surface elevation that occur over a short period can sometimes be mistakenly identified as waves, even though they are not generated by the wave paddle. It was decided to remove 'waves' with a wave period $T < 1s$. From Figure 3.4 it becomes clear that a spectral component with a frequency $f > 0.8$ i.e. $T < 1.25s$ has

almost no influence on the total variance. All the variables mentioned in this subsection are listed in Table 3.1.

Variable	Unit	Test 1	Test 2	Test 3	Test 4	Test 5	Test 6
h	m	5.2	5.85	5.72	5.59	5.45	5.32
N	[-]	1075	1174	1169	1177	1179	1166
T_m	s	4.30	3.94	3.93	3.93	3.92	3.96
$H_{1/3}$	m	0.82	0.71	0.71	0.71	0.71	0.71
$H_{1/10}$	m	1.02	0.89	0.89	0.90	0.89	0.90
$H_{2\%}$	m	1.24	1.10	1.09	1.10	1.09	1.10
H_{m0}	m	0.85	0.73	0.73	0.74	0.73	0.74
m_0	m^2	0.045	0.034	0.034	0.034	0.034	0.034
T_p	s	5.14	4.96	4.96	4.96	4.96	4.87
T_{m01}	s	4.45	4.25	4.25	4.25	4.25	4.22
T_{m02}	s	4.24	4.09	4.08	4.09	4.08	4.05
$T_{m-1,0}$	s	4.83	4.54	4.55	4.56	4.56	4.55

Table 3.1: Wave statistics Delta Flume tests.

From Table 3.1 it becomes clear that two different wave conditions are conducted in the Delta Flume. The table shows approximately the same wave characteristics for tests 2-6. Also in Figure 3.4, similar spectra can be found for these tests. However, it is still useful to include the test results from tests 2-6 in this research because these tests differ in water level. The measuring devices on the structure in the Delta Flume were positioned approximately 4 meters apart. To obtain a more comprehensive understanding of the pressure distribution along the slope, it would have been beneficial to space out the measuring devices over a greater distance. Nonetheless, by combining the results from tests 2-6, valuable insights into the pressure distribution can be obtained over a wider range for the given wave conditions.

3.4.2. Pressure transducers

Figures 3.5 represent the processed data from the pressure transducers. Each row corresponds to a test, ascending from test 1 up to test 6. The first column corresponds to the pressure transducers on the top layer and the second column to the pressure transducers in the filter layer. Column 3 shows the differences in the hydraulic head over the top layer in the upward direction. The maximum difference in the hydraulic head during a wave cycle, will not necessarily occur at the same moment in time as the maximum pressures on the top layer or in the filter layer (i.e. figures in column 3 is not obtained by subtracting values from the figures in column 1 from values in figures of column 2.) In all the figures, red, blue and green markers are plotted above each other for several locations. Every set of markers corresponds to a pressure transducer located on the slope of the structure. The markers represent the 2%, 10% and 33% exceedance values for the measured pressures respectively.

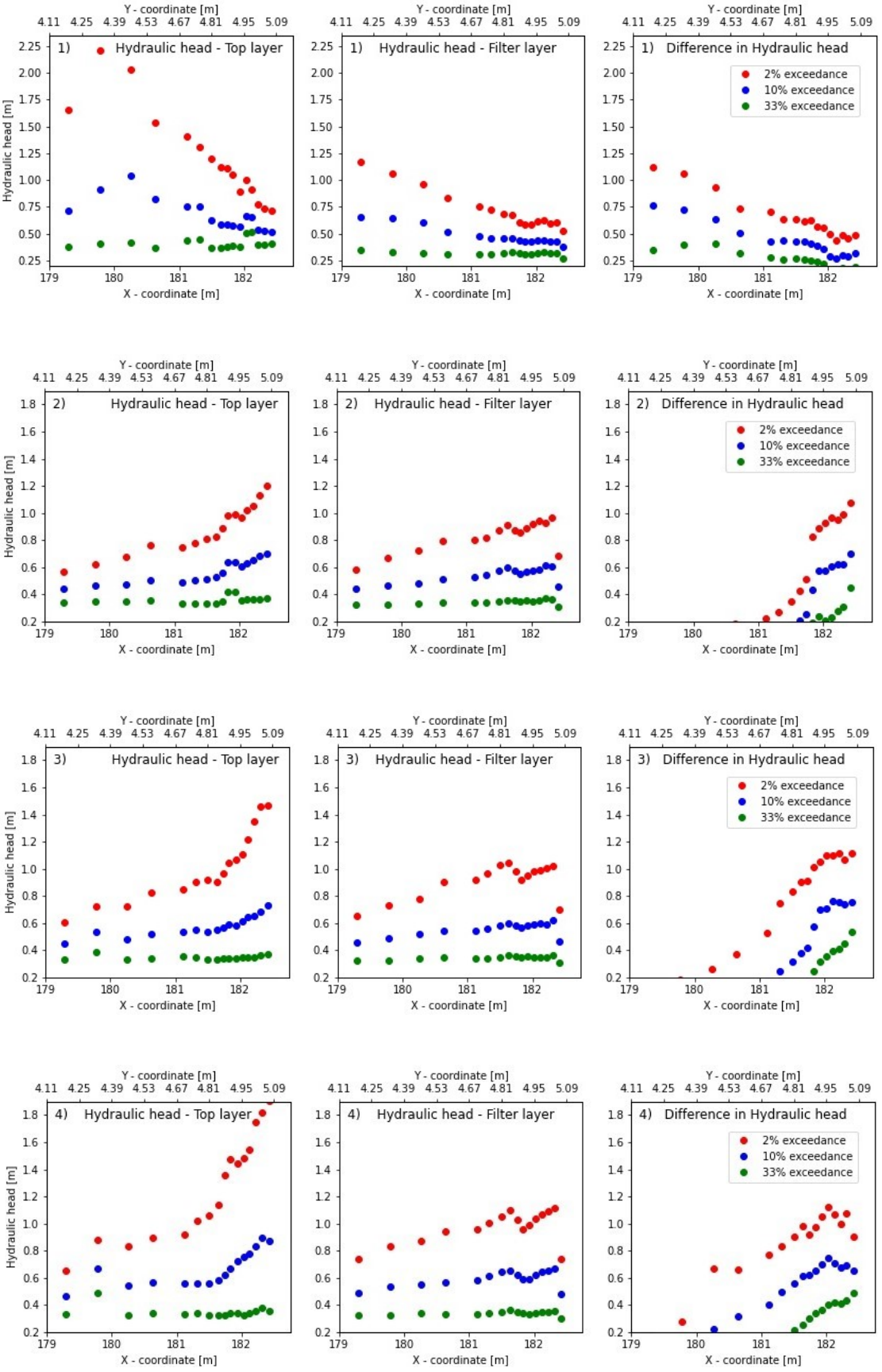
1) Hydraulic head - Top layer
1) Hydraulic head - Filter layer
1) Difference in Hydraulic head
2) Hydraulic head - Top layer
2) Hydraulic head - Filter layer
2) Difference in Hydraulic head
3) Hydraulic head - Top layer
3) Hydraulic head - Filter layer
3) Difference in Hydraulic head
4) Hydraulic head - Top layer
4) Hydraulic head - Filter layer
4) Difference in Hydraulic head
2% exceedance
10% exceedance
33% exceedance
Y - coordinate [m]
X - coordinate [m]
Hydraulic head [m]

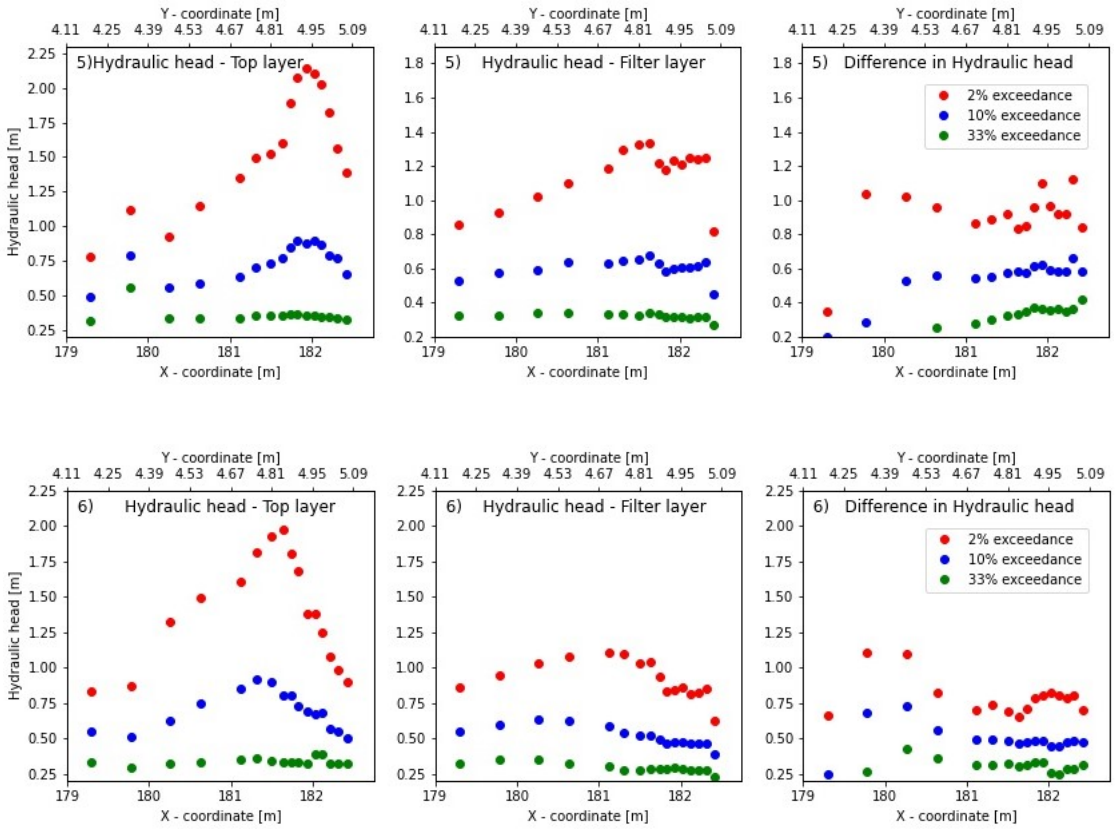

Figure 3.5: This figure shows the processed data from the pressure transducers in 6 different physical flume tests. The first row of figures corresponds to test 1 and the successive rows correspond to respectively tests 2-6. The first column shows the measured hydraulic head on the top layer for the different tests, the second column shows the hydraulic head in the filter layer and the third column the maximum (upward) difference in hydraulic head.

3.5. Analysis of results

Based on the processed data as described in the previous section, multiple observations have been made. A summation is given of observations that could be relevant when comparing the physical and numerical simulations. If applicable, the observations are related to the theory presented in Chapter 2.

Wave gauges

- In tests 2-6 the same wave conditions are applied. The water level varies between 5.85m and 5.32m. Combining these results gives a more comprehensive understanding of the pressure distribution along the slope.
- Test 1 yielded the highest significant wave height, and a water level of 5.2 m was applied. Consequently, the majority of the breaking waves will hit the slope within the range covered by measuring devices. As expected, the highest pressures on top of the placed block revetment are measured in test 1.
- A wave steepness of 2% was applied on the same slope in all the tests (1-6), which kept the Iribarren number (ξ) constant across the experiments. The data from the physical tests only allows for validating the CFD model for a single breaker type. However, a value of $\xi = 1.9$ is found, indicating plunging breakers. This breaker type generates the most critical loads, making it the most relevant for this study.

Pressure transducers

- In tests 1, 5 and 6, the wave impacts are registered on top of the placed block revetment. This could be observed by the peak in the figures that show the hydraulic head on the top layer (first

column). For these three tests, measuring devices are located at the depth where waves with a wave height equal to the significant wave height are expected to break. The theory suggests that for these tests, the majority of the peak pressures will take place in the range covered by measuring devices. The results are in line with this principle.

- In tests 2, 3 and 4, the majority of the wave impacts are not registered on top of the placed block revetment. The increase in the exceedance values suggests that the wave impact will take place at the asphalt slope above the placed block revetment. Again, this is in line with the theory. The water levels in these tests were relatively high, resulting in a water depth at the sensors that exceeded the breaker depth for wave heights equal to the significant wave height.
- Tests 2-6 show a rather constant distribution of the hydraulic head in the filter layer over the slope. It can be concluded that there is no significant change in the hydraulic head in the filter layer after the point of wave breaking. The maximum hydraulic heads in the wave impact zone are similar to the maximum hydraulic heads before wave breaking. It can be concluded that the maximum pressures originate from quasi-static wave loads. The energy from dynamic wave loads dissipates after the impact with the top layer.
- Test 1 shows a decrease in the distribution of the hydraulic head in the filter layer. When the water depths approach $h = 0m$, the quasi-static wave loads decrease.
- From tests 2, 3 and 4 it becomes clear that a certain distance before the point of wave impact, no significant differences in the hydraulic head are measured. From a theoretical point of view, it is clear that no uplifting forces will occur below the run-down point. This is in line with the observations.
- All the performed tests show mainly differences in hydraulic head at locations where the highest pressures on the top layer are measured. It was already concluded that these pressures result from dynamic wave loads. This observation is consistent with the theory that variations in hydraulic head over the top layer occur as a result of dynamic wave loads.

3.6. Conclusion

All the discussed observations are in line with the theory presented in Chapter 2. The physical test results show clearly differences in hydraulic head for different test conditions. The obtained data is therefore suitable to use for the validation of the CFD model. The data from the wave gauges can be used to compare and validate the wave generation and propagation in the numerical model. The hydraulic heads on the top layer as measured in the Delta Flume provide information about the breaking process of the waves by showing different pressure distributions for quasi-static and dynamic wave loads. This information can be used to reflect on the breaking process within the CFD model. To analyse the flow through the layers, the differences in hydraulic heads need to be compared. In the physical tests is observed that no differences in hydraulic head arise from quasi-static wave loads. Only the dynamic wave loads within the wave impact zone lead to differences in hydraulic head. It is interesting to check whether this physical principle is captured within the numerical model.

4

Numerical model set-up and validation

Multiple simulations have been performed to analyse the wave loads on placed block revetments. This chapter has the purpose to find the best model settings and to determine which values to use for the empirical coefficients. The first section describes the approach and the consecutive steps that have been taken to derive the final model setup. Thereafter, the general settings of the model are discussed. This includes a description of the flume layout, the layer designs, the spatial and temporal resolution of the grid and the generation of the waves within the CFD model. The goal is to simulate similar wave loads as measured in the physical model tests described in Chapter 3. Therefore, the properties and dimensions of the CFD model are based on the structure in the Delta Flume. The third section of this chapter shows the determination of the resistance coefficients α and β. This is done for all the continuum layers separately. The chapter ends with an overview of the final settings to simulate the wave loads on the placed block revetment.

4.1. Approach

A CFD model is created to investigate the possibility of simulating realistic wave loads on placed block revetments. Section 2.1.1 describes how a pressure difference over a placed block revetment will result in an uplifting force on the revetment. From this section, it became clear that the flow through the top and filter layer mainly determines the loads on the revetment. However, the CFD model that is created in OpenFOAM is a two-dimensional model, therefore a schematization of the top layer has to be applied. Two different schematizations are proposed and compared based on their performance. This chapter aims to find the best settings for the OpenFOAM model to simulate wave loads. To do this in a structured way, the following consecutive steps have been taken to achieve the final settings:

- Two different schematizations of the layers are made to schematize the actual layers in the structure. Dimensions and properties are based on the physical model set-up that is described in Chapter 3.
- A grid is designed and general settings are chosen based on the literature and the comparison with the physical model tests.
- Empirical coefficients α and β are determined for all the considered porous layers.
- A favourable layer schematization is chosen based on the performance of the models in the different simulations.
- An overview of the final settings is given.

4.2. General settings

4.2.1. Computational domain

To mimic the Delta Flume tests as described in Chapter 3, a 2DV OpenFOAM model is created. The domain of the model has a length of 249.79 m and a height of 11.50 m. The toe of the dike is located at 164,19 m of the relaxation zone. This is the same distance as the distance between the wave paddle and the toe of the structure in the Delta Flume. Also, the dimensions of the dike as well as the locations of the wave gauges are similar to these dimensions and locations in the physical tests. However, the landward slope of the dike is not included in the domain of the OpenFOAM model. Only the wave-structure interaction at the seaside is of interest, and the reduction of the domain decreases the calculation time of the model. The total length of the placed block revetment is 6.6 meters. The placed block revetment consists of a top layer placed on a filter layer. Together these layers form the area of interest within the model. Figure 4.1 gives an overview of the situation. In this figure, the still water level is depicted at a height of 5.2 meters which is the case in simulation 1. This level will increase up to 5.85 meters in simulations 2-6.

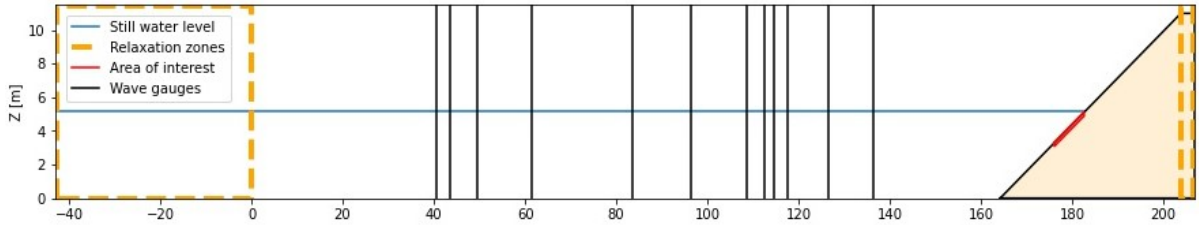

Figure 4.1: Flume layout in OpenFOAM

4.2.2. Boundary conditions

On the left side of the domain, the model starts with a relaxation zone of 43 m, which corresponds to the deep water wavelength (L_0). Within this zone, waves are generated and travel in the direction of the dike. Reflected waves that arrive from the opposite direction are absorbed to prevent interference with the boundary of the domain. On the right side of the domain, a relaxation zone is not necessary. The structure has a height of 11.5m which is high enough to prevent overtopping from happening. The bottom of the numerical flume and the impermeable structure elements (e.g. lower slope, upper slope and the placed block revetment) in the CFD model have closed boundaries. At these boundaries, the numerical model does not account for any shear stresses. Effects of bottom friction have been neglected. This is considered acceptable since measurements show no important decay in wave heights along the flume, indicating that the physical effect of bottom friction is negligible. Also, the surface friction of the blocks of the placed block revetment has been neglected. This is considered acceptable since the friction by the porous media flow is much larger than the surface friction. However, it is important to take into account the absence of these shear stresses when interpreting the model results.

4.2.3. Layer schematization

The area of interest consists of the top layer and the filter layer. Section 2.1.1 describes how wave-structure interaction can lead to instability of the block revetment and Section 2.3 elaborates on which parameters will affect the stability of the structure. The top layer's linearized permeability (k') is one of the variables that appear in formula (2.7). In reality, the top layer consists of C-star blocks that are impermeable. The shape of the blocks results in a pattern with multiple open spaces between these blocks. This pattern determines the flow regime through the top and filter layers. The flow regime in the structure is not considered in the analytical equation 2.16. This formula assumes a laminar flow which is not necessarily the case. However, this flow regime has an impact on the loads on the structure and needs therefore to be modelled correctly. There are multiple options to schematise the layers in the numerical model which could lead to different flow patterns. In this thesis, two different top layer schematizations will be considered. Different simulations should provide insight into the relationship between the flow through the layers and the measured pressures. The first schematization, referred to

as 'schematization 1', consists of a uniform and permeable top layer on top of a uniform filter layer. In the second schematization, referred to as 'schematization 2', the top layer consists of multiple blocks alternated by small gaps to ensure the permeability of the top layer. Both schematizations are depicted in Figure 4.2. In schematization 1, water can infiltrate into the top layer at any point on the surface and the flow within the porous medium is governed by the extended Darcy-Forchheimer equation (2.25). In schematization 2, water can infiltrate only through the gaps between blocks. In this region, the flow regime is affected by the boundary conditions applied on the surfaces of the blocks. The two schematization methods will result in different flow regimes in the top layer. The resistance on the flow will also be different. Simulations of the two schematizations must show if this results in differences in pressure distribution in the filter layer. Schematization method 2 seems to be more similar to the Delta Flume. However, there are no shear stresses presented in the gaps between the blocks. In schematization method 1 a porous flow is modelled instead of a flow between the blocks. The advantage of this method is the possibility to impose a resistance force on the flow. Both models will be compared to the results from the Delta Flume, in order to decide which schematization is favourable for modelling a placed block revetment. A more detailed description with dimensions per layer is given.

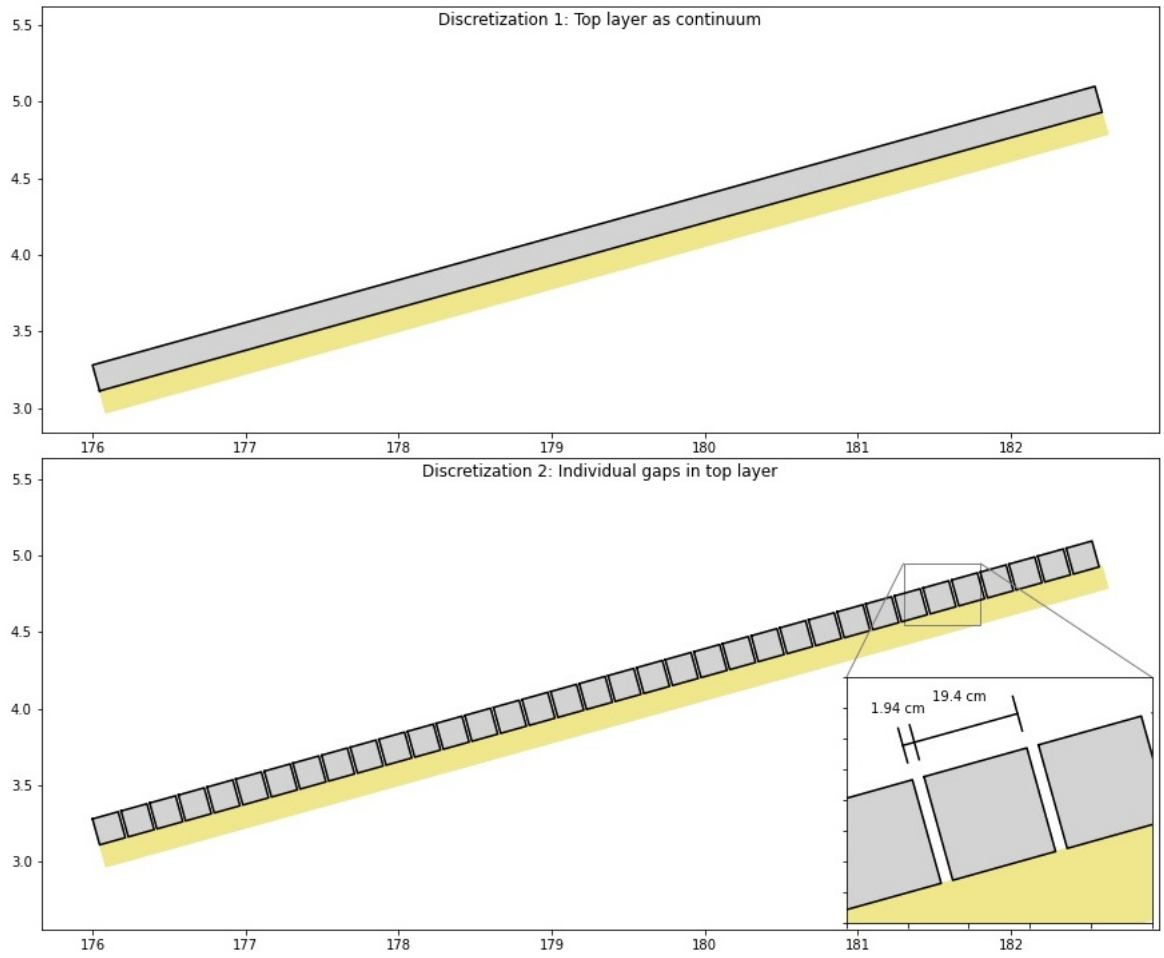

Figure 4.2: Schematization of layers in OpenFOAM model

Top layer schematization 1 (Top layer as continuum)
In schematization 1, the top layer is modelled as a continuum with a certain permeability. The porosity equals the percentage of openings in the surface of the top layer ($n = 0,103$). Also, a grain size has to be specified although the layer does not consist of grains in practice. The size of the grains determines the size of the pores in the medium which affects the flow regime. Grains and pores have the same order of magnitude in practice, therefore a grain size (d_{n50}) equal to the width of the open spaces of schematization 2 is chosen (e.g. $d_{n50} = 0,019m$). In Appendix D is the quantity of this fictional

grain size further analysed. The resistance in this layer that will be experienced by a water particle is approximated by the Darcy-Forchheimer equation (2.25). As a result, also quantities for the empirical coefficients α, β and the Keulegan-Carpenter number for stones (KC) had to be chosen. For the Keulegan-Carpenter number, a value of $KC = 10.000$ is chosen. By setting a high KC-value, the effect of an increased drag force under oscillatory flow is negligible. This principle is also applied in Jacobsen et al. (2018), in which a default value $KC = 10.000$ is used, leading to results that are in agreement with experimental data. The empirical resistance coefficients α and β are dependent on the case study in which they are used, and should therefore be determined. This will be described, later in this chapter.

Top layer schematization 2 (individual gaps in top layer)
In the second schematization of the top layer, the layer consists of individual blocks (impermeable), alternated by openings which allow for flow between the filter layer and the surface. The OpenFOAM model will simulate a two-dimensional case (2DV) that has the aim to imitate the physical Delta Flume tests described in Chapter 3. The geometry of the C-star blocks has to be translated into a two-dimensional design. In reality, the blocks are locked by surface friction between adjacent blocks. The revetment is designed in such a way that a row of C-star blocks fits into another row of C-star blocks that are orientated in the opposite direction. The pair of rows is smooth on both sides and placed adjacent to another pair of rows, covering the total surface. The longitudinal distance covered by the two rows is 19.4 cm, and the height of the blocks is 17.5 cm. An illustration of the revetment can be found in figure 4.2 and Appendix E. A surface that is covered by C-star blocks will consist of 10.3% open spaces. To keep the top layer schematization in the OpenFOAM model as simple as possible, the C-star block is schematized as a rectangular block with a height of 17.5 cm and a width of 19.4 cm, corresponding to the height and longitudinal distance of the C-star blocks in practice. The blocks are alternated by open spaces of 1.94 cm which results in the same ratio between covered surface and open spaces. Flow through the layer takes place between the blocks. The porous media flow is not relevant in this layer and there is no need to modify the default values for α, β and KC. Theoretically, the gaps themselves could be modelled as a porous medium to increase the resistance through the top layer. In that case, a modification of the empirical resistance coefficient should be considered. However, this schematization is not considered during this research.

Filter layer
The filter properties in the CFD model have been selected to closely mimic the physical set-up. In the Delta Flume, the grading of the filter material had a d_{n50} of 30 mm, which is relatively coarse for a filter layer (Klein Breteler & Mourik, 2020). However, in order to model large pressure differences over the top layer, a large leakage length was favourable in the physical tests. To ensure a high permeability of the filter layer, coarse filter material is utilized, with a corresponding porosity of n = 0.45 [-]. The thickness of the layer was (b = 15 cm). The grain size (d_{n50}), porosity (n) and layer thickness (b) were selected to be identical in the numerical model. Also, values for the empirical coefficients α and β have to be selected. The selection of the variables is described later in this chapter.

4.2.4. Spatial resolution

In order to obtain accurate and stable results, an appropriate computational grid is defined. In total, two different structure schematizations are tested and subjected to six different hydraulic boundary conditions. Therefore, twelve different situations could be distinguished and all may require different grid resolutions. However, to compare the results from all the simulations it is favourable to use the same spatial grid during all the tests. The finest required spatial grid for any of the simulations is used for all simulations. The size of the mesh varies over the domain. The background mesh is created using the utility BlockMesh. This background mesh is coarser than the mesh around the areas of interest. Consequently, the number of grid cells will be smaller compared to the situation in which the mesh refinement is applied over the entire domain, resulting in a reduction in the computational times as well. The mesh around the free surface is refined in order to model the wave propagation more accurately, and also the region around the top layer and filter layer are refined to predict the wave impact more accurately. The refinements are performed using the utility SnappyHexMesh. According to Pedersen et al. (2017), maintaining an aspect ratio of $\Delta x/\Delta y = 1$ within the entire domain improves both the accuracy and numerical stability of the model. The size of the background mesh is 0.4m which has led to reasonable computation times.

The first refinement region is around the free surface. In literature, different approaches are used to determine the minimum mesh size in order to accurately model the wave propagation. A minimum number of grid cells for both the wave height and wave length are commonly imposed. In Huang et al. (2022) 10 cells per wave height and 100 cells per wavelength are advised and in both Schmitt et al. (2020) and Pedersen et al. (2017) simulations have been performed for grid sizes varying between 5 cells per wave height to 20 cells per wave height. For this thesis, a refinement level of 2 (e.g. for each refinement level, the mesh size is divided by 2) is chosen around the free surface, which results in a grid size of 0.1m. For test 1 (table 3.1) this leads to 0.847/ 0.1 = 9 cells per wave height and 31.2/ 0.1 = 312 cells per wavelength, while for tests 2-6 (same wave conditions) this results in 0.739/ 0.1 = 8 cells per wave height and 29.7/ 0.1 = 297 cells per wavelength. This refinement is applied between 3.2 meters to 7.2 meters (over the entire horizontal domain) corresponding to a bandwidth of 2*H_{m0} below the still water level for test 1 (lowest water level), and 2*H_{m0} above the still water level in test 2 (highest water level). The grid sizes for the different mesh regions are listed in Table 4.3.

Mesh region	Zone in Figure 4.3	Grid size Δx*Δy [m x m]
Background mesh	1.	0.4 x 0.4
Mesh near the water surface	2.	0.1 x 0.1
Mesh around top and filter layer	3.	0.003 x 0.003

The normative layer schematization that determines the refinement around both layers is schematization 2. The gaps between the blocks have a width of 1.94 cm which require a very fine mesh to model a flow between the surface and filter layer. In practice, a refinement level of 7 (corresponding to a grid size of 0.003125 meters) was necessary to obtain stable solutions. After the refinement, approximately 6 cells cover the width of the gap between two blocks (0.0194/ 0.003125 = 6.208). The refinement covers the circumference of both layers. The applied spatial grid is depicted in Figure 4.3.

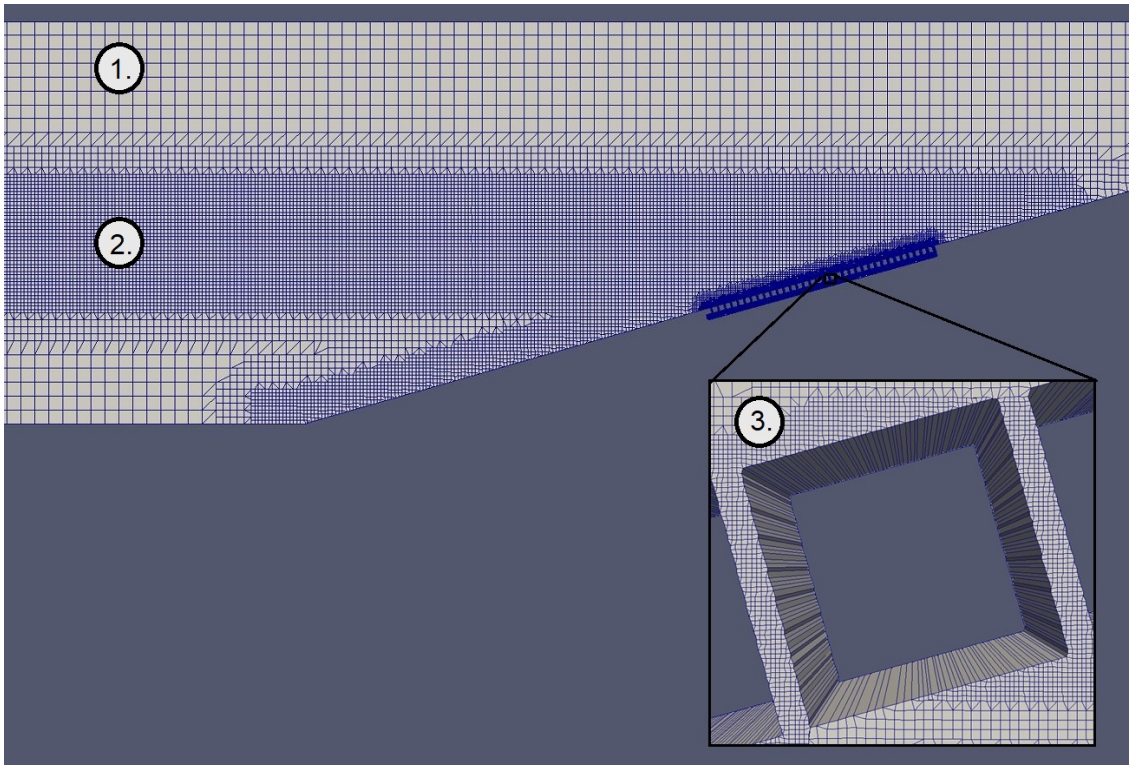

Figure 4.3: Grid OpenFOAM model

4.2.5. Temporal resolution

The aim of a CFD model is to derive a numerical solution that is as close as needed to the experimental observations. The solution generated by the numerical model is said to be convergent if the numerical solution converges to the exact solution if Δx & $\Delta t \rightarrow 0$ (Zijlema, 2015). To be convergent, a system has to be both consistent and stable. The stability of a numerical model is dependent on the applied numerical scheme, spatial resolution, velocity and the applied time stepping method. The available numerical schemes can be divided into schemes that use explicit or implicit time integration. Implicit schemes use both the solutions at the current time step and time step(s) ahead of the current time step. Implicit schemes have no stability requirements. A disadvantage of an implicit scheme is that such models are computationally expensive compared to explicit schemes. Explicit schemes calculate the solution at the next time step using the solutions from previous time steps. A CFD model that uses such a scheme, has to be checked for stability. The Courant Friedrichs Lewy (CFL) condition is a requirement for the stability of a finite difference scheme to a (non)linear hyperbolic partial differential equation. This condition is based on the fact that the numerical domain of dependence must contain the analytical domain of dependence (Zijlema, 2015). Formula (4.1) shows the CFL condition. The OpenFOAM model that is used in this thesis uses an explicit Euler scheme for solving the momentum equation and should therefore be checked on the CFL condition.

$$|\sigma| \equiv \frac{|u|\Delta t}{\Delta x} \leq C \tag{4.1}$$

In formula (4.1), u is the velocity, Δx is the spatial step size, Δt is the time step, and C is the Courant number. The Courant number is dependent on the model that is applied, and in this case, set to $C = 0.35$ by default. This value is prescribed for every time step. Δx is fixed by the grid and u is calculated. This means that Δt has either to vary per calculation or it has to be as small as its minimum value. A smaller time step than necessary is computationally unattractive, therefore an adaptive time step is applied.

4.2.6. Wave generation

In Appendix B several methods are discussed to generate waves in a CFD model. Relaxation zone techniques turn out to be the best method to use for this thesis. SBM can not be applied because the waves that have to be produced are not shallow water waves. DBM will be difficult because the wave paddle signal from the Delta Flume is not available, and both MSM& ISM require special absorption techniques. The relaxation zone techniques are implemented in the $waves2Foam$ toolbox, which is used by the OpenFOAM model. According to Jacobsen et al. (2012) the minimum length of the relaxation zone should be equal to one wavelength. Based on a maximum wave period of 6.5s and a water depth of 5.2 m, a wavelength of L = 42.58 m is found and the length of the relaxation zone is set to $L_R = 43m$. The OpenFOAM model is used to simulate a set of configurations in which two different hydraulic conditions are utilized at six different water levels. These hydraulic conditions should correspond to the hydraulic conditions that were used in the Delta Flume tests, as described in Chapter 3. By prescribing the same variance density spectra to waves in the numerical models, statistically, the same wave condition will be obtained. The spectra are depicted in Figure 3.4. Characteristics values of the wave fields are listed in the table below.

Variable	Unit	Test 1	Test 2	Test 3	Test 4	Test 5	Test 6
h	m	5.20	5.85	5.72	5.59	5.45	5.32
H_{m0i}	m	0.85	0.73	0.73	0.74	0.73	0.74
T_{pi}	s	5.14	4.96	4.96	4.96	4.96	4.87
m_{0i}	m^2	0.045	0.034	0.034	0.034	0.034	0.034
T_{m01i}	s	4.45	4.25	4.25	4.25	4.25	4.22
T_{m02i}	s	4.24	4.09	4.08	4.09	4.08	4.05
$T_{m-1,0i}$	s	4.83	4.54	4.55	4.56	4.56	4.55

Table 4.1: Target hydraulic conditions.

4.3. Determination of empirical coefficients

The resistance on the porous media flow is determined by the Darcy-Forchheimer equation (2.25). Empirical coefficients α and β needs to be defined for the porous layers. In order to do this, first the pressure signal on the top layer as predicted by the CFD model is compared with the measured signal from the physical tests for validation. Next, the pressure signals of the filter pressures are compared for different values of α and β. Based on the trends will be determined whether the signals are in reasonable approximability and which α and β values yield the best results. Figure D.1 shows a pressure signal on the top layer (blue) and in the filter layer (yellow) for six waves. During wave impact, the hydraulic head rises instantaneously. Thereafter, the pressures drop until the lowest pressures are reached during the maximum wave run-down. The pressures rise again when the next wave hits the slope. The pressure signal in the filter layer looks slightly different. During wave run-down, the pressure in the filter layer decreases at a slower rate compared to the pressure on the top layer due to flow resistance in the layers. At maximum wave run-down, an upward pressure difference over the top layer is observed. The hydraulic head on the top layer as depicted in Figure D.1 (blue) is measured by sensor 13, located at X = 181.12 m and Y = 4.98. The highest pressures are measured at this location, which yields the clearest results to use for validation. The yellow graph represents the hydraulic head in the filter layer measured by sensor 30. This sensor is located in the same line as sensor 13, perpendicular to the slope.

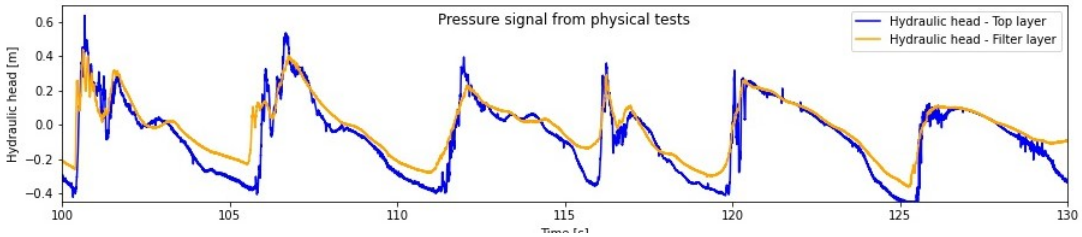

Figure 4.4: Hydraulic head measured by sensors 13 and 30 in the Delta Flume during test 1.

4.3.1. α and β values filter layer

The first porous layer that is considered is the filter layer. To determine the α and β values for this layer, a CFD model with top layer schematization 2 is used. Unlike schematization 1, no empirical values for the top layer have to be specified which makes α and β of the filter layer the only unknown variables. The pressure transducers in the CFD model are located at exactly the same locations as sensors 13 and 30 from the physical tests in order to compare the model predictions to Figure 4.4. The same wave conditions are applied, but random waves are generated. The obtained results will therefore only be compared on the trends that are observed.

Figure 4.5A show the pressure signals on the top layer and in the filter for the described CFD model under the default settings of the empirical coefficients (e.g. α = 1000 and β = 1.1). Again, the blue graph shows the hydraulic head on the top layer and the yellow graph the hydraulic head in the filter layer. The predicted hydraulic head on the top layer shows a similar trend as obtained from the physical tests. The hydraulic head rises instantly during wave impact, followed by a drop in pressure until maximum wave run-down is reached. At this point in time, the lowest pressures are observed. Thereafter, this cycle starts again.

The CFD model is able to predict the pressures on the slope of the structure. Next, the pressures in the filter layer will be considered. The magnitudes of α and β become relevant when modelling these filter pressures. Knowledge about the variation of α and β originates from theoretical considerations, physical experiments and numerical calibrations. The coefficients determine the relative importance of the linear and non-linear terms in the Darcy-Forchheimer equation i.e. if the flow behaves laminar or turbulent. In multiple studies, values for α and β are determined for different flow regimes and applications. Jensen et al. (2014) gives an overview of these studies. Van Gent (1995) found the ranges [0, 2780] for α and [0.36, 1.33] for β from laboratory experiments and suggested using the values $\alpha = 1000$ and $\beta = 1.1$. However, Losada et al. (2008) mentioned that under oscillatory flow and waves propa-

gating over slopes or breaking, values existing in the literature may not be valid since the experimental conditions for obtaining those values do not consider the wave-structure interaction correctly. As an alternative, Losada et al. (2008) suggested the values α=200 and β=0.8 for a breakwater core and α=200 and β = 0.7 - 1.1 for the top layers. Figures 4.5 A-D shows a time series of 2 pressure transducers in a series of simulations. In order to check the sensitivity of the empirical resistance coefficients, the quantities are changed consecutively. As a starting point, in simulation A the α and β as proposed by Van Gent (1995) are used. In simulation B, a smaller value for α is used while in simulation C a decrease of β is applied with respect to simulation A. In the last simulation, both coefficients are reduced. By decreasing the coefficients, the resistance in the filter layer is reduced. However, the results show hardly any changes in the pressure distribution in the filter layer. The minor influence of the reduction of α and β gives no reason to make adjustments in the default settings. Therefore, it is decided to use α = 1000 and β = 1.1 for the filter layer in the rest of the simulations that will be performed during this research.

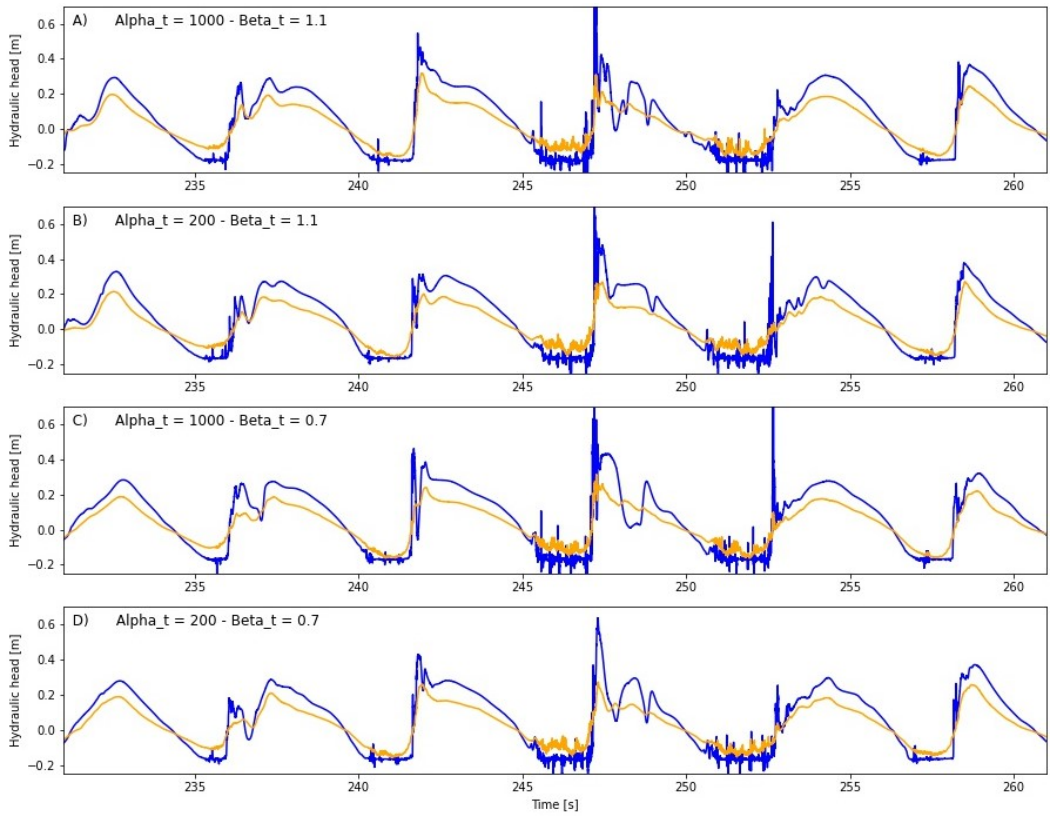

Figure 4.5: Computed pressure distribution on the top layer (blue) and in the filter layer (yellow) in four different simulations are depicted. The simulations are performed in order to calibrate α and β of the filter layer. The four different plots are referred to as figure A-D from top to bottom. A similar pressure signal as shown in figure 4.4 is predicted.

4.3.2. α and β values top layer (schematization 1)

Again, five simulations are performed to determine the α and β values. In this set of simulations, schematization 1 is considered in which the top layer is modelled as a continuum. Simulations A-F in Figure 4.6 only varies in α and β values of the top layer. For the filter layer, the resistance coefficients are set to α=1000 and β=1.1. In figure A, α_{top}=1000 and β_{top}=1.1. These empirical values lead to such a high resistance, that almost no variation in the filter pressure occurs. In simulation B, α has been set to α = 200 (β has not changed) as proposed by Losada et al. (2008) for the top layer of a breakwater. This results in small variations in the measured filter pressure, which are still too small to mimic the Delta Flume tests. Figure C shows the results of a simulation in which only β has changed with respect to Figure A. The results are quite similar and the decrease of β from 1.1 to 0.7 has a very limited impact on the measured filter pressure. The resistance coefficients are further decreased in simulations D and

E. In simulation E, α = 0 which means that the flow through the top layer behaves turbulent. β is set to its minimum value (β = 0.36). This resulted in the biggest pressure fluctuations of the 5 performed simulations. However, the amplitudes of the measured pressures are still too small and not in agreement with the trends observed in Figure D.1 from the physical tests. It can be concluded that designing the top layer as a continuum does not result in a realistic representation of the filter pressures in a dike, for the derived properties (grain size and porosity) in Section 4.2.3. The flow velocities of the porous media flow are significantly smaller than the free flow between the blocks in schematization 2. The typical duration of wave impact is in the order of magnitude $10^{-2} - 10^{-1}$ seconds (Klein Breteler et al., 2012). When the flow velocities through the top layer are too small, no significant increase in filter pressure will occur. In a similar way, there will be a minor decrease in pressure during wave run-down. This principle seems to be the case for the model in which the top layer is modelled as a continuum. It should be noted that the fictional grain size and porosity of the top layer were not adjusted during the simulations. Another method (such as the one described in Appendix D) for determining n and d_{n50} could lead to different results. However, based on the performed simulations preference is given to model the top layer by the schematization of individual blocks, separated by small gaps (schematization 2).

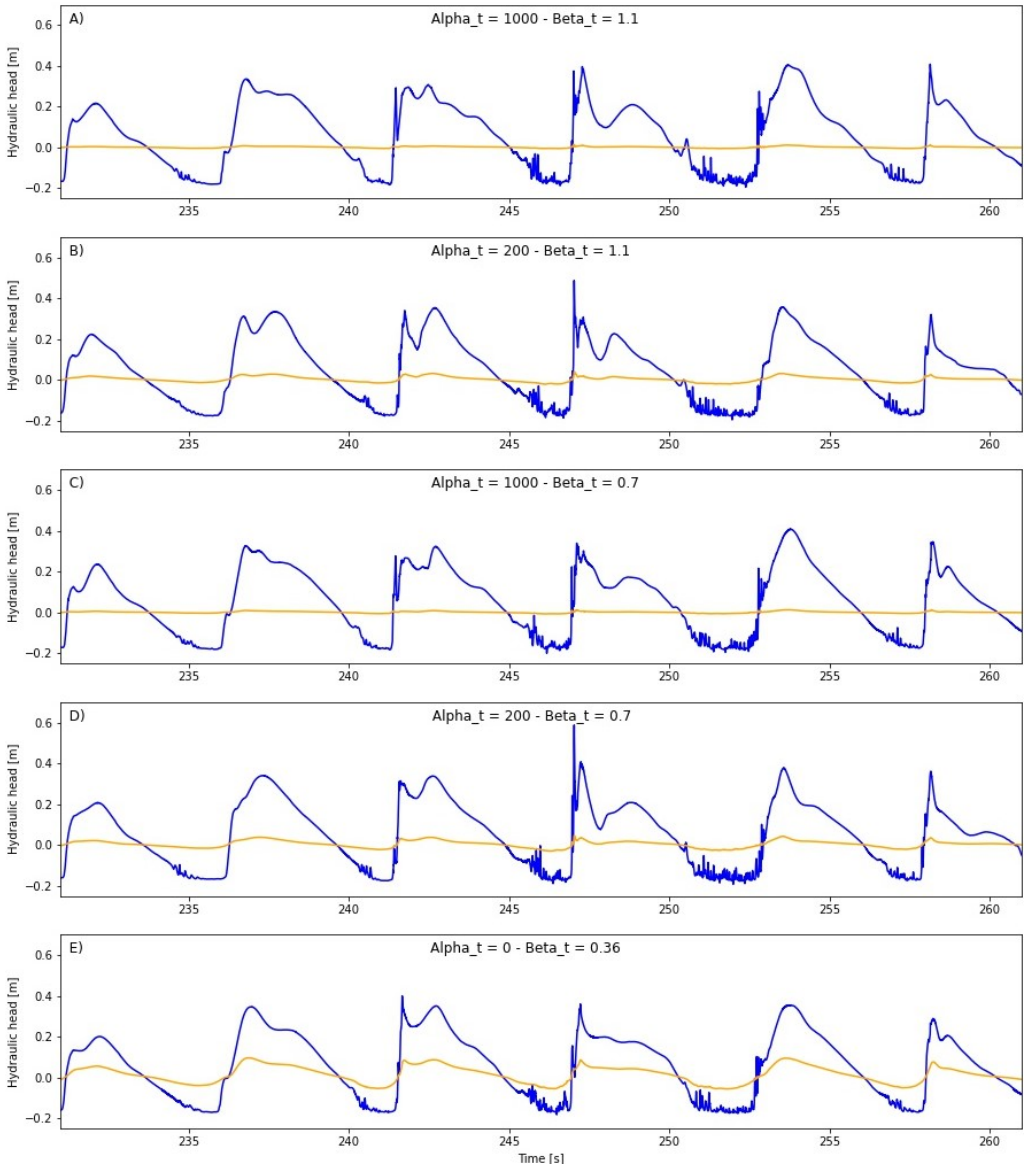

Figure 4.6: Pressure distribution on the top layer (blue) and in the filter layer (yellow) in 5 different simulations are depicted. The simulations are performed in order to calibrate α and β of the filter layer. The 5 different plots are referred to as figure A-E.

4.4. Overview of settings

This section gives an overview of all the settings that have been discussed. After performing two sets of simulations, schematization 2 turns out to be the most promising alternative to model wave loads on a placed block revetment. In the filter layer, the default settings for the resistance coefficients of α=1000 and β=1.1 seems to be valid in this case study. The dimensions and applied properties in the CFD model are listed in the tables on the next page.

	distance [m]
Length	249.79
Height	11.5
L_R	43

Table 4.2: Flume dimensions

Mesh region	**Grid size Δx*Δy [m x m]**
Background mesh	0.4 x 0.4
Mesh near the water surface	0.1 x 0.1
Mesh around top and filter layer	0.003 x 0.003

Table 4.3: Mesh resolution

	Top layer
Thickness [m]	0.175
Number of blocks [-]	35
Block width [m]	0.194
Gap width [m]	0.019
Openness [%]	0.10

Table 4.4: Top layer

	Filter layer
Thickness [m]	0.15
Porosity [-]	0.45
$\mathbf{D_{n50}[m]}$	0.03
$\boldsymbol{\alpha}$**[-]**	1000
$\boldsymbol{\beta}$**[-]**	1.1
KC [-]	10.000

Table 4.5: Filter layer

Variable	**Unit**	**Test 1**	**Test 2**	**Test 3**	**Test 4**	**Test 5**	**Test 6**
h	m	5.20	5.85	5.72	5.59	5.45	5.32
H_{m0i}	m	0.85	0.73	0.73	0.74	0.73	0.74
T_{pi}	s	5.14	4.96	4.96	4.96	4.96	4.87
m_{0i}	m^2	0.045	0.034	0.034	0.034	0.034	0.034
T_{m01i}	s	4.45	4.25	4.25	4.25	4.25	4.22
T_{m02i}	s	4.24	4.09	4.08	4.09	4.08	4.05
$T_{m-1,0i}$	s	4.83	4.54	4.55	4.56	4.56	4.55

Table 4.6: Target hydraulic conditions.

4.5. Conclusion

In this chapter, settings are derived for a CFD model in order to mimic the physical experiment described in Chapter 3. Two different schematizations of the top layer (Figure 4.2) are proposed to model the C-star block revetment. Simulation results for both schematizations are qualitatively analysed. In both cases, the predicted pressure signal on the top layer corresponds to the measured pressure signal in the Delta Flume. However, the filter pressures predicted by the numerical model exhibit different behaviour for schematization 1 and 2. Only the predicted filter pressures in the model with schematization 2 match the results from the physical tests. Therefore, it is decided to focus on schematization 2 in the letter of the research based on the observed filter pressures in both simulations. In the subsequent chapter, quantitative analyses will be conducted in order to evaluate the model's performance.

5

Interpretation and analysis of results

In this chapter, the model performance is tested using simulations and comparisons with the physical tests described in Chapter 3. Section 5.1 describes what should be analysed in the performed simulations. Section 5.2 and 5.3 show the wave statistics and wave impacts on the top layer respectively for 6 performed simulations. These simulations correspond to the 6 different Delta Flume tests. Section 5.4 shows the difference in the hydraulic head for one of the simulations. The next section reviews the influence of the leakage length on the pressure difference over the top layer in a qualitative way since this parameter is considered an important quantity of the structure. In the final section, a scaling analysis was conducted for both design 1 and design 2. The purpose of these analyses was to gain insight into the most important terms of the momentum balance that should be incorporated into a CFD model and to identify potential improvement areas for both designs.

5.1. Approach

To model the hydraulic loads on a placed block revetment, a numerical model should be capable of modelling several processes. From the inlet boundary until the outlet boundary, the following processes should be modelled correctly:

- Wave generation and propagation
- Wave breaking
- Porous media flow

First of all, the model should be able to generate waves that propagate to the structure without (significant) artificial energy dissipation. The wave propagation is analysed by looking into the wave statistics, to check whether the waves are statistically in agreement with the waves in the physical tests. Secondly, the process of wave breaking becomes relevant. This process determines both the magnitude and the location of the wave impact. The available data is insufficient to compare the wave-breaking process between numerical and physical setups. However, by looking at the wave impacts on the structure's top layer, an indication of the course of the process can be given. The last crucial process to model is the flow through the structure. This flow affects the relation between the internal and external pressure during a wave cycle, which can lead to uplifting forces on the placed block revetment. Analysing the pressure difference over the top layer should indicate whether these internal flows are modelled correctly.

5.2. Wave statistics

Figure 3.4 shows the variance density spectra for 6 different hydraulic conditions that are tested in the Delta Flume. Further specifications of the conditions are listed in Table 3.1. In this thesis, it is chosen to expose the structure in the numerical wave flume to statistically the same wave conditions (i.e. a wave signal described by the same variance density spectrum) instead of exactly the same wave signal. The signal of the wave paddle was not available which makes it very hard to mimic the exact wave signal.

However, subjecting the structure to a wave signal with an identical variance density spectrum should result in similar loads on the revetment. Figure 5.1 show the wave spectra of the physical tests (blue) and the spectra of the OpenFOAM simulations (red) in the same figure. It can be seen that the waves from the physical and numerical simulations are in agreement with each other. All the spectra in the figure are based on incoming waves. The incoming waves are separated from the measured wave height by the method proposed by Mansard and Funke (1980). In order to perform this method, the wave gauges at $X = 40.5m$, $X = 43.4m$, $X = 49.5m$ and $X = 61.5m$ are used (in both physical and numerical setups). These wave gauges are the first 4 sensors in line and are located at approximately $1/3$ of the distance from the wave paddle to the structure (see Figure 4.1). To check whether the wave propagation is reproduced correctly, the development of H_{m0} and T_{m01} over the distance from the left boundary to the structure is analysed. No significant changes in the quantities are observed. The corresponding figures are attached in Appendix F. It can be concluded that no significant decrease in energy occurs during the propagation of the waves and that this process is modelled correctly.

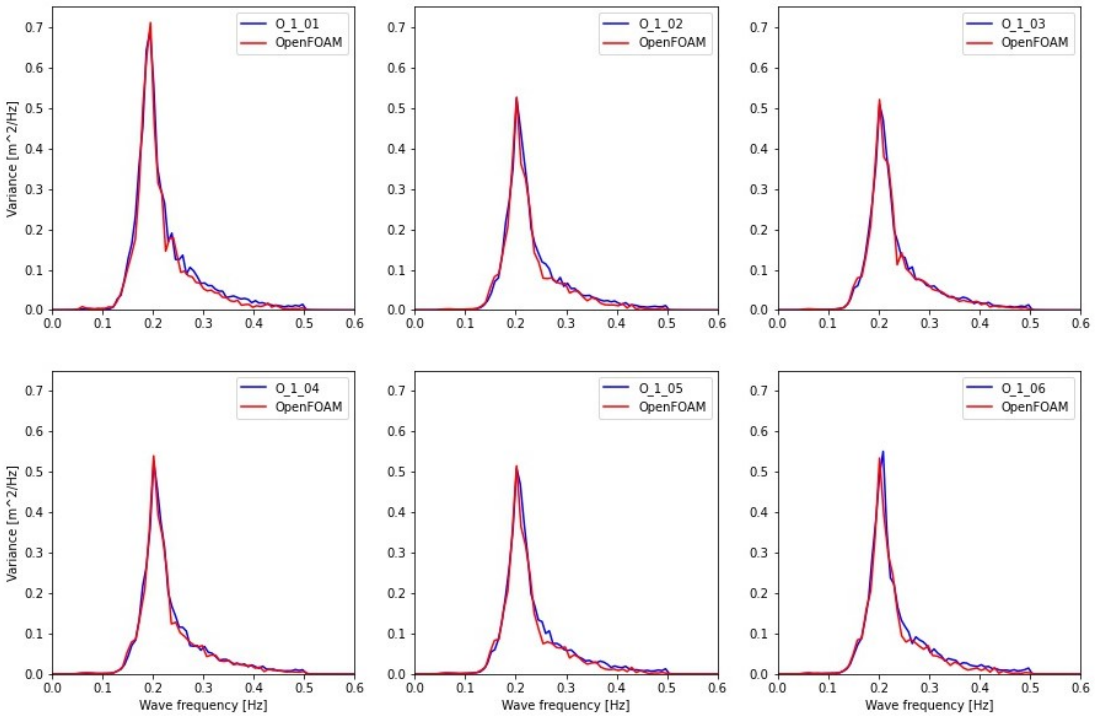

Figure 5.1: Variance density spectra of Delta Flume tests (blue) and OpenFOAM simulations (red). The spectra are subtracted from wave height data obtained from wave gauges at $X = 40.5m$, $X = 43.4m$, $X = 49.5m$ and $X = 61.5m$.

5.3. Wave impact

The wave impact on the top layer is analysed for the same simulations that are used in the previous section. In these simulations, a simple concrete structure without placed block revetment is modelled. There is no requirement to model flows through the structure as the only process being analysed is wave impact (assuming that the flow inside the structure has a minor influence on the wave impact.) As a result, a coarser mesh than the one described in Subsection 4.2.4 will suffice for the simulation outcomes, due to the absence of blocks and the gaps between them. A grid refinement equal to the one that is needed to model the wave propagation is applied on top of the slope of the dike in order to reduce the computation time. To validate the simulated wave impact, the measurements from the physical tests are used (Figure 3.5). However, the number of probes in the Delta Flume was limited. In the numerical simulations, the pressures are measured over a wider range to better understand the pressure distribution over the slope. This section describes the observations per simulation. At the end of the section, it will be concluded how the model performance compares to the physical tests in general. Figure 5.2 gives an illustration of the wave-structure interaction in a CFD model, which leads to the pressures that are used in this section.

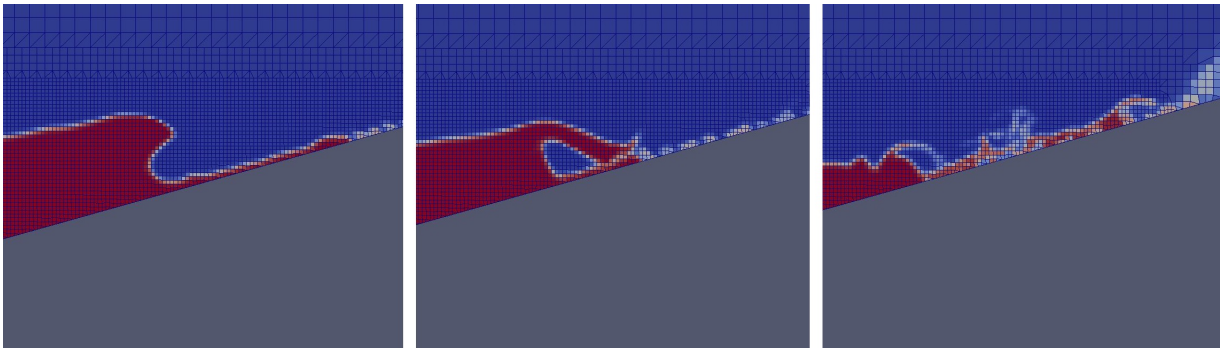

Figure 5.2: From left to right, the wave run-down, wave impact and wave run-up are depicted for wave-structure interaction in the numerical model.

5.3.1. Observations

Simulation 1

Figure 5.3 shows the 2%, 10% and 33% exceedance values for the hydraulic head, for all the pressure transducers in both the physical and numerical simulations. The water level in this simulation is $h = 5.2m$ and the significant wave height $H_{m0} = 0.847m$. As a consequence, the measurements from the physical tests are within the wave impact zone. The results from the numerical and physical tests clearly do not agree with each other. In the numerical experiment, the highest peak values are found at Y = 4.91m (i.e. a depth of 0.31m). Observations have shown that the majority of the waves hit the slope at this location after breaking. Also from a theoretical point of view, the highest pressures are expected after wave breaking. The 2% exceedance value of the hydraulic head at this location is $1.79m$. This is 19% lower than the peak from the physical tests (ϕ = 2.21m), which is found at Y = 4.46m (a depth of 0.74m).

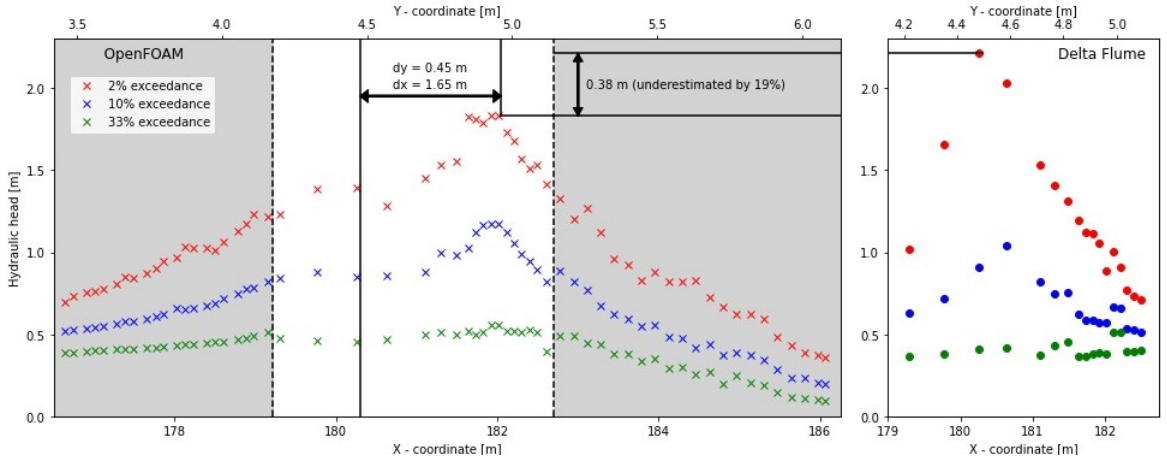

Figure 5.3: Pressure on top layer physical test 1 vs. OpenFOAM simulation. In both tests the following conditions are applied: $h = 5.20m$, $H_s = 0.85m$, $T_{m-1,0} = 4.83s$.

Simulation 2

The water level in simulation 2 is $h = 5.85m$ and the significant wave height is equal to $H_{m0} = 0.746m$. The graph corresponding to the physical test doesn't show a peak within the domain covered by measuring devices, implying that the area of most frequent impact is above this covered domain. From $X = 179m$ to $X = 181m$, the pressures are slightly increasing, while thereafter the measured pressures increase rapidly. The slowly increasing pressures could be explained by the increasing wave height with a decreasing depth, while the rapid increase in pressures suggests the impact of breaking waves. The numerical and physical tests show similar results for the area between $X = 179m$ to $X = 181m$. The 2% exceedance values in this region are approximately 10% smaller in the numerical tests.

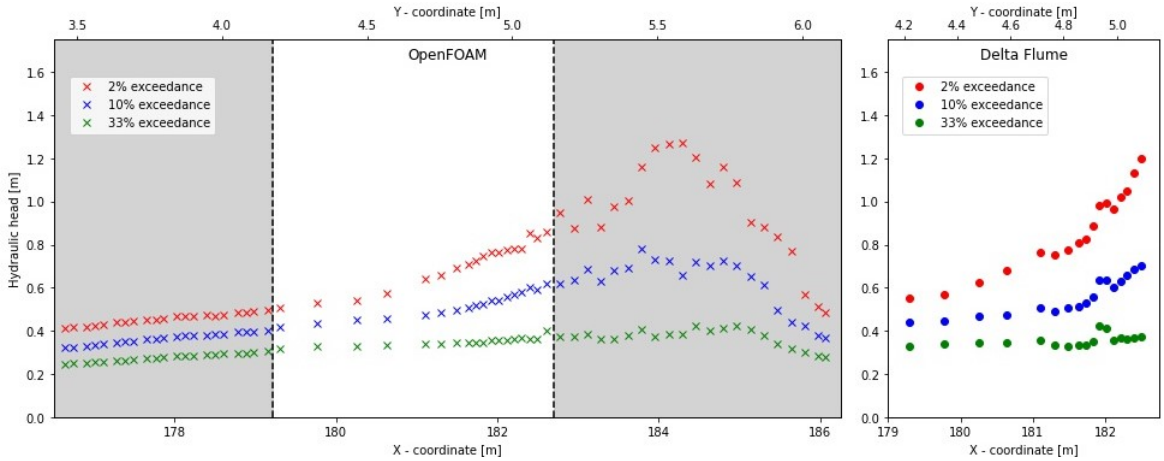

Figure 5.4: Pressure on top layer physical test 2 vs. OpenFOAM simulation. In both tests the following conditions are applied: $h = 5.85m$, $H_s = 0.73m$, $T_{m-1,0} = 4.54s$.

Simulation 3

The applied wave conditions in simulation 3 are quite similar to the conditions in simulation 2. However, the water level is reduced from $h = 5.85m$ to $h = 5.72m$. Lowering the water level causes the waves to break earlier and lower on the slope. The figure corresponding to the numerical simulation shows indeed that the peak shifts slightly to the left compared to Figure 5.4. The results from the physical tests show again an increase in exceedance values for an increasing distance from the wave paddle. The measured values are slightly higher compared to the values from Figure 5.4, which is in line with the decrease in the water depth. The numerical and physical tests show similar results for the area between $X = 179m$ to $X = 181m$.

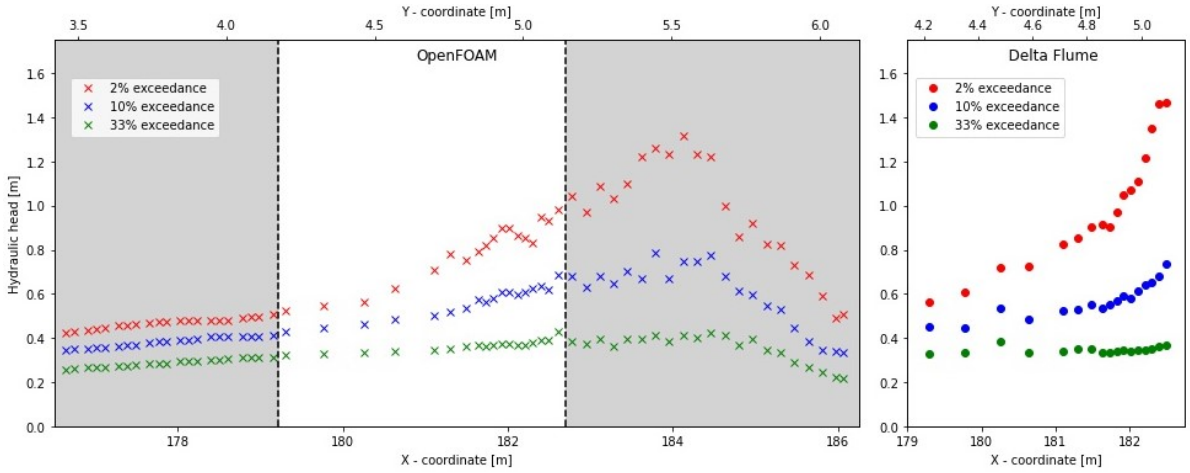

Figure 5.5: Pressure on top layer physical test 3 vs. OpenFOAM simulation. In both tests the following conditions are applied: $h = 5.72m$, $H_s = 0.73m$, $T_{m-1,0} = 4.55s$.

Simulation 4

Again, the hydraulic conditions are kept the same and the water level is decreased by $0.13m$ with respect to simulation 3. The results are in line with simulations 2 and 3. The peak that is visible in the figure, corresponding to the numerical simulations, is a little bit moved to the left while the quantities of the pressures remain the same. From this figure, it is not clear if the maximum exceedance values from the physical tests are within the domain of the measuring devices, or that even higher values would have been found slightly higher on the slope. Therefore, the location of the peaks in the physical and numerical tests cannot be compared.

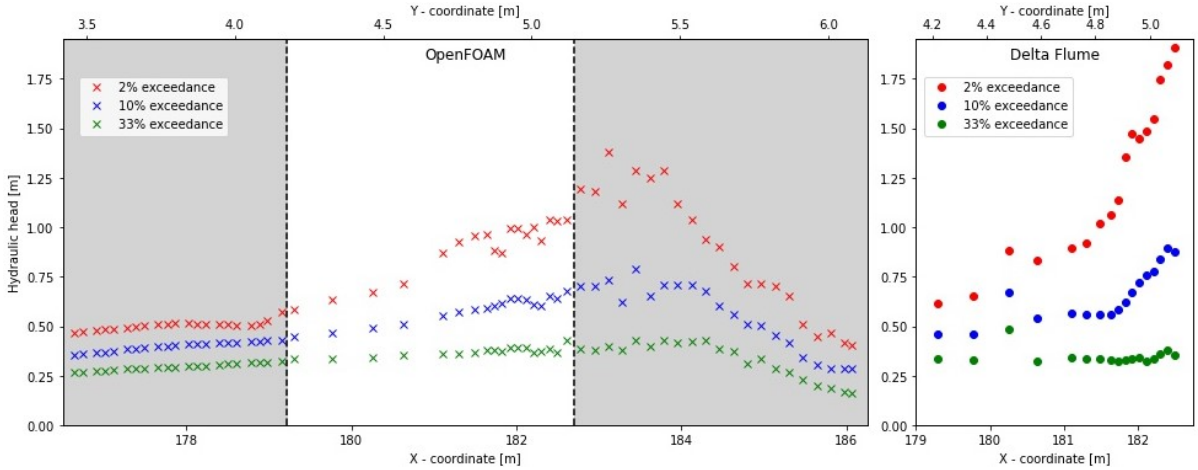

Figure 5.6: Pressure on top layer physical test 4 vs. OpenFOAM simulation. In both tests the following conditions are applied: $h = 5.59m$, $H_s = 0.74m$, $T_{m-1,0} = 4.56s$.

Simulation 5

For the next simulation, the water level is further decreased ($h = 5,45m$). As a result, the wave impacts are within the zone covered by measuring devices for the physical tests. A peak of the 2% exceedance values is found at Y = 182.02 m. The minimum hydraulic head that is measured for the highest 2% of the waves is 2.15 m. In the numerical simulation, the peak of the exceedance values is again moved to the left (compared to the previous simulation) as a result of the decrease in water level. The peak is found at Y = 182.78 m, which is 0.76 m higher than the location of the actual peak as found in the physical test. The minimum hydraulic head that is measured for the highest 2% of the waves in the numerical setup, is 1.38 m. The highest pressures are underestimated by 35.81%.

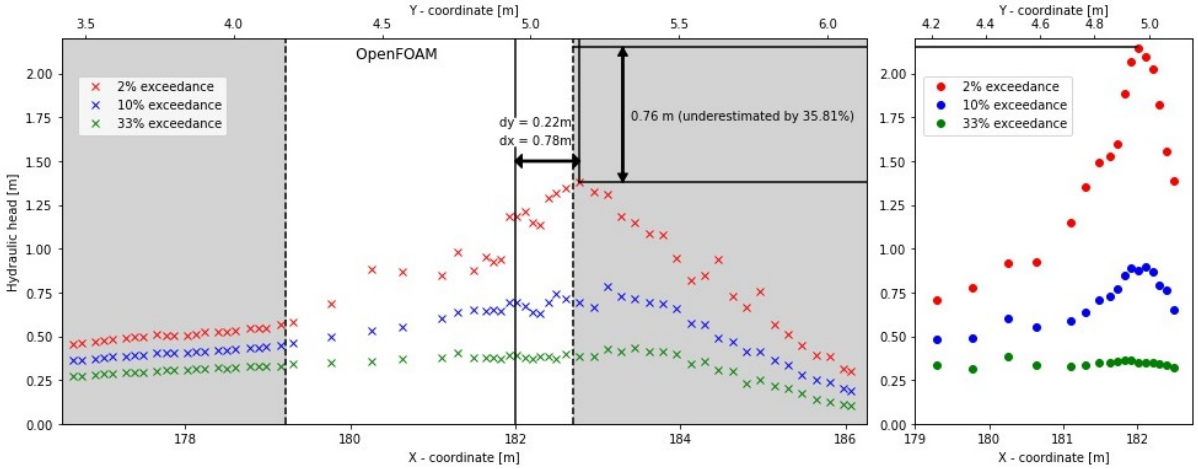

Figure 5.7: Pressure on top layer physical test 5 vs. OpenFOAM simulation. In both tests the following conditions are applied: $h = 5.45m$, $H_s = 0.73m$, $T_{m-1,0} = 4.56s$.

Simulation 6

Also in the last simulation, the water level decreased while the wave conditions remains the same. In the physical test, a peak in 2% exceedance value is found at Y = 4.86 m. In the numerical setup, this peak is found at Y = 4.98 m. The height of the peak in the physical test is 1.92 m and in the numerical simulation 1.42 m. This is an underestimation of 26.04%.

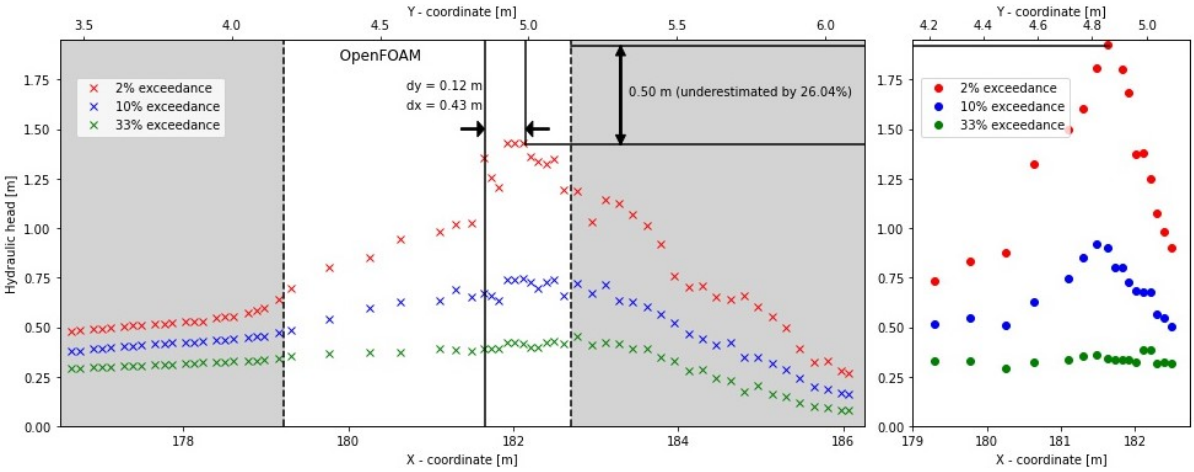

Figure 5.8: Pressure on top layer physical test 6 vs. OpenFOAM simulation. In both tests the following conditions are applied: $h = 5.32m$, $H_s = 0.74m$, $T_{m-1,0} = 4.55s$.

5.3.2. Interpretation

From Figures 5.3-5.8, in which physical tests are compared with numerical simulations, three observations have been made. First of all, the measurements of the hydraulic head show similar results for the numerical and physical tests at the left boundary of the domain, for simulations 2, 3 and 4. For these locations at the left boundary, the ratio (H_{m0}/d) is too high for wave breaking and only quasi-static wave loads are measured. It can be concluded that wave loads on the lower section of the slope can be modelled accurately for the section before the waves' breaking point. The second observation is that the pressures become inaccurate when approaching the location where the waves break. This is visible in simulations 2, 3, 4, 5 and 6. The pressures have been consequently underestimated by the CFD model. The peak in the pressure distribution originates from dynamic wave loads which occur after wave breaking. It can be concluded that the process of wave breaking is not modelled correctly which results in inaccurate pressures on the structure with deviations up to 35%. The last observation is that the predicted location of the peak is consistently too high. This can be seen in simulations 1, 5 and 6. It can be concluded that the wave impact is systematically modelled too high at the slope. The hypothesis is that the numerical model underestimates the wave run-down. As a result, the pressures of the wave load will be underestimated, after the breaking point of the waves and the wave impact will be simulated at a higher location on the slope. The hypothesis is mainly based on the fact that no surface roughness is included in the CFD model which will affect the run-up and run-down. To confirm whether this is true, it is necessary to analyze the data obtained from the physical tests. However, this data is not available.

5.4. Pressure difference

The pressures that occur in the filter layer are highly dependent on the wave loading on the dike. Because of the inaccuracy in predicting the wave-breaking process with the CFD model, also the simulated pressures will deviate from the measured pressures in the Delta Flume. Nevertheless, it is still possible to reflect on the pressure differences that are modelled by the CFD model. A qualitative comparison between the physical and numerical results can provide insight into the model's performance. Test 3, corresponding to Figures 3.5 and 5.5 is further analysed.

Figure 5.9 shows the time series corresponding to pressure sensor V2 & V19 (top) and V17 & V34 (bottom). The considered time series is a random sample consisting of five different waves. On the right side of the figure, the locations of the four sensors are indicated by the dotted line. V2 & V19 are located on the left side of the breaking point and only measure quasi-static wave loads. In Chapter 3 was already concluded that no uplifting forces occur in this region of the slope. The time series show indeed that the pressures on the top and filter layer are approximately the same. The yellow graph is the difference in the hydraulic head (V19-V2) in the upward direction. No significant variation around

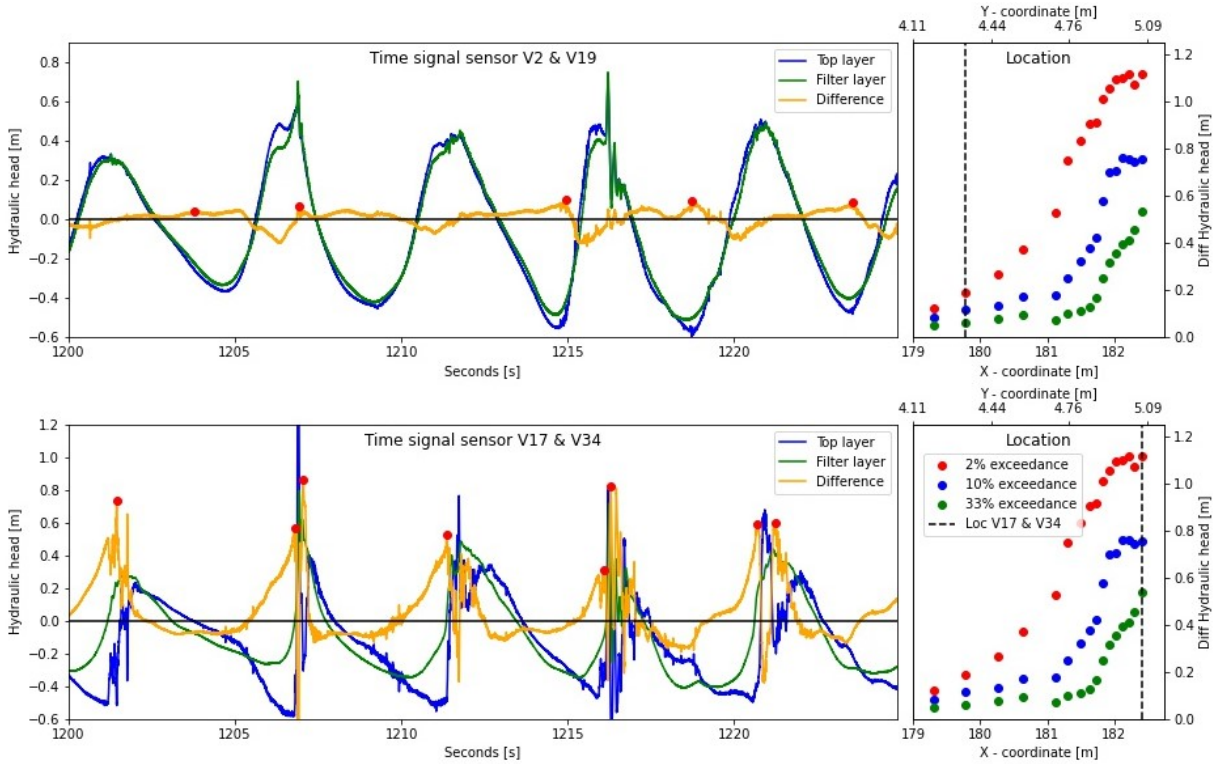

Figure 5.9: Time series that show differences in the hydraulic head for sensor V2 & V19 (top figure) and for sensor V17 & V34 (bottom figure) from **physical test** number 3. The shown time series is a random sample consisting of five waves. On the right side of the figure, the 2%, 10% and 33% exceedance values for the difference in the hydraulic head are plotted for all the sensors. The black dashed lines indicate the locations of sensors V2, V19, V17 and V34. The red markers plotted in the time series indicate the peak values for the difference in hydraulic head.

$\phi = 0$ is visible. V17 & V34 are located on the right side of the domain and are located within the wave impact zone (e.g. will also register dynamic pressures). The measured pressures on the top and filter layer are not identical anymore which results in pressure differences. Before wave impact, the pressures in the filter layer are larger than on the top layer. The mechanism that is responsible for this pressure difference is discussed in subsection 2.2.1.

Figure 5.10 shows a time series from a numerical simulation. The CFD model's applied hydraulic conditions are identical to those in the physical test depicted in Figure 5.9. From Figure 5.10 it becomes clear that no significant pressure differences occur as a result of quasi-static wave loads. The time signal of the hydraulic head in sensors V2 and V19 are identical, which was also found in the physical tests. This is not the case for sensors V17 and V34. As a result of dynamic wave loads, pressure differences are found at the corresponding location at the slope. Again, the upward forces are found just before wave impact, or during wave impact. From a qualitative point of view, the computed pressures in the numerical setup seem to be in agreement with the pressures from the physical tests.

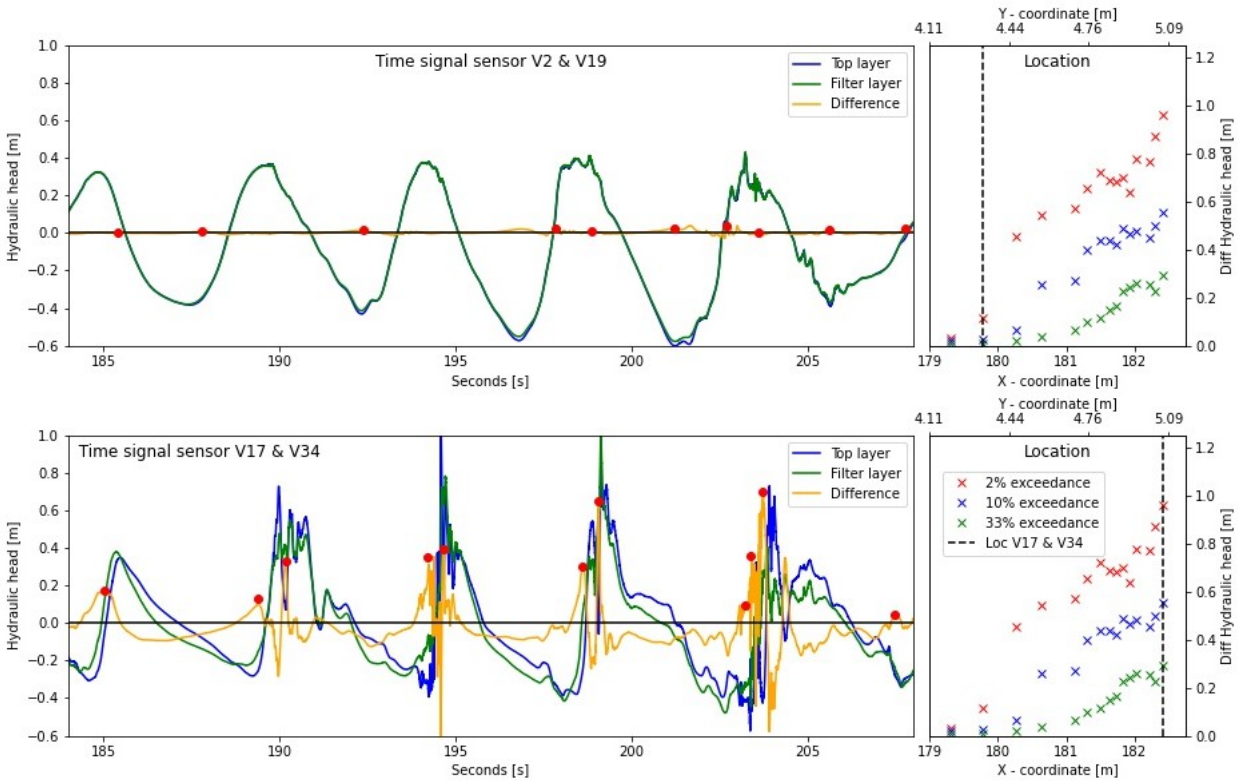

Figure 5.10: Time series that show differences in the hydraulic head for sensor V2 & V19 (top figure) and for sensor V17 & V34 (bottom figure) from **numerical test** 3. The shown time series is a random sample consisting of five waves. On the right side of the figure, the 2%, 10% and 33% exceedance values for the difference in the hydraulic head are plotted for all the sensors. The black dashed lines indicate the locations of sensors V2, V19, V17 and V34.

5.5. Leakage length

In Chapter 2 the importance of the transfer from external to internal loads is discussed, in terms of the stability of a placed block revetment. It was explained how the leakage length characterizes this transfer and concluded that a low leakage length is favourable for a structure. Given the importance of this structure-property, it is important that this property is also reflected within the numerical model. To verify this, multiple simulations are conducted where b, D, k and k' are varied. Modifying these properties causes the structure to deviate from the Delta Flume tests. The simulated pressure differences could not be compared with physical test results. Formula 2.16 gives a relation between the pressure difference and the leakage length. However, this equation can only be solved analytically if boundary conditions are highly schematized and if flow in the filter layer is assumed to be laminar (Schiereck et al., 2019), which is not necessarily the case. The simulations with varied leakage lengths will therefore be qualitatively compared to one another. From formula 2.7 and the described theory in Section 2.3 the following statements became clear:

$$b\uparrow \quad \vee \quad D\uparrow \quad \vee \quad k\uparrow \quad \rightarrow \quad \Lambda\uparrow \quad \rightarrow \quad \Delta\phi\uparrow$$

$$b\downarrow \quad \vee \quad D\downarrow \quad \vee \quad k\downarrow \quad \rightarrow \quad \Lambda\downarrow \quad \rightarrow \quad \Delta\phi\downarrow$$

$$k'\uparrow \quad \rightarrow \quad \Lambda\downarrow \quad \rightarrow \quad \Delta\phi\downarrow$$

$$k'\downarrow \quad \rightarrow \quad \Lambda\uparrow \quad \rightarrow \quad \Delta\phi\uparrow$$

The applied wave boundary conditions are the same as in test 3 (previous subsection). The difference in the hydraulic head is determined by subtracting the measurements from sensors V17 and V34 from

	Plot A	Plot B	Plot C	Plot D
b	↓	-	-	-
D	-	↓	-	-
k'	-	-	↓	-
k	-	-	↓	-
Δϕ	↓	↓	↓	↓

Table 5.1: Expected changes in the difference in hydraulic head for the plotted probability density functions in figure 5.11.

each other. At this location, the highest pressures are measured so potential changes between the measurements from different simulations will be most clearly visible. Figure 5.11A shows a histogram of the measured pressure differences together with their probability density function for $b = b_{ref}$, $b = 0,5b_{ref}$ and $b = 1,5b_{ref}$. Table 5.1 shows how the difference in hydraulic head is expected to change, based on the statements earlier in this section. The reference thickness of the filter layer is the original thickness of $b_{ref} = 0,15m$. In 5.11B, a similar figure is depicted for $D = D_{ref}$, $D = 0,5D_{ref}$ and $D = 1,5D_{ref}$. The reference thickness of the top layer is the original thickness of $D_{ref} = 0,175m$. Figures 5.11C & D show respectively the pressure distributions for variations in n_{filter} and D_{n50}. These properties determine the permeability k of the filter layer. Their reference values are $n_{ref} = 0,45$ and $D_{n50,ref} = 0,03m$. The shown results in the four subplots are based on a series of approximately 100 waves.

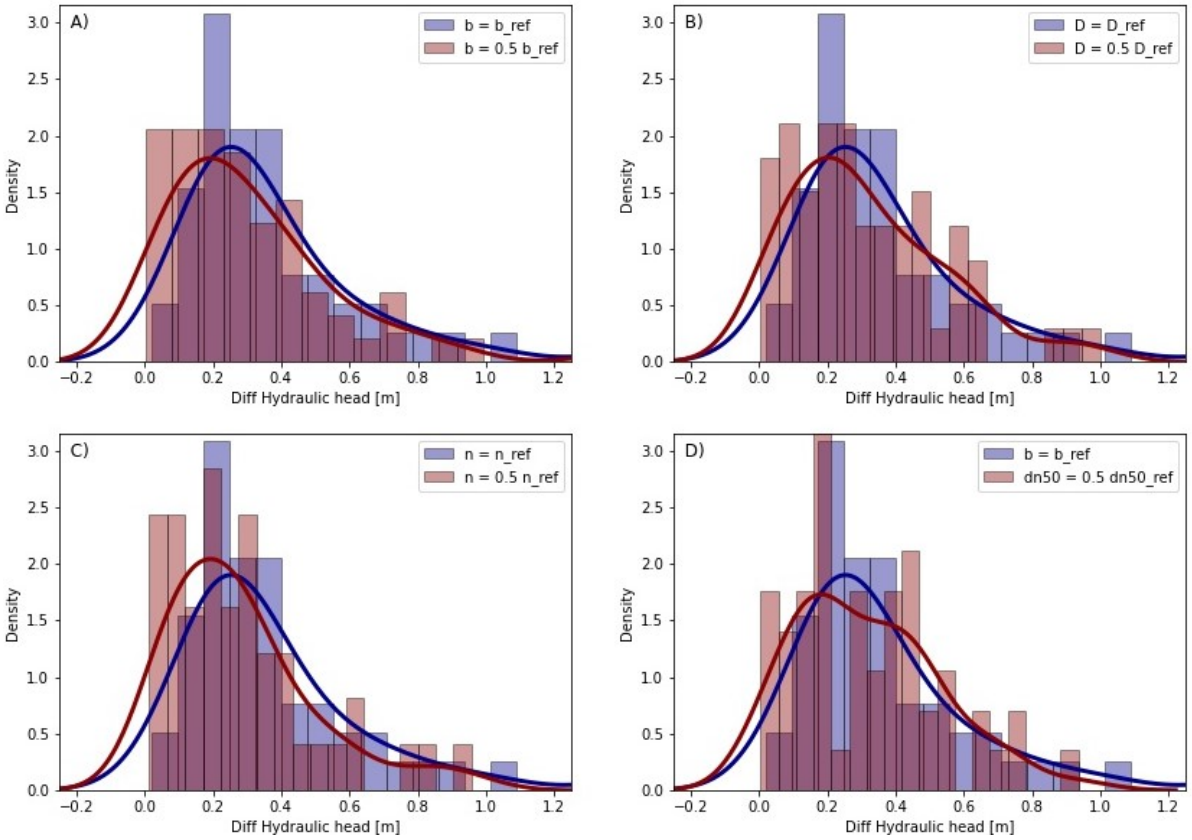

Figure 5.11: Probability density functions for structures with different leakage lengths. The y-axis displays the bin's raw count divided by the total number of counts and the bin width ($density = counts/(sum(counts) * binwidth)$) so that the area under the histogram integrates to 1.

The depicted probability density functions in Figure 5.11A slightly shift to the left direction for a decrease in thickness (b). This is in agreement with the derived statements earlier in this subsection. However, the difference in upward pressure that is calculated for the different structural properties is minimal. It cannot be established from this figure whether the effect of the thickness of the filter layer on the

calculated pressure difference is significant. From Figure 5.11C it becomes clear that the calculated pressure differences decrease for a decrease in the porosity of the filter layer. This result is in agreement with the theory since an increase in porosity leads to an increase in permeability (k). Figure 5.11D aims to depict the impact of the variation in grain size (of the filter layer) on the pressure differences. The distribution of the calculated pressures leads to an unclear probability density function. It is concluded that the model does not show significantly the impact of the leakage length, on the predicted differences in hydraulic head for the performed simulations.

5.6. Analysis of dominant processes

Schematization 2 has been selected as a preference over schematization 1 in Chapter 4. No variations in filter pressures have been calculated for schematization 1, even for the minimum values for the empirical coefficients α and β (see Figure 4.6). By tweaking α and β, only the magnitude of the resistance term in the momentum balance will change. Simply altering the resistance term's magnitude seems insufficient to model the filter pressures, when representing the top layer as a continuum. Simulations with schematization 2 have shown better results when modelling filter pressures and upward pressure differences over the top layer. In order to model flow through the narrow gaps between two adjacent blocks a local mesh size of 0.003 X 0.003 m was required. This has led to an increase in the number of grid cells from approximately 105.544 to 172.408 cells resulting in an increase in computation times as well. There is an exponential relation between the computational cost and the increase in the number of grid cells which is known as the curse of dimensionality (Atanasov & Schnetter, 2017). In general, doubling the number of grid cells in each dimension will lead to an increase in computational time by a factor of 2 to the power of the number of dimensions plus one. The refinement that is necessary to model the flow through the narrow gaps will therefore take 4 times longer than a model in which a continuum top layer (schematization 1) is applied. As a result, the maximum simulation times were limited during this research. To understand why schematization 2 has led to better results than schematization 1, an analysis of dominant processes is performed. The relative importance of different terms of the momentum balance will be discussed in this section and compared for both situations. The momentum balance is repeated once again:

$$\overbrace{(1+C_m)\frac{\partial}{\partial t}\frac{\rho\bar{u}_i}{n}}^{\text{Local inertia}} + \overbrace{\frac{1}{n}\frac{\partial}{\partial x_j}\frac{\rho\bar{u}_i\bar{u}_i}{n}}^{\text{Advective inertia}} = \overbrace{-\frac{\partial\bar{p}^f}{\partial x_i}}^{\text{Grav. forcing}} + \overbrace{g_j x_j\frac{\partial\rho}{\partial x_i}}^{\text{Body force}} + \overbrace{\frac{1}{n}\frac{\partial}{\partial x_j}\mu\left(\frac{\partial\bar{u}_i}{\partial x_j}+\frac{\partial\bar{u}_j}{\partial x_i}\right)}^{\text{Viscous forcing}} \overbrace{+F_p}^{\text{Resistance}} \tag{5.1}$$

Substitution of characteristic length scales in this momentum balance could provide insight into the order of magnitude of the different terms. The obtained equation is stated below:

$$\overbrace{\frac{U}{T}}^{\text{Local inertia}} + \overbrace{\frac{U^2}{L}}^{\text{Advective inertia}} = \overbrace{\frac{gH}{L}}^{\text{Grav. forcing}} + \overbrace{0}^{\text{Body force}} + \overbrace{\upsilon\frac{U}{L^2}}^{\text{Viscous forcing}} \overbrace{+\frac{c_f}{R}U^2}^{\text{Resistance}} \tag{5.2}$$

5.6.1. Schematization 2

First, the flow through the gaps of the top layer in schematization 2 is considered. The relative importance of the different terms of the momentum equation is analysed. The first term of the equation represents the local inertia. For typical flow velocities of 1 m/s and a time scale of 1-3 seconds, the local inertia term will be in the order of magnitude of $O(10^0)$. This order of magnitude for the local inertia is found for both the physical test and the CFD model with schematization 2 or 1. The ratio between the advective inertia term and the viscous forcing determines the flow regime of the water. This ratio is called the Reynolds number and defined as $Re = \frac{uL}{\upsilon}$. During wave run-down, the flow velocity in the middle of the 'pipe' can reach velocities up to 1 m/s as a result of the filter pressures. The length of the pipe is 0,175 m and the kinematic viscosity (υ) is approximately $10^{-6}m^2/s$ for a temperature of 20 degrees Celsius. During this process, the Reynolds number can reach values in the order of magnitude $O(10^5)$ which corresponds to turbulent flow regimes. The last considered term is the resistance term. To estimate the order of magnitude of this term, the value of the friction factor c_f must be determined. For turbulent flows, this factor could be obtained using Moody's diagram, which is a design chart that is based on an empirical equation, called the Colebrook-White formula (Crowe, 2010). In order to use

this diagram, the Reynolds number and the relative pipe roughness (ϵ/d) are needed. The numerical model contains blocks in the top layer without surface roughness e.g. $\epsilon = 0mm$, resulting in a friction factor of $c_f = 0$. In reality, the C-star revetment surface exhibits a certain degree of roughness, and the presence of granular material within the 'pipes' contributes to an increase in resistance. To estimate a more realistic order of magnitude for the resistance term, a surface roughness of $\epsilon = 5mm$ is chosen. This corresponds to coarse concrete according to "Roughness & surface Coefficients" (2003). Using the Moody diagram, a friction factor of $c_f = 0.18$ is found. The resistance term in the applied model is negligible, although a value in the order of magnitude $O(10^0)$ would have been more realistic.

5.6.2. Schematization 1

Next, the ratio of the different terms of the momentum balance will be analysed for schematization 1. Again, the flow through the top layer is considered. The top layer is modelled as a continuum which results in a porous media flow. The resistance term is approximated by the Darcy-Forchheimer equation (2.25) and the Reynolds number for flow through a porous media is defined as $Re_p = (UD_{50})/(n\upsilon)$ (Jensen et al., 2014). The computed velocities within the continuum top layer are in the order of magnitude $U = 0.01m/s$, resulting in $Re_p \sim O(10^3)$. Also in this case a fully turbulent flow regime is found. For a velocity $U = 0.01m/s$ and the empirical values $\alpha = 1000$ and $\beta = 1.1$, the resistance term will be in the order of magnitude $F_p \sim O(10^1)$, which is an order of magnitude too high. For $\alpha = 0$ and $\beta = 0.36$, the resistance term will be in the order of magnitude $F_p \sim O(10^0)$, which is more realistic. In order to improve the ratio between different terms in the momentum balance, the fictional values for the porosity and grain size of the continuum top layer should be changed. Increasing the porosity and grain size will lead to higher velocities resulting in a higher local inertia and advective inertia term. Also, the values a and b will decrease which will affect the resistance term.

Based on the performed analysis of dominant processes, some conclusions can be made. A summation of these conclusions is given below.

- For the process of wave loading on the top layer of the studied placed block revetment, mainly the local inertia, advective inertia and resistance terms are important within the momentum balance.
- The body force term equals zero due to the assumption of incompressible fluids.
- The viscous forcing term is negligible compared to the inertia because of the high flow regimes, during upward pressure differences over the top layer.
- The resistance term is underestimated in the numerical model with top layer schematization 2, due to the absence of shear stress in the 'pipes'.
- The resistance term is overestimated in the numerical model with top layer schematization 1, if $\alpha = 1000$ and $\beta = 1.1$.
- The inertia term is underestimated in the numerical model with top layer schematization 1.
- The numerical model with top layer schematization 1 could be improved by changing the fictional values for the porosity and grain size of the continuum top layer.

5.7. Conclusion

The momentum equation is dominated by local inertia, advective inertia, and resistance. Unlike schematization 1, schematization 2 can model the dominant processes, resulting in the best model predictions. The model performance was accessed on three consecutive processes. The wave generation and propagation predicted by the model were highly accurate. As waves approach the slope, pressures on the top layer increase. The predicted pressures from non-breaking waves, i.e., quasi-static wave loads, differed by less than 10% from the measurements in the physical tests. For dynamic wave loads, the predicted values could deviate by up to 35%. The model predicted the location of wave impact slightly higher on the slope than the actual location. The hypothesis is that small deviations in the run-up and run-down due to the absence of surface roughness have led to the deviation in the location of impact. The last analyzed process is the porous media flow that causes pressure differences. The model

showed only differences in hydraulic head for dynamic wave loads, similar to the physical tests, with deviations of less than 20%. In conclusion, the model is capable of predicting wave loads on placed block revetments. The model will mostly be of qualitative value, due to the deviations in the predictions compared to the physical test results.

6

Discussion

The discussion of this research is divided into three sections. The first section elaborates on the validity of the results. Next, the interpretation of the results is discussed. Justifications for the model outcomes are provided alongside the connection of the results with the underlying theory. The last section describes the limitations of the performed research.

6.1. Validity of results

Delta Flume tests are used to validate the numerical model results in this thesis. These physical tests are discussed in Chapter 3. The exact wave signal that is measured in the Delta Flume is not reconstructed in the numerical setup. The wave paddle signal was not available, making it difficult to mimic the exact wave signal. Instead, a wave signal is applied with the same variance density spectrum based on the incoming wave heights. As a result, the numerical model is subjected to statistically the same wave conditions as applied in the physical tests. The loads on the structure are validated for multiple series of waves, up to N = 500. This validation method offers the benefits of enabling the comparison of trends and extreme values. In practice, design solutions for dike revetments must take into account extreme loads with a low return period, making this validation method an efficient approach.

For the validation of the numerical model, six different physical tests are used. Tests 2-6 had the same wave height and wave period but varied in water level, while test 1 had different quantities for both wave height and wave period compared to tests 2-6. As a result, different wave loads are measured on the revetment. However, all the conducted tests are performed with a wave steepness of 2%. Also, the structure dimensions in the model did not change which means that the same slope is applied in all the tests. In Subsection 2.2 is explained that the breaker type of the waves is fully dependent on the wave steepness and the slope of the structure. For the applied wave steepness of 2% and the slope of the dike, an Iribarren number of $\xi = 2$ is found, which implies plunging breakers. This means that the used numerical model is only validated for plunging breakers with an Iribarren number of $\xi = 2$. For other breaker types, a new validation should be performed. However, this research focuses on the most critical situation in terms of structural design, which is when the revetment is subjected to plunging breakers since these waves generate the highest impact.

6.2. Interpretation of results

6.2.1. Model performance

The goal of the numerical model is the prediction of wave loads on a placed block revetment in order to contribute to the design process of the structure. It is important to reflect on how the CFD model predicts extreme wave conditions (e.g. conditions with a low return period) since the critical loads determine the dimensions of a design. In Subsection 2.1 is explained that the most important failure mechanism of a placed block revetment is the uplift of the top layer. This mechanism can occur due to pressure differences over the top layer that arise during wave run-down and wave impact. The CFD

model should therefore be able to model the pressures in the filter layer and on the top layer correctly. To evaluate the numerical model's ability to predict this load, three consecutive processes are distinguished and assessed on their individual performance. These processes are the wave generation and propagation, wave breaking and internal flow.

The wave generation is assessed by comparing the variance density spectra of the incoming wave heights for the physical and numerical models. Figure 5.1 shows that the spectra from the physical and numerical test are in agreement while also the wave height and wave period remain constant along the numerical flume (see Appendix F). There can be concluded that the wave generation and propagation are very accurately computed by the CFD model.

The process of wave breaking is important for the generated wave loads. From the physical tests, the only data that is closely related to the breaking processes, are the measured pressures on the top layer. Therefore, a comparison is made between the pressure distribution on the top layers of the physical and numerical models. The results have shown that the dynamic pressures predicted by the numerical model are in agreement with the measured values in the physical setup. For the wave impact within the wave-breaking zone, the difference in the results became larger, especially for the extreme values. The maximum 2% exceedance value for the hydraulic head along the slope shows underestimations ranging from 25%-35%, whereas the deviation for 33% exceedance values is less than 10%. The CFD model is observed to have the highest deviations in the predicted pressures for extreme events. The predicted wave impact for highly breaking waves seems to be sensitive to the applied grid resolution in the CFD model although the wave propagation remains stable for the applied range of resolutions. Also, the location of the highest measured pressures slightly differs for the physical tests. In the numerical tests, this impact location is found a distance of $\Delta y = 0.2m$ higher on the slope. In the physical setup, the roughness of the surface is larger than in the CFD model. As a result, the run-up and run-down are different as well, leading to a small deviation in the impact location. Although the CFD model shows acceptable results for the wave impact for the majority of the waves, the extreme events are not well-reflected. Unfortunately, these critical loads are most important when the model has the purpose to accommodate the design of a placed block revetment.

During wave loading, the porous flow determines the filter pressures that occur, which directly lead to the upward pressure differences. The flow through the top and filter layers is highly dependent on the wave impact. Section 5.4 primarily provides a qualitative analysis of the pressure differences. In this section, it is already concluded that pressure differences are only found as a result of dynamic wave loads (e.g. no pressure differences for quasi-static wave loads.) Also, the moments within the wave cycle that shows the largest pressure differences are in agreement with the theory and the physical tests. The model accurately captures the porous media flow and successfully predicts pressure differences over the top layer. Figures 5.9 and 5.10 show an underestimation of approximately 20% in the pressure differences. To enhance the model's prediction of the pressure differences, it will be most effective to improve the wave run-down mechanism within the model. Further evaluation of the flow through the structure will be conducted using scaling analysis.

6.2.2. Leakage length

In Section 5.5, the influence of the leakage length is investigated. The leakage length of the structure is changed by decreasing the top layer thickness, filter layer thickness, the porosity of the filter and the grain size of the filter. For the performed simulations, histograms are plotted together with their probability density function for the difference in hydraulic head to see the impact of the changed dimensions of the structure. Again, the findings presented here are based on qualitative observations, as no physical test results are available to validate the simulation. The main objective is to demonstrate how the CFD model responds to changes in the leakage length of the structure. In all cases, the probability functions move to the left (e.g. smaller differences in hydraulic head) for a decrease in leakage length which is in line with the literature. Nevertheless, the differences between the simulations in Figures 5.11B and 5.11D are not that clear, and it is worth noting that each simulation is limited to 100 waves. This might not be enough for statistical analysis, especially when looking at extreme values. It was not feasible to extend the duration of the simulations because of the long computational times. It is concluded that the results show a minor influence of the leakage length on the differences in hydraulic

head.

6.2.3. Analysis of dominant processes

To better understand the differences between the model results of schematization 1 and schematization 2, an analysis of dominant processes is performed in Section 5.6. It has been analysed which terms of the momentum balance are dominant when the placed block revetment is subject to an uplifting force. For a first estimate, it is sufficient to only consider the local inertia, advective inertia and resistance term. For schematization 2, there is almost no resistance included in the flow through the top layer. Boundary conditions within the gaps which cause more friction would have led to higher uplifting forces. A resistance term in the order of magnitude of $O(10^{-1})$ would have been more realistic. In Section 5.5, which is discussed in the previous subsection, the leakage length of the structure is mainly changed by decreasing the permeability of the filter layer. It would have been interesting to also change the permeability of the top layer by applying different boundary conditions (surface roughness within the gaps). Nevertheless, it should be noted that in practical applications, the resistance term is small compared to the local inertia and advective inertia terms. Therefore, schematization 2 remains capable of producing satisfactory outcomes. This is not the case for schematization 1. No pressure variations in the measured filter pressures are found. Analysis of the dominant processes has shown that the relative importance of the inertia term is underestimated while the predicted resistance is too large. The model performance could be improved by choosing other dimensions for the fictional grain size and porosity of the top layer of the structure. Another method has to be derived for choosing these variables.

6.3. Limitations

During the course of this research, several limiting factors were encountered. The majority of these limitations stem from the conversion of physical experiments to numerical simulations, resulting in discretization-related constraints. Additionally, the limited amount of available data from physical tests was a restriction for the validation. The most important limitations are further elaborated.

Availability of data

A big advantage of numerical modelling is the unlimited amount of data that can be generated if computation efficiency is not taken into account. Pressures and velocities are measured through the entire domain to determine the most critical location of the placed block revetment in an efficient way. For physical setups, the amount of measuring devices is restricted. The best locations to measure data are determined before the research. The Delta Flume tests employed in this thesis were originally designed for a different purpose than to serve as validation of a CFD model. As a result, the locations of the measuring devices in the Delta Flume were not optimal for this research. Also, different combinations of water levels and wave conditions could provide this research with more data to use for validation. The limited amount of data from the physical test is considered a limitation of the research. However, the large amount of data that could be obtained from the CFD model makes it an extremely useful tool. It is possible to create a detailed overview of how the loads are divided over the structure for example.

Schematization to a two-dimensional model

The applied CFD model is a 2DV OpenFOAM model. By schematizing the situation to a two-dimensional case, the structure is assumed to be uniform in depth (e.g. only one cross-section is considered.) The top layer of the structure in the Delta Flume consists of a C-star block revetment. An illustration of the revetment can be found in Appendix E. The dimensions of the C-star blocks are clearly not uniform with depth. The complex design has to be translated into simple two-dimensional dimensions with the same characteristics. Throughout this thesis, the C-star revetment was represented in a simplified form using rectangular blocks with gaps of approximately the same size as the spacing between blocks in practice. While this was done for the sake of simplicity, there is room for further improvement in the model. Exploring two-dimensional designs that more closely mimic the physical process in numerical simulations may yield this improvement.

Predicted pressures dependent on grid resolution

In Chapter 4, a computational grid is defined that yields stable results. To accurately model the wave propagation, a local grid refinement was necessary. The mesh near the water surface has a grid size of 0.1 x 0.1 m. To model a flow through the gaps in the top layer, a minimum grid size of 0.003 x 0.003 m was necessary to obtain stable and accurate results. However, simulations (that not have been shown in earlier chapters) have shown a dependency between the predicted pressures and the applied grid resolution even though the wave propagation remains accurate for different grid sizes smaller than 0.1 x 0.1 m. In Figure 6.1, the wave impact on the top layer is depicted. The top figure was already shown in Section 5.3 (test 6). The mesh around the structure has a size of 0.1 x 0.1 m. In the bottom figure, the mesh is refined and has a size of 0.006 x 0.006 m at the location of wave impact. On the right side of the figure, the grids are shown for both situations. A significant increase in the measured values can be found. Further investigation is required to establish a technique for determining the optimal grid resolution leading to accurate results.

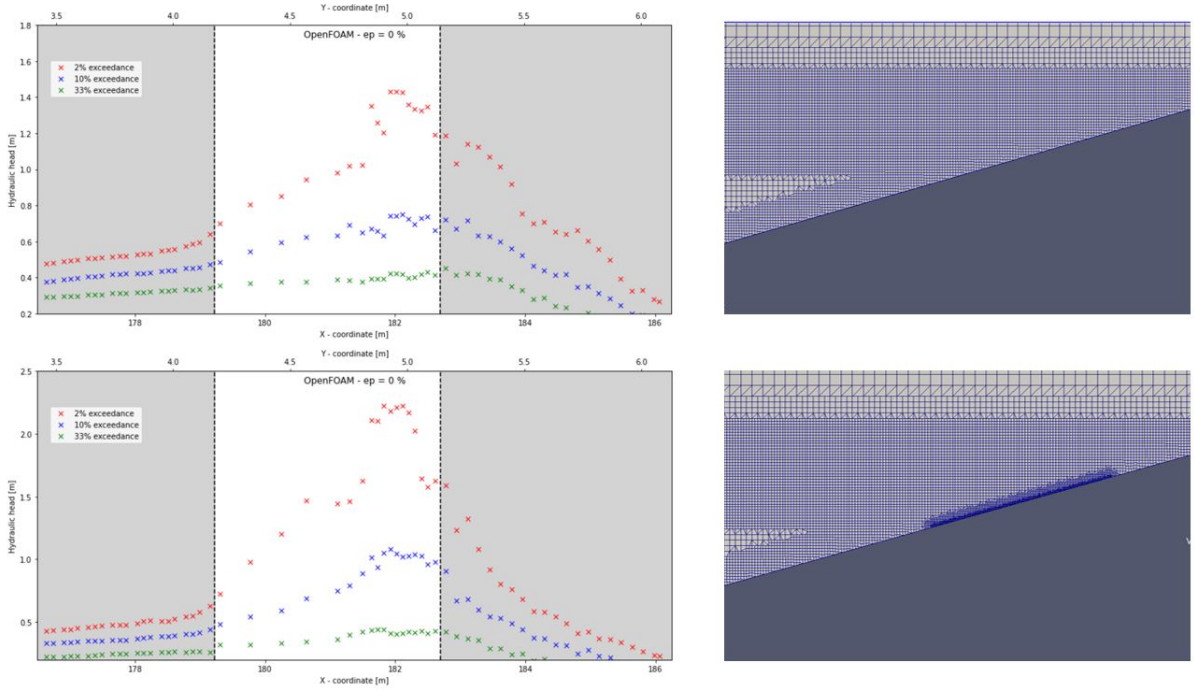

Figure 6.1: Pressure on top layer, for two different local grid sizes. The local mesh at the wave impact zone is 0.1 x 0.1 m in the top figure and 0.006 x 0.006 m in the bottom figure. On the lift side of the figure, the pressure distributions are shown while on the right side of the figure the different grids are depicted.

Computational times

In order to validate the CFD model, it utilizes the same wave conditions as measured in the Delta Flume. For this statistical approach, approximately 500 waves per simulation were needed. As a result, simulation times up to 2000 seconds are applied. In addition, mesh refinements were needed to model the flow through the gaps in the top layer of the structure. The local mesh size of 0.003 x 0.003 m leads to a total of 172.408 grid cells. Due to the extensive number of grid cells and a simulation time of 2000 seconds, the total run-time of the CFD model is approximately 15 days. This duration posed a constraint on the research, as it restricted the number of simulations that has been executed.

7

Conclusions and recommendations

7.1. Conclusions

The purpose of this research was to determine whether CFD modelling can accurately model hydraulic loads on placed block revetments as a result of wave impact. The model performance is evaluated using physical tests conducted in the Delta Flume from Deltares. In this chapter, the main research question is addressed, and the key conclusions derived from the sub-research questions are presented. The first subsection provides answers to each sub-research question, and the following subsection draws a conclusion that addresses the main research question. Finally, recommendations are provided in the last subsection.

7.1.1. Answer to sub-research questions

Sub-question 1: What are the physical mechanisms that lead to different pressure signals on the top layer and in the filter layer of a placed block revetment?

During wave run-down, water flows from the filter layer to the surface due to hydrostatic pressure. However, the flow along the slope is faster than the flow through the structure. As a result, the hydraulic head in the filter layer is larger than the hydraulic head on the top layer during maximum run-down. This upward pressure difference could lead to uplifting forces. To model these uplifting forces, it is important to include resistance through the structure. Also, the inertia of the water has to be included in the model, as it resists changes in velocity and direction, which contributes to the phase difference between the pressure on the top layer and in the filter layer.

Sub-question 2: How does the pressure distribution on the top layer of a dike predicted by CFD modelling relate to the pressure distribution from a similar setup in a physical test?

The predicted (top layer) pressures could be divided into two sets of measurements: those obtained from devices that capture wave loads prior to wave breaking, and those obtained from devices that measure wave loads subsequent to wave breaking. Prior to wave breaking, only quasi-static wave loads are measured. The predicted pressures as a result of quasi-static wave loads are in agreement with the measurements from the physical tests. The quasi-static pressures in the CFD model exhibit a deviation of less than 10% compared to the devices in the Delta Flume.

After wave breaking, also dynamic wave loads are measured. The dynamic wave loads produce the highest pressures on the slope. However, the pressures originating from dynamic wave loads have higher inaccuracies than the quasi-static wave loads. The 2% exceedance values of the predicted hydraulic head deviate up to 35% from the measurements in the physical tests. The process of wave breaking is not accurately represented in the model, leading to discrepancies in the outcomes. Also, the run-down distance in the model is too small, resulting in peak loads at smaller depths (d). This could

be explained by the difference in surface roughness in the CFD model compared to the physical set-up.

Sub-question 3: How do the filter pressures in a dike determined by CFD modelling relate to the filter pressures determined in physical tests?

During this thesis, two different structure schematizations are created and evaluated on their results. The schematizations only differ on their top layer. In schematization 1, the top layer was modelled as a continuum layer while in schematization 2, the top layer consists of rectangular blocks, alternated by small gaps. It has been demonstrated that the top layer schematization plays a crucial role in the pressure distribution within the filter layer. It has been found that schematization 2 yields the best results. The physical test results described in Chapter 3 show relatively constant hydraulic heads in the filter layer along the slope. This is also found in the results from the CFD model for schematization 2. The filter pressures in the CFD model exhibit a deviation of approximately 10% compared to the devices in the Delta Flume.

Sub-question 4: To what extent is it feasible to model the top layer of a dike as a continuum, and what are the required α and β values for producing accurate estimates of hydraulic loads?

In the answer to sub-question 3 was already mentioned that schematization 2 shows better results for modelling filter pressures. Designing the top layer as a continuum has not resulted in a realistic representation of the filter pressures. In schematization 1, the porous flow through the top layer is relatively small compared to the duration of the wave impact, run-up and run-down. As a result, the pressure in the filter barely increased during wave impact, and neither decreased during wave run-down. The hydraulic head in the filter remains relatively constant over time, and no significant variation could be observed for the applied properties of the structure. The resistance in the filter layer is too high, even for the minimum value of α and β. However, the resistance in the continuum top layer could also be further decreased by changing the fictional grain size and porosity of this layer. These properties are estimated through analysis of their physical significance, and selection of appropriate values based on assumptions and kept constant during this thesis. For the chosen values for n and D_{n50} of the top layer, it is not feasible to model the top layer as a continuum layer, in order to produce accurate estimates of the hydraulic loads on a placed block revetment. It is likely that a significant increase in n and D_{n50} will lead to better results.

Sub-question 5: What would be the added value of CFD modelling in the design process of placed block revetments?

CFD models are able to predict hydraulic loads on structures. For placed block revetments, the dimensions are determined by considering both the magnitude and location of pressures acting on the top layer and filter layer. The numerical model could give an indication of the critical loads, and the location of the impacts. This consideration could be integrated into the design of placed block revetments, in addition to the existing design guidelines. Furthermore, due to the predictive capacity of the CFD model for hydraulic loads on the structure, it has the potential to enhance the efficiency of physical modelling. By conducting CFD simulations prior to physical modelling, valuable insights can be gained into the optimal wave conditions and water levels to apply in physical testing. Additionally, numerical models can identify the most pertinent locations on the structure to place measuring devices. In conclusion, CFD will provide valuable insights when used in a qualitative manner because the physical processes are modelled correctly. However, for extreme wave loads the differences in predicted pressures can deviate up to 35%, which should be taken into account when using CFD for such applications.

7.1.2. Answer to main question

Research question: What is the most effective way to model a placed block revetment using CFD to simulate the hydraulic head over a revetment, which consequently can cause uplift of units in the top layer? Which physical processes should be incorporated into this model?

The most important failure mechanism of a placed block revetment is the uplift of the top layer. The uplifting force results from a difference in hydraulic head over the top layer (e.g. the pressure on the top layer is smaller than the pressure in the filter layer for two locations situated above each other perpendicular to the slope.) This pressure difference originates from wave loading on a dike. During its wave cycle, the wave impact, run-up and run-down induce a pressure signal on the top layer and in the filter layer. These two pressure signals are different because of the flow through the structure. Therefore, the physical processes that need to be modelled correctly in order to model the uplifting force, are the wave propagation through the flume, the wave breaking that leads to wave impact and the flow through the structure.

In this research, the CFD model OpenFOAM is used. This model solves the NS equations to predict the course of the flow. To model the flow between the filter layer and the surface, local inertia, advective inertia and resistance are the dominant terms in the conservation of momentum equation. A two-dimensional model is applied, in order to significantly reduce computational times. Two different schematizations of the top layer are applied to investigate the most favourable method to model a placed block revetment. The first option concerns a computational grid in which a continuum top layer is applied. The porous flow velocities were several orders of magnitude lower than expected, leading to an underestimation of the inertia term in the momentum equation. As a result, the model was not able to generate realistic predictions of the uplifting forces. In the second schematization, the top layer is schematized into rectangular blocks alternated by small gaps to ensure the flow through the top layer. This model has demonstrated the ability to predict uplifting forces that deviated less than 20% from the physical test results.

7.2. Recommendations

Contributions
The CFD model is capable of reproducing wave generation and propagation very accurately. The pressure on the top layer deviates by less than 10% from the physical tests before wave breaking and up to 35% for wave impact resulting from breaking waves. Moreover, the pressure differences over the top layer show a deviation of less than 20%. Despite these deviations, the predicted wave load trends show a high level of similarity to those of the physical experiment. Therefore, it is recommended to use the CFD model qualitatively in the design process of a placed block revetment on a (sea) dike. It should be noted that the CFD model can only simulate loads on a structure and cannot predict the stability of individual blocks. However, it can assist in identifying the blocks most likely to be subjected to extreme loads, and this information can be taken into account in the design process. By conducting CFD simulations before physical tests, the latter can be executed more efficiently, thereby reducing costs and duration. The CFD simulations can for example indicate the most interesting locations to place measuring devices for specific wave conditions and water levels, and show which conditions are most interesting to apply in the physical tests.

Future research
Modelling the wave-breaking process is a crucial step for accurately predicting uplifting forces acting on the top layer. However, the pressures on the top layer obtained from the numerical model are not in agreement with the physical tests, for the wave impact zone. Results have shown that decreasing the grid sizes leads to an increase in predicted pressures. While for wave propagation a maximum grid size can be determined for which a further decrease in grid size does not significantly affect the results, this does not appear to be the case for pressure measurements. Further investigation is required to determine the optimal grid size to predict pressures on a slope. A methodology needs to be developed which is applicable in general cases.

Schematization 2 is the favourable schematization of the top layer since this model is able to predict uplifting forces, unlike schematization 1. The disadvantage of schematization 2, is the required mesh size to model the flow through the gaps in the top layer. To simulate a series of 500 waves with a period of approximately 5 seconds, the computational time required for the model is approximately 15 days. This is considered too long for practical use. Schematization 1 did not require a grid refinement for the top layer which makes the model computationally attractive. The model predictions were not accurate because of the underestimation of the filter velocities leading to an underestimation of the inertia term in the momentum equation. However, during the research, the fictional porosity and grain size of the top layer were kept constant. Changing these properties can result in different velocities through the top layer which may improve the results. In Appendix D is shown that an increase in the fictional grain size can adjust the predicted filter pressures. This simulation implies that it is possible to improve the results of the CFD model with the continuum top layer. Further research has to prove to what extent this model is able to mimic the physical tests.

Bibliography

Atanasov, A., & Schnetter, E. (2017). *Sparse grid discretizations based on a discontinuous galerkin method*.

Battjes, J. (1974). *Computation of set-up, longshore currents, run-up and overtopping due to wind-generated waves* (Doctoral dissertation). http://resolver.tudelft.nl/uuid:e126e043-a858-4e58-b4c7-8a7bc5be1a44

Berberović, E., Van Hinsberg, N., Jakirlić, S., Roisman, I., & Tropea, C. (2009). Drop impact onto a liquid layer of finite thickness: Dynamics of the cavity evolution. *Physical review. E, Statistical, nonlinear, and soft matter physics*, *79*, 036306. https://doi.org/10.1103/PhysRevE.79.036306

Blacka, M., Nilsen, A., & Colleter, G. (2011). An overview of the use of physical models to assess wave loading on marine structures.

Crowe, C. (2010). *Engineering fluid mechanics 9th edition binder ready version with binder ready survey flyer set*. John Wiley & Sons, Incorporated. https://books.google.nl/books?id=g0qiuAAACAAJ

de Waal, J., Klein Breteler, M., & den Adel, H. (1995). *Taludbekleding van gezette steen: Golfdruk op het talud: Deel b: Verbetering van het analytisch model en steenzet, verslag bureaustudie*. Deltares. http://resolver.tudelft.nl/uuid:a659e727-e0f5-4d8f-9385-7a0e94d022e4

Dorst, K., Provoost, Y., & Verhagen, H. Stability of pattern placed revetment elements. In: PIANC, 2012, February. http://resolver.tudelft.nl/uuid:84541e27-6382-4cb2-ae35-c5365aa7be90

Engelund, F. (1954). *On the laminar and turbulent flows of ground water through homogeneous sand.*

Fuhrboter, A., & Sparboom, U. (1988). Full-scale wave attack of uniformly sloping sea dykes. *Coastal Engineering Proceedings*, *1*(21), 161. https://doi.org/10.9753/icce.v21.161

Gamaleldin, M., Babanin, A., & Chabchoub, A. (2020). On cfd numerical wave tank simulations: Static-boundary wave absorption enhancement using a geometrical approach.

Grüne, J. (1989). Wave-induced shock pressures under real sea state conditions, 2340–2354. https://doi.org/10.1061/9780872626874.174

Hanjalic, K. (2004). Closure models for incompressible turbulent flows, 2–4. https://www.researchgate.net/file.PostFileLoader.html?id=53898c5fd039b1bd3a8b45c0&assetKey=AS%5C%3A273543839846420%5C%401442229341759

Higuera, P., Lara, J. L., & Losada, I. J. (2013a). Realistic wave generation and active wave absorption for navier–stokes models: Application to openfoam®. *Coastal Engineering*, *71*, 102–118. https://doi.org/https://doi.org/10.1016/j.coastaleng.2012.07.002

Higuera, P., Lara, J. L., & Losada, I. J. (2013b). Simulating coastal engineering processes with openfoam®. *Coastal Engineering*, *71*, 119–134. https://doi.org/https://doi.org/10.1016/j.coastaleng.2012.06.002

Higuera, P., Lara, J. L., & Losada, I. J. (2014a). Three-dimensional interaction of waves and porous coastal structures using openfoam®. part i: Formulation and validation. *Coastal Engineering*, *83*, 243–258.

Higuera, P., Lara, J. L., & Losada, I. J. (2014b). Three-dimensional interaction of waves and porous coastal structures using openfoam®. part ii: Application. *Coastal Engineering*, *83*, 259–270.

Holmes, L., Favero, J., & Osswald, T. (2012). Numerical simulation of three-dimensional viscoelastic planar contraction flow using the software openfoam. *Computers Chemical Engineering*, *37*, 64–73. https://doi.org/https://doi.org/10.1016/j.compchemeng.2011.09.015

Holthuijsen, L. H. (2007). *Waves in oceanic and coastal waters*. Cambridge university Press.

Howarth, M., Allsop, W., Vann, A., Jones, R., & Davis, J. (1996). Scale effects of wave impact pressures on cob armour units. *Proceedings of the 25th International Conference Coastal Engineering 1996*, *2*, 2522–2531.

Huang, L., Li, Y., Benites-Munoz, D., Windt, C. W., Feichtner, A., Tavakoli, S., Davidson, J., Paredes, R., Quintuna, T., Ransley, E., Colombo, M., Li, M., Cardiff, P., & Tabor, G. (2022). A review on the modelling of wave-structure interactions based on openfoam. *OpenFOAM® Journal*, *2*, 116–142. https://doi.org/10.51560/ofj.v2.65

Jacobsen, Fuhrman, D., & Fredsoe, J. (2012). A wave generation toolbox for the open-source cfd library: Openfoam (r). *International Journal for Numerical Methods in Fluids*, *70*. https://doi.org/10.1002/fld.2726

Jacobsen, van Gent, M. R., & Wolters, G. (2015). Numerical analysis of the interaction of irregular waves with two dimensional permeable coastal structures. *Coastal Engineering*, *102*, 13–29. https://doi.org/https://doi.org/10.1016/j.coastaleng.2015.05.004

Jacobsen, van Gent, M., Capel, A., & Borsboom, M. (2018). Numerical prediction of integrated wave loads on crest walls on top of rubble mound structures. *Coastal Engineering*, *142*, 110–124. https://doi.org/https://doi.org/10.1016/j.coastaleng.2018.10.004

Jensen, B., Jacobsen, N. G., & Christensen, E. D. (2014). Investigations on the porous media equations and resistance coefficients for coastal structures. *Coastal Engineering*, *84*, 56–72. https://doi.org/https://doi.org/10.1016/j.coastaleng.2013.11.004

Jonkman, S., Jorissen, R., Schweckendiek, T., & van den Bos, J. (2021). *Flood defences lecture notes cie5314 4th edition*.

Klein Breteler, M., & Mourik, G. (2020). *Stabiliteit van steenzettingen bij een overgangsconstructie: Deltagootonderzoek voor pov-waddenzeedijken* (tech. rep.). Deltares.

Klein Breteler, M., Mourik, G., & Bosters, M. (2014). *Stabiliteit van steenzetting bij golfaanval: Samenvatting onderzoeksresultaten 2003 - 2013* (tech. rep.). Deltares. http://resolver.tudelft.nl/uuid:f81f904a-8052-418b-926a-c48b4ef881e4

Klein Breteler, M., 't hart, R., Wichman, B., Dorst, C., Provoost, Y., & Bizzarri, A. (2015). *Handreiking dijkbekleding: Deel 2: Steenzettingen* (tech. rep.). Deltares. http://resolver.tudelft.nl/uuid:dcd44389-f276-48ba-a693-29a15c9b3600

Klein Breteler, M., & Van der Werf, I. (2016). *Kennisontwikkeling t.b.v. steentoets2006* (tech. rep.). Deltares. http://resolver.tudelft.nl/uuid:fc5113b4-7cc5-40cd-a4c4-ff0e5b99c3f7

Klein Breteler, M., Van der Werf, I., & Wenneker, I. (2012). *Kwantificering golfbelasting en invloed van lange golven: Onderzoeksprogramma kennisleemtes steenbekleding* (tech. rep.). Deltares. https://edepot.wur.nl/241149?_ga=2.101955201.1255012660.1655232552-1803560895.1642149229

Losada, I. J., Lara, J. L., Guanche, R., & Gonzalez-Ondina, J. M. (2008). Numerical analysis of wave overtopping of rubble mound breakwaters. *Coastal Engineering*, *55*(1), 47–62. https://doi.org/https://doi.org/10.1016/j.coastaleng.2007.06.003

Mansard, E., & Funke, E. (1980). The measurement of incident and reflected spectra using a least squares method. *Coastal Engineering Proceedings*, *1*(17), 8. https://doi.org/10.9753/icce.v17.8

Mata, M. I. (2021). *Numerical estimation of wave loads on crest walls on top of rubble mound breakwaters using openfoam* (Master's thesis). Delft University of Technology. the Netherlands.

Neves, M. G., Didier, E., Brito, M., & Clavero, M. (2021). Numerical and physical modelling of wave overtopping on a smooth impermeable dike with promenade under strong incident waves. *Journal of Marine Science and Engineering*, *9*(8). https://doi.org/10.3390/jmse9080865

Pedersen, J. R., Larsen, B. E., Bredmose, H., & Jasak, H. (2017). A new volume-of-fluid method in openfoam. *MARINE 2017 Computational Methods in Marine Engineering VII*, 266–278.

Peters, D. (2017). *Design of pattern-placed revetmetns* (Doctoral dissertation). https://doi.org/10.4233/uuid:0b67a0dd-a951-46f3-bbaa-86270e546c4e

Pilarczyk, K., & Klein Breteler, M. (1998). Dikes and revetments ; design alternative revetments + gabions. https://www.researchgate.net/publication/294891948_Dikes_and_Revetments_Design_alternative_revetments_gabions

The rock manual: The use of rock in hydraulic engineering. (2007). CIRIA.

Roughness & surface coefficients. (2003). https://www.engineeringtoolbox.com/surface-roughness-ventilation-ducts-d_209.html

Schiereck, G., Verhagen, H., & Hofland, B. (2019). *Introduction to bed, bank and shore protection: Engineering the interface of soil and water* (Second). Delft Academic Press.

Schmitt, P., Windt, J., C. and- Davidson, Ringwood, J., & Whittaker, T. (2020). Beyond vof: Alternative openfoam solvers for numerical wave tanks. *Journal of Ocean Engineering and Marine Energy*, 277–292. https://doi.org/10.1007/s40722-020-00173-9.

Schmitt, P., Windt, C., Davidson, J., & Ringwood, J. V. (2013). The efficient application of an impulse source wavemaker to cfd simulations. *Marine Science and Engineering*. https://doi.org/10.20944/preprints201901.0222.v1

Van Gent, M. R. A. (1995). *Wave interaction with permeable coastal structures* (Doctoral dissertation). Delft University of Technology.

van Gent, M. R. A., Herrera, M. P., Monlines, J., & Jacobsen, N. G. (2017). Rock slopes on top of sand: Modelling of open filters under wave loading. *Coastal Structures and Solutions to Coastal Disasters 2015: Resilient Coastal Communities*. https://doi.org/https://doi.org/10.1061/9780784480304.085

Weller, H., Tabor, G., Jasak, H., & Fureby, C. (1998). A tensorial approach to computational continuum mechanics using object orientated techniques. *Computers in Physics*, *12*, 620–631. https://doi.org/10.1063/1.168744

Windt, C., Davidson, J., Schmitt, P., & Ringwood, J. V. (2017). Assessment of numerical wave makers. *Proceedings of the Twelfth European Wave and Tidal Energy Conference*. https://pureadmin.qub.ac.uk/ws/portalfiles/portal/134527776/WAVHYD_03_707.pdf

Windt, C., Davidson, J., Schmitt, P., & Ringwood, J. V. (2019). On the assessment of numerical wave makers in cfd simulations. *Journal of Marine Science and Engineering*, *7*(2). https://doi.org/10.3390/jmse7020047

Wolsink, G. (1984). *Leidraad cementbetonnen dijkbekleding (inclusief achtergrondrapport)*. Rijkswaterstaat. http://resolver.tudelft.nl/uuid:aa8d1fc1-52d5-435d-9e93-30aa1302bb9f

Yang, X. (2017). Study on slamming pressure calculation formula of plunging breaking wave on sloping sea dike. *International Journal of Naval Architecture and Ocean Engineering*, *9*(4), 439–445. https://doi.org/https://doi.org/10.1016/j.ijnaoe.2016.11.008

Zijlema, M. (2015). *Computational modelling of flow and transport*. Delft University of Technology.

A

OpenFOAM description

The CFD model that is used for this thesis is created in OpenFOAM (Open Field Operation And Manipulation), version foam-extended-3.1. OpenFOAM is an open-source object-oriented C++ class library for continuum-mechanics modelling techniques, including those of incompressible and compressible fluid flow, multiphase flow, and free surface flow, together with various turbulence modelling techniques. Any system of time-dependent partial differential equations including convection, diffusion and source terms can be handled (Weller et al., 1998). The structure of the objects as shown in A.1 represents the hierarchical arrangement in OpenFOAM. To create a model, a case file is needed that contains at least three directories. In the time directory, the initial and boundary conditions are imposed. This directory is called $'0'$. The physical properties of the fluids are quantified in a $constant$ directory even as the subdirectory $polyMesh$ which contains a full description of the case mesh. The last directory is the $system$ directory including three different files. $controlDict$ determines the time-step and write information, in $fvSchemes$ the discretization schemes are selected, and $fvSolution$ where solvers, preconditioners and tolerances are selected at run-time. (Holmes et al., 2012).

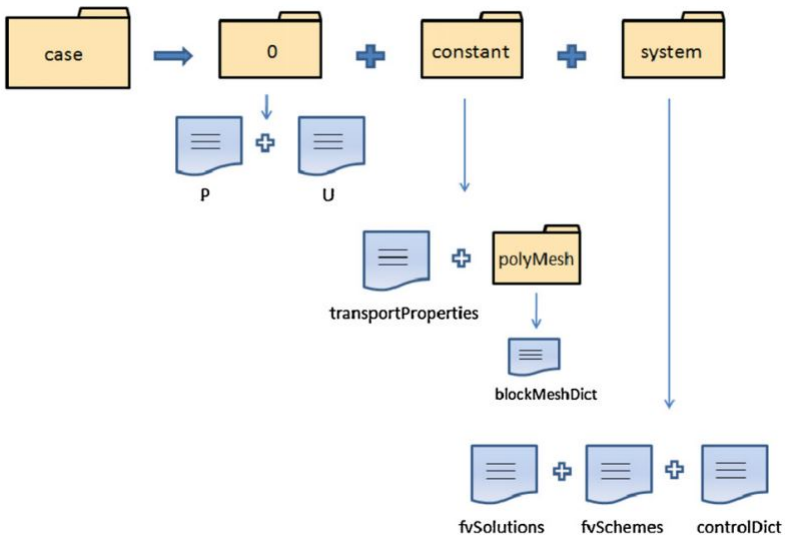

Figure A.1: Basic directory structure OpenFOAM. (Holmes et al., 2012).

In the mathematical framework (2.4.1), the most important equations that are used within the CFD model are discussed. The aim is to derive a numerical solution that is as close as possible to the exact solution. The solution generated by the numerical model is said to be convergent if the numerical solution converges to the exact solution if Δx and $\Delta t \rightarrow 0$ (Zijlema, 2015). To be convergent, a system has to be both consistent and stable. The convergence of a numerical model is dependent on the

numerical scheme that is applied. The numerical schemes could be divided into schemes that use explicit or implicit time integration. Implicit schemes use both the current time step and time step(s) ahead of the current time step. Implicit schemes have no stability requirements. A disadvantage of an implicit scheme is that such models are computationally expensive compared to explicit schemes. Explicit schemes calculated the next time step using previous time steps. A CFD model that uses such a scheme, has to be checked for stability. The OpenFOAM model that is used in this thesis uses an explicit Euler scheme.

B

Numerical wave makers

To analyse wave-structure interaction within a numerical wave flume, generation and absorption of free surface waves within the wave flume are needed. A variety of numerical wave-maker methodologies have been suggested in the literature. For wave generation, five methods are well known: the Relaxation Zone Method (RZM), Static Boundary Method (SBM), Dynamic Boundary Method (DBM), Mass Source Method (MSM) and Impulse Source Method (ISM). For absorption of waves in the numerical wave flume, six different methods are available: RZM, SBM, DBM, Numerical Beach implementations (NB), geometrically sloped beaches and the cell stretching method (Windt et al., 2019). Figure B.1 gives a schematic representation of the different techniques. More details of the wave generation techniques are discussed in this section. For a description of the wave absorption techniques is referred to Windt et al. (2019).

The first method to discuss is the RZM. This method imposes functions for $U(x,t)$ and $\eta(x,t)$ at the boundary of the domain. These solutions are defined as the target solutions, both represented by $\phi_{target}(x,t)$. The relaxation zone is used to blend the target solution $\phi_{target}(x,t)$, with a computed solution, $\phi_{computed}(x,t)$, over the length of the relaxation zone L_R with the following formulas:

$$\phi(\mathbf{x},t) = \chi_R(x)\phi_{\text{computed}}(\mathbf{x},t) + (1-\chi_R(x))\,\phi_{\text{target}}(\mathbf{x},t) \tag{B.1}$$

$$\chi_R(x) = 1 - \frac{\exp\left(\frac{x}{L_R}\right)^{3.5} - 1}{\exp(1) - 1} \quad with \quad x \in [\ 0 \quad L_R\ ] \tag{B.2}$$

In these formulas, χ_R is the weighting function. At the boundary of the domain, this function equals 0 and at the end of the relaxation zone, it has increased to 1. The horizontal coordinate x has a value between 0 and L_R. Relaxation zones are also used to avoid reflection of waves from outlet boundaries and further to avoid waves reflected internally in the computational domain to interfere with the wave maker boundaries (Jacobsen et al., 2012).

The SBM is computationally the most attractive numerical wave-maker methodology. At the boundaries of the domain, $U(x,t)$ and $\eta(x,t)$ are defined. The wave generation and absorption are imposed by these Dirichlet boundary conditions. SBM assumes a uniform velocity profile over the water depth, therefore the method is only applicable in shallow water (Gamaleldin et al., 2020).

The DBM can be seen as the numerical representation of the wave paddle in a physical setup. This method uses a moving wall and dynamic mesh motion. The input could be a time series of the velocity or displacement of the wave maker. When the numerical model has the purpose to mimic a physical test, this method could easily be applied when with the use of the wave paddle data. Similarly, the absorption of the waves can be handled by the movement of the moving wall in the numerical flume.

The MSM wave maker displaces the free surface with a fluid inflow and outflow. A source term $s(x,t)$ is defined coupling the free surface elevation $\eta(x,t)$, wave celerity c, and the surface area of the source $A_s(x,t)$. Since the source term does not alter waves travelling through the source, wave absorption can only be achieved through an additional beach (Windt et al., 2017). The source term is added to the mass equation (2.20) and defined as:

$$s(\mathbf{x},t) = \frac{2c\eta(x,t)}{A_s(x,t)} \tag{B.3}$$

The ISM make use of the same principle as the MSM. A source term is added to the RANS equations. Unlike the MSM, ISM adds the source term to the momentum equation. A disadvantage of this method is the difficulty in calculating the required source function to obtain desired target wave series. Since the free surface is not a variable in the RANS equation, there is no direct expression relating the impulse source function to the resulting generated wave series (Schmitt et al., 2013). Again, wave absorption can only be achieved through an additional beach.

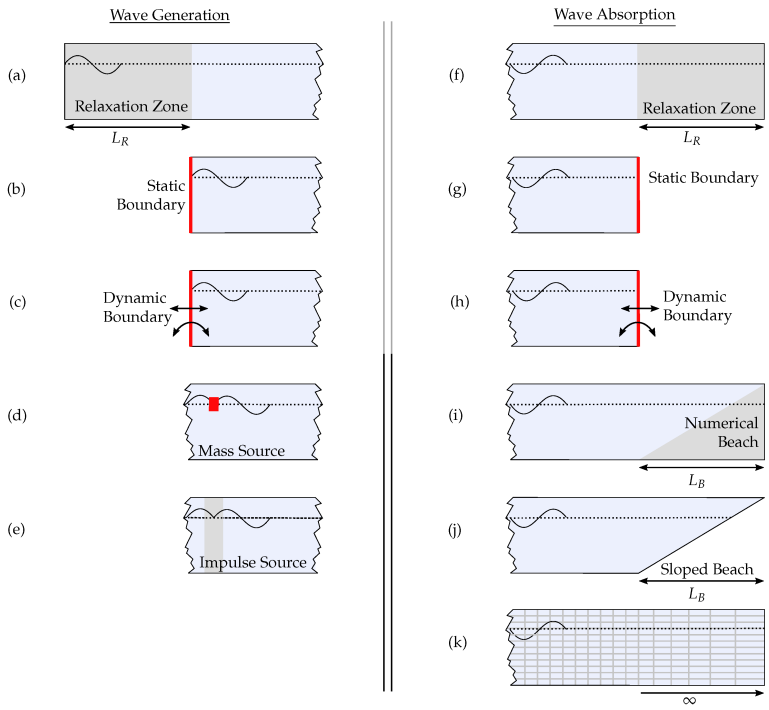

Figure B.1: Generation and absorption techniques.

In this study, the RZM method is employed for wave generation and absorption at the left boundary, which enables both processes to be effectively performed. The relaxation zone method is implemented in the $Waves2Foam$ toolbox and is publicly available. This toolbox is used in Jacobsen et al. (2012), Jensen et al. (2014) and van Gent et al. (2017), among others.

C

Location measuring devices

Number	X-coordinate [m]
1	40.5
2	43.5
3	49.5
4	61.5
5	83.5
6	96.5
7	108.5
8	112.5
9	114.5
10	117.5
11	126.5
12	136.5
13	155.7
14	174.75

Table C.1: Location wave gauges

Number	X [m]	Z [m]	Y [m]
On the top layer			
p1	179.305	0.561	4.203
p2	179.782	0.561	4.334
p3	180.259	0.561	4.466
p4	180.641	0.561	4.571
p5	181.023	0.561	4.676
p6	181.214	0.561	4.729
p7	181.405	0.561	4.781
p8	181.595	0.561	4.834
p9	181.691	0.561	4.860
p10	181.786	0.561	4.886
p11	181.882	0.561	4.913
p12	181.977	0.561	4.939
p13	182.073	0.561	4.965
p14	182.168	0.561	4.992
p15	182.264	0.561	5.018
p16	182.360	0.561	5.045
p17	182.455	0.561	5.071
p18	182.551	0.561	5.097
p19	182.694	0.561	5.137
In the filter layer			
p22	179.821	1.360	4.112
p23	180.409	1.360	4.274
p24	180.997	1.360	4.436
p25	181.273	1.360	4.512
p26	181.551	1.360	4.588
p27	181.828	1.360	4.665
p28	182.104	1.360	4.741
p29	182.242	1.360	4.779
p30	182.381	1.360	4.817
p31	179.519	1.360	4.855
p32	179.588	1.360	4.874

Table C.2: Location pressure transducers

Number	X [m]	Y [m]
On the top layer		
V1	179.305	4.203
V2	179.782	4.334
V3	180.259	4.466
V4	180.641	4.571
V5	181.119	4.706
V6	181.400	4.755
V7	181.500	4.808
V8	181.643	4.847
V9	181.739	4.873
V10	181.834	4.900
V11	181.930	4.926
V12	182.025	4.952
V13	182.121	4.979
V14	182.216	5.005
V15	182.312	5.032
V16	182.408	5.058
V17	182.503	5.084
V18	182.623	5.117
In the filter layer		
V19	179.842	4.118
V20	180.319	4.250
V21	180.701	4.355
V22	181.178	4.486
V23	181.369	4.539
V24	181.600	4.591
V25	181.703	4.631
V26	181.798	4.657
V27	181.894	4.683
V28	181.989	4.710
V29	182.085	4.736
V30	182.180	4.762
V31	182.276	4.789
V32	182.372	4.815
V33	182.467	4.842
V34	182.563	4.868

Table C.3: Location virtual pressure transducers

D

Grain size of continuum top layer (schematization 1)

During this study a $D_{n50} = 0.019m$ is chosen for the top layer, such that the grain size equal the width of the gaps between adjacent blocks. It also would have been possible to relate the width between the gaps to the pore size (instead of to the grain size) of the top layer. In *The Rock Manual* (2007), the relation between the pore and grain size is defined as $z = 0.2D_{15}$. To obtain a pore size equal to the width of the gaps, a (D_{15}) 5 times larger than the width of the gaps had to be chosen. For schematization 1, the applied D_{50} should have been at least 5 times larger than the one applied in the CFD model. In further investigation, a method should be derived to determine values for n and D_{n50} in order to make schematization option 1 applicable for modelling a top layer of a placed block revetment. To illustrate that changing the values for n and D_{n50} leads to better results, an extra simulation is performed:

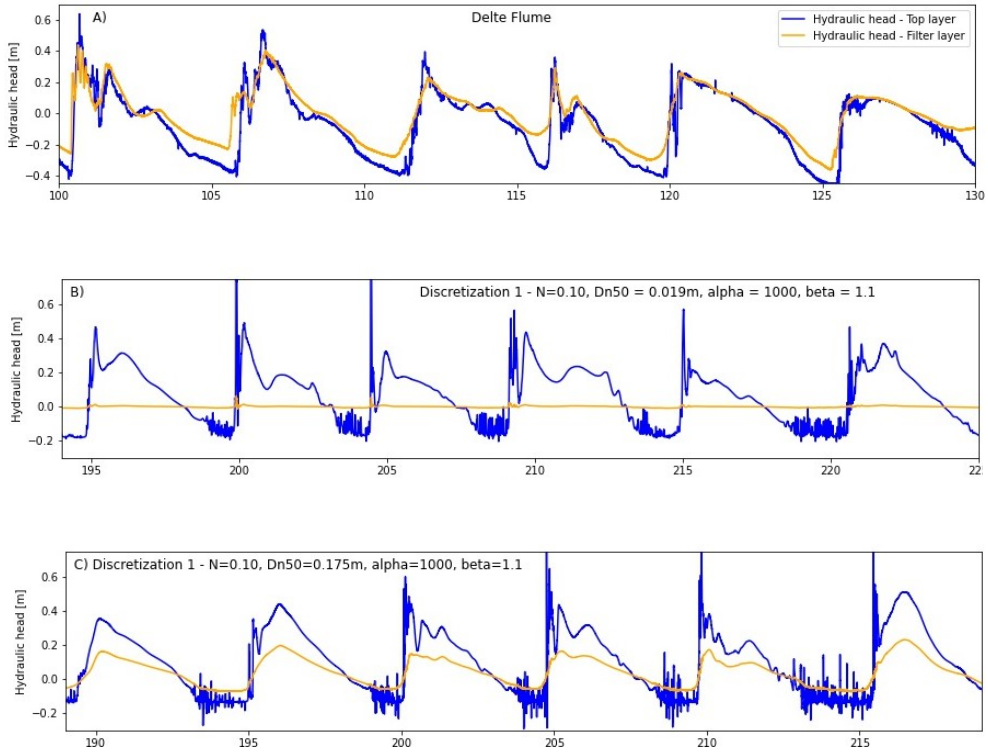

Figure D.1: Time series of the hydraulic head on the top layer (blue graph) and in the filter layer (yellow graph). Figure A shows measurements from the Delta Flume in test 1. Figure B shows the simulated pressures for schematization 1 for the same filter properties as used during this study. Figure C shows the results from a new simulation, in which the D_{n50} is significantly increased to obtain a pressure signal in the filter layer.

Simulation A and B are already shown in Chapter 4. Figure A shows a random time series for hydraulic head on the top layer (blue) and in the filter layer (yellow), obtained from the Delta Flume (test 1). Figure B shows a result from a simulation in which schematization 1 is applied. As concluded in Chapter 4, the resistance through the top layer is too large to model a pressure signal in the filter layer. In figure C a simulation is shown that has not been discussed before in this study. Again, a simulation is performed with schematization method 1, but with a significantly increased grain size ($D_{n50} = D = 0.175m$). An increase in the grain size of the top layer has led to an improvement in the results. This simulation shows that further research into the fictional grain size, in the case of a continuum top layer, is needed to use this schematization method.

E

C-star revetment

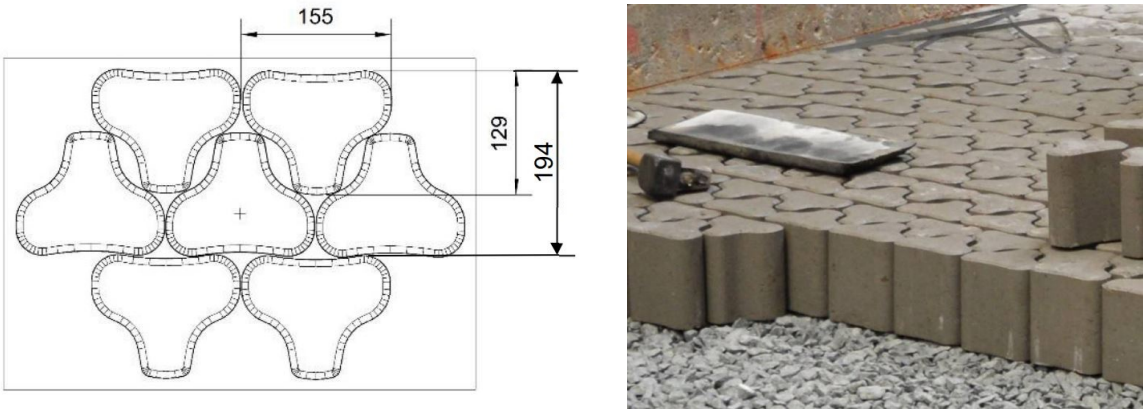

Figure E.1: Geometry of C-star revetment

Figure E.2: C-star revetment

F

Wave propagation

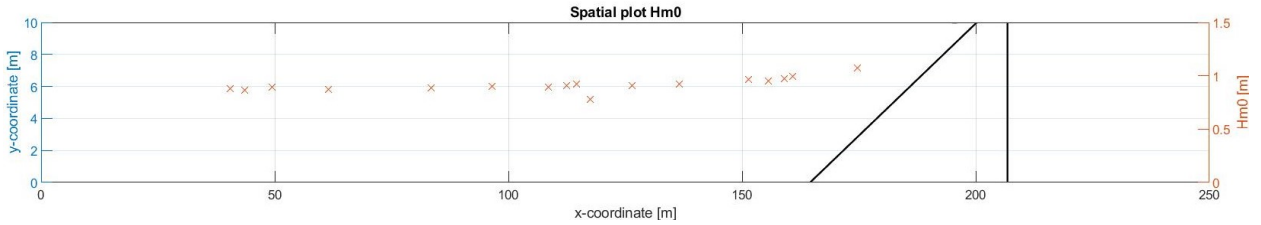

Figure F.1: development of H_{m01} in X - direction for OpenFOAM simulation 1.

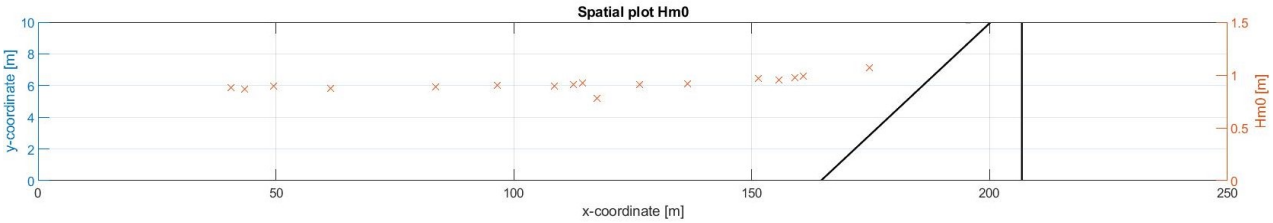

Figure F.2: development of H_{m01} in X - direction for OpenFOAM simulation 2.

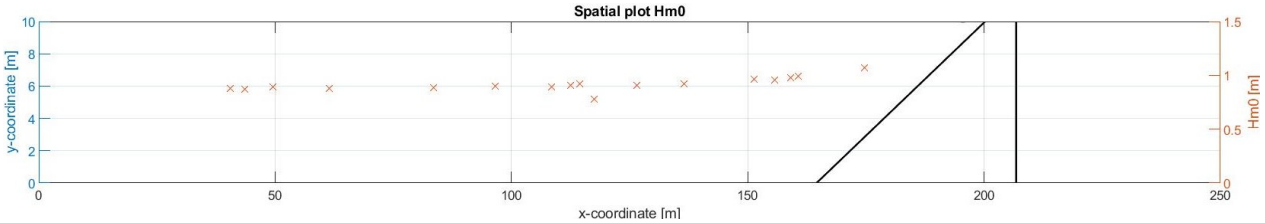

Figure F.3: development of H_{m01} in X - direction for OpenFOAM simulation 3.

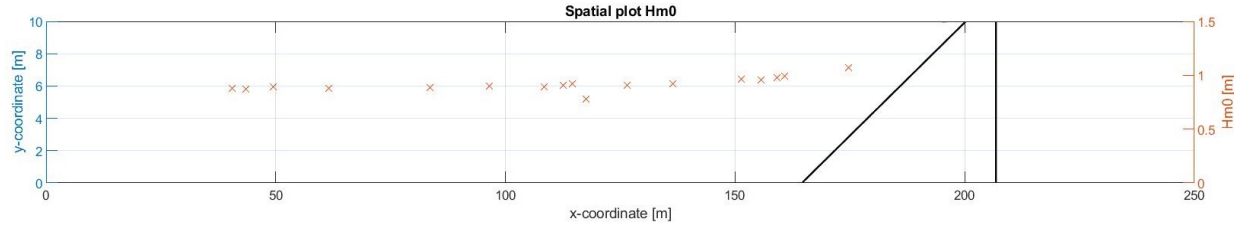

Figure F.4: development of H_{m01} in X - direction for OpenFOAM simulation 4.

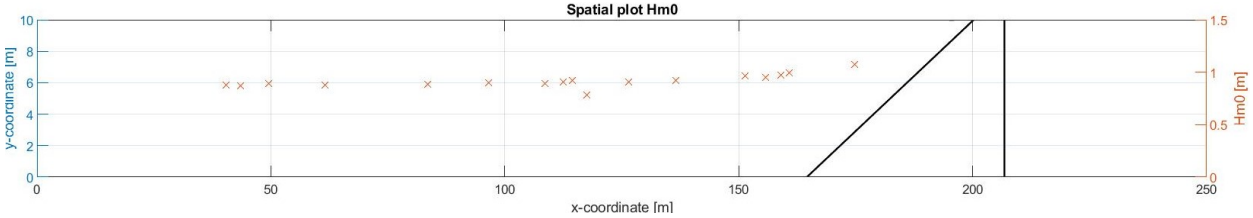

Figure F.5: development of H_{m01} in X - direction for OpenFOAM simulation 5.

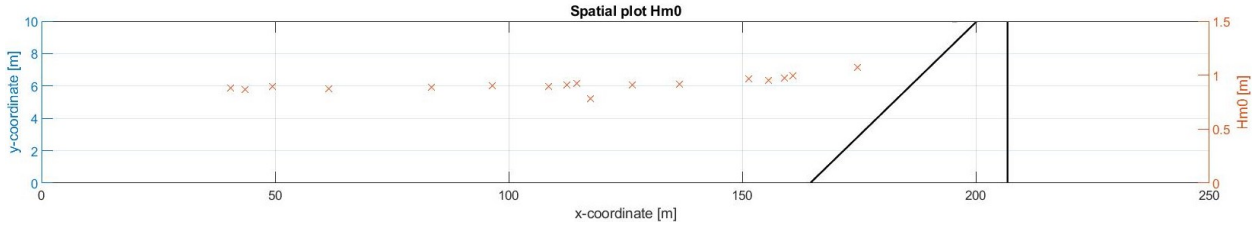

Figure F.6: development of H_{m01} in X - direction for OpenFOAM simulation 6.

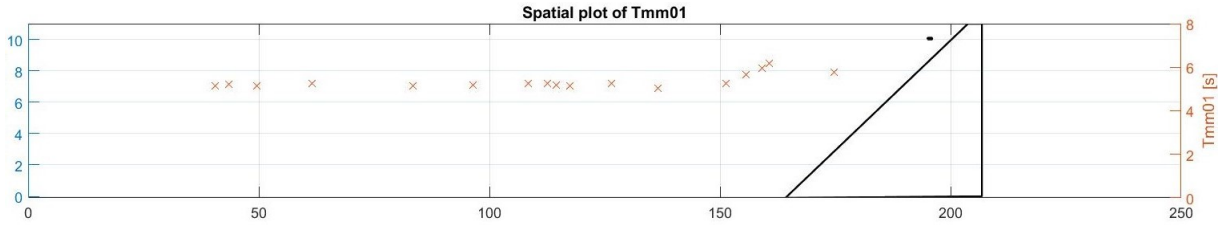

Figure F.7: development of T_{mm01} in X - direction for OpenFOAM simulation 1.

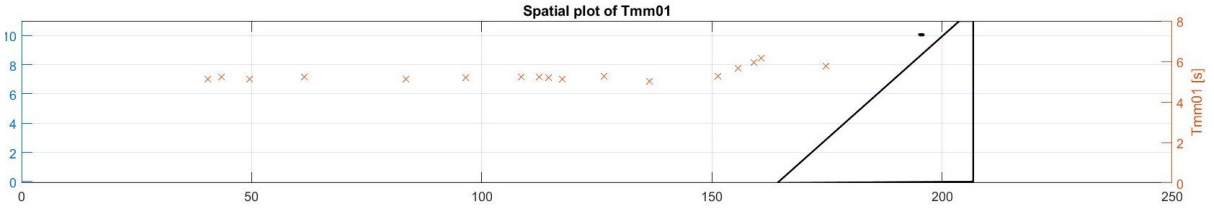

Figure F.8: development of T_{mm01} in X - direction for OpenFOAM simulation 2.

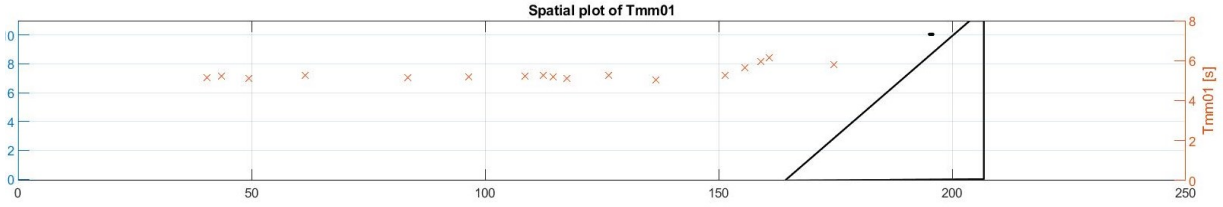

Figure F.9: development of T_{mm01} in X - direction for OpenFOAM simulation 3.

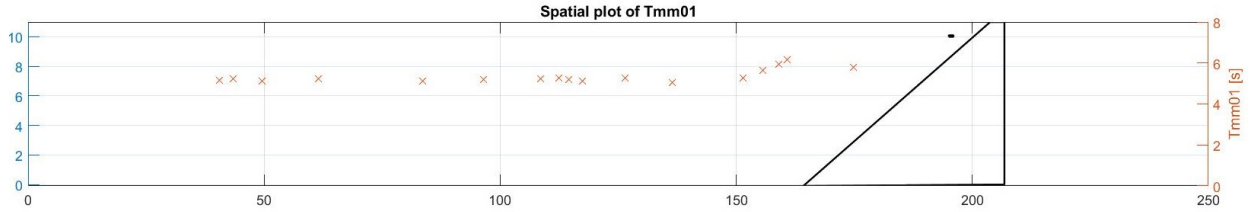

Figure F.10: development of T_{mm01} in X - direction for OpenFOAM simulation 4.

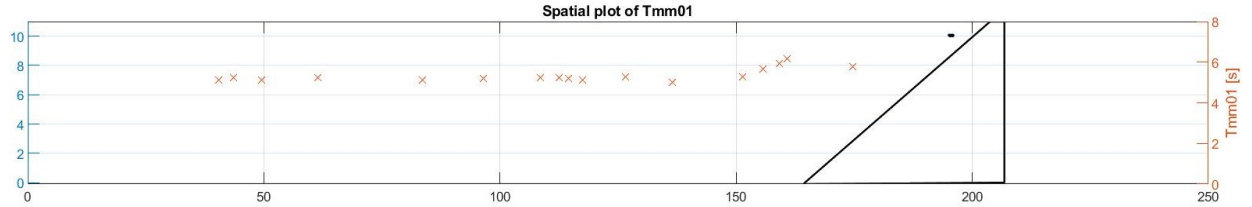

Figure F.11: development of T_{mm01} in X - direction for OpenFOAM simulation 5.

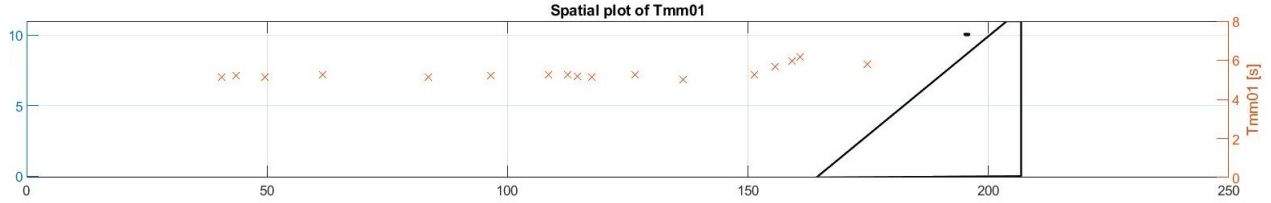

Figure F.12: development of T_{mm01} in X - direction for OpenFOAM simulation 6.

G

Moody diagram

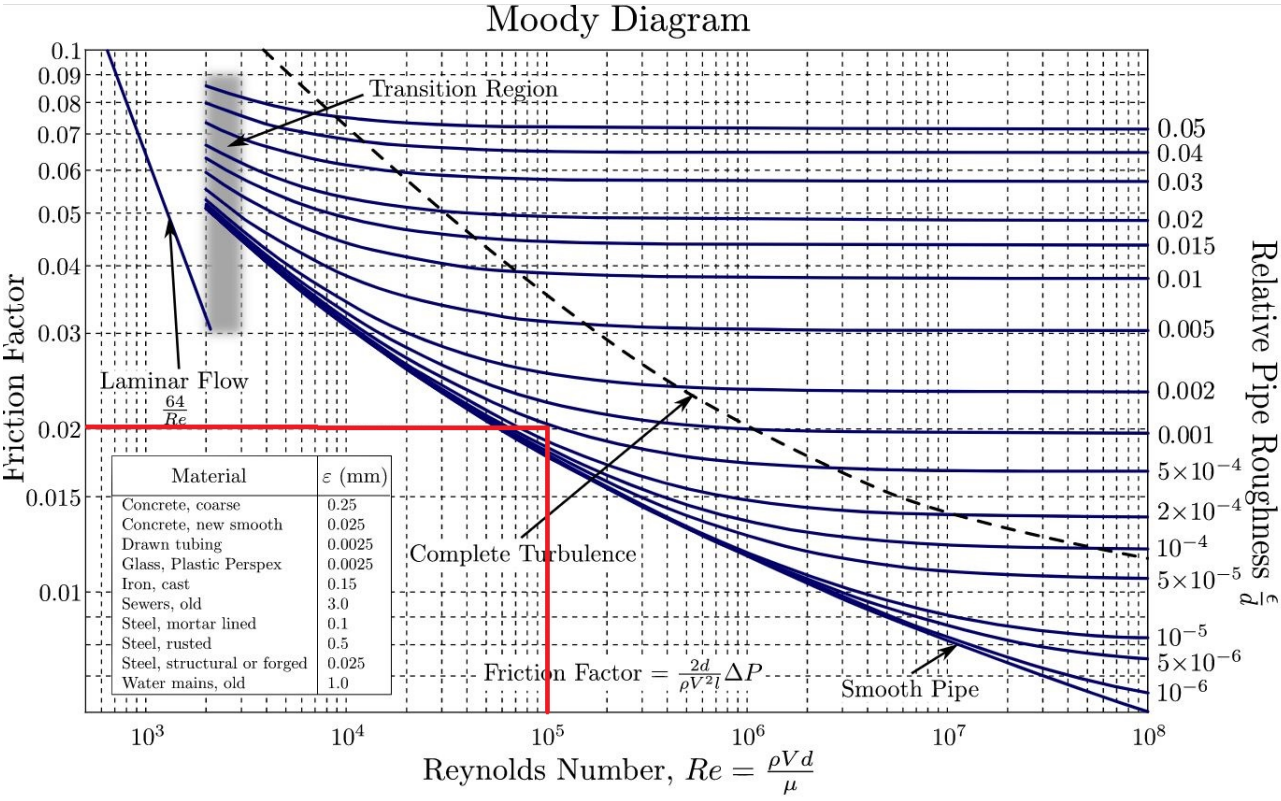

Material	ε (mm)
Concrete, coarse	0.25
Concrete, new smooth	0.025
Drawn tubing	0.0025
Glass, Plastic Perspex	0.0025
Iron, cast	0.15
Sewers, old	3.0
Steel, mortar lined	0.1
Steel, rusted	0.5
Steel, structural or forged	0.025
Water mains, old	1.0